FLORIDA INTERNATIONAL UNIVERSITY

Miami, Florida

$^2H(e,e'p)$ STUDIES OF THE DEUTERON AT HIGH Q^2

A dissertation submitted in partial fulfillment of the

requirements for the degree of

DOCTOR OF PHILOSOPHY

in

PHYSICS

by

Luminita Coman

2007

To: Interim Dean Mark Szuchman
College of Arts and Sciences

This dissertation, written by Luminita Coman, and entitled $^2H(e,e'p)$ Studies of the Deuteron at High Q^2, having been approved in respect to style and intellectual content, is referred to you for judgment.

We have read this dissertation and recommend that it be approved.

John T. Landrum

Misak Sargsian

Jörg Reinhold

Werner U. Boeglin, Major Professor

Date of Defense: July 12, 2007

The dissertation of Luminita Coman is approved.

Interim Dean Mark Szuchman
College of Arts and Sciences

Dean George Walker
University Graduate School

Florida International University, 2007

DEDICATION

To my late mother Aristita.

ACKNOWLEDGMENTS

Throughout the years I was fortunate to have many wonderful teachers and professors that influenced me a great deal. From the many excellent physicists that instructed me while at Bucharest University I would like to specially acknowledge Viorica Florescu, Mariana Vraciu, Constantin Vrejoiu, Ioan Licea and Petrica Cristea. They made a great impresion on me while I was taking their classes and as I look back now, I appreciate them even more at this time. Upon joining the experimental nuclear physics group at Florida International University in 2000 I had the opportunity to be taught by and interact with the members of the group and other faculty, all of them accomplished physicists and benefit from their skills, knowledge and kindness. I would like to thank first my supervisor, Dr. Werner Boeglin, who provided me the opportunity to become his PhD student and for giving me the opportunity to face the challenges of experimental nuclear physics. During the whole period of my work at FIU and at Jefferson Laboratory, he always helped me in my research. I wish to highlight his immense patience, his rich experience, and his readiness to help, anytime I needed him, during my graduate years. He also provided a pleasant working environment and good advice. I consider myself very fortunate to have had him as my advisor. My experimental co-supervisor Dr. Jörg Reinhold deserves my gratitude for his guidance since I first started to work at Jlab in Hall C, and later on in Hall A. I am also indebted to Dr. Misak Sargsian who constantly assisted in making the theoretical physics a familiar ground through his endless series of Special

Nuclear and Particle Physics Seminars (around forty in total). I want to thank all the spokespersons of Experiment E01-020, Werner Boeglin, Mark Jones, Andi Klein, Paul Ulmer, and Eric Voutier for proposing this experiment and making it succesfull. They have invested so much effort with the data analysis after the collection of data was completed. My special thanks to all other members of the E01-020 previous and current analysis team: Hassan Ibrahim, Jeff Lachniet and Rikki Roche' who cooperated with me during the last five years until we obtained the final results. I am very appreciative to Paul Ulmer, Mark Jones and Eric Voutier for all their valuable comments during our Jlab or phone meetings.

The experimental part of my work could not have been started, let alone accomplished, without the help of all members of the E01-020 Hall A Collaboration, too many to be listed here.

In the end, I owe gratitude to my husband, Marius Coman who shared with me his own experience with the experimental nuclear physic data analysis, for his support and understanding. I would like to thank my two children for giving a meaning to my existence, to my sister Veronica for helping me deal with everything and to my friends, Gohar, Carmen, Mihaela and their families who supported me when I went through rough times.

ABSTRACT OF THE DISSERTATION

$^2H(e,e'p)$ STUDIES OF THE DEUTERON

AT HIGH Q^2

by

Luminita Coman

Florida International University, 2007

Miami, Florida

Professor Werner U. Boeglin, Major Professor

A high resolution study of the quasielastic $^2H(e,e'p)n$ reaction was performed in Hall A at the Thomas Jefferson Accelerator Facility in Newport News, Virginia. The measurements were performed at a central momentum transfer of $|q| \sim 2400$ MeV/c, and at a central energy transfer of $\omega \sim 1500$ MeV, a four momentum transfer Q^2 = 3.5 (GeV/c)^2, covering missing momenta from 0 to 0.5 GeV/c. The majority of the measurements were performed at $\Phi = 180^o$ and a small set of measurements were done at $\Phi = 0^o$. The Hall A High Resolution Spectrometers (HRS) were used to detect coincident electrons and protons, respectively. Absolute $^2H(e,e'p)n$ cross sections were obtained as a function of the recoiling neutron scattering angle with respect to $\vec{q}$.

The experimental results were compared to a Plane Wave Impulse Approximation (PWIA) model and to a calculation that includes Final State Interaction (FSI) effects. Experimental ^{2}H$(e,e'p)n$ cross sections were determined with an estimated systematic uncertainty of 7 %. The general features of the measured cross sections

are reproduced by Glauber based calculations that take the motion of the bound nucleons into account (GEA). Final State Interactions (FSI) contributions were found to depend strongly on the angle of the recoiling neutron with respect to the momentum transfer and on the missing momentum. We found a systematic deviation of the theoretical prediction of about 30 %. At small θ_{nq} ($\theta_{nq} < 60^o$) the theory overpredicts the cross section while at large θ_{nq} ($\theta_{nq} > 80^o$) the theory underestimates the cross sections.

We observed an enhancement of the cross section, due to FSI, of about 240 %, as compared to PWIA, for a missing momentum of 0.4 GeV/c at an angle of 75^o. For missing momentum of 0.5 GeV/c the enhancement of the cross section due to the same FSI effects, was about 270 %. This is in agreement with GEA. Standard Glauber calculations predict this large contribution to occur at an angle of 90^o. Our results show that GEA better describes the $^2H(e, e'p)n$ reaction.

TABLE OF CONTENTS

LIST OF TABLES

LIST OF FIGURES

1 Introduction

Understanding nuclear structure and reactions relies on the comprehension of nuclear forces. The understanding of the nuclear force is one of the main objectives of nuclear physics. One cannot hope to understand complex nuclei without first understanding the deuteron, which is the only bound two-nucleon (neutron and proton) system [1]. Nuclear forces are responsible for binding nucleons into atomic nuclei. The short range part of the nuclear force is not well understood. It is agreed that the nuclear force is mediated through meson exchange. However, the progress in understanding the two-nucleon interaction (NN interaction) has been slow. To access the short-distance aspects of the NN interaction, one has to properly select the reaction and the kinematical settings to avoid effects which are not well understood (like three-body interactions) [2]. Theories of nuclear forces and nuclear systems are being developed to allow the connection to the theory of the strong interaction, quantum chromodynamics (QCD) [3]. However, the strong NN interaction inside the nucleus is an interaction between colourless particles at a distance of about 2 fm. It is not understood today how gluon exchange develop into the strong interaction acting at distances of a few fm.

The mean field theory, which describes the nucleus as a system of nucleons moving in a mean field can reproduce many basic features of nuclear structure. However, the repulsive core of nucleon-nucleon (NN) interactions cannot be described by the mean field theory. The simple picture of a particle in a mean field is modified by competing

mechanisms such as meson-exchange currents (MEC), isobaric currents (IC) and final state interactions (FSI). The latter one consists of the interaction of the outgoing nucleon with the residual nucleus (the neutron). For low to intermediate energies, the NN interaction is described by a suitable potential to determine the scattering wave function of the ejected nucleon.

The deuteron, the only two-nucleon bound system, is a widely used system for studying the nuclear force. Since one can calculate the deuteron structure with high accuracy, this system serves as a basis for different models of the nucleon-nucleon force. The electron induced deuteron breakup reaction has been a valuable tool to investigate fundamental problems in nuclear physics such as the ground state and continuum wave function and the structure of the nuclear electromagnetic current operator. In addition, the interaction effects previously mentioned, MEC, IC and FSI can be studied. As a consequence, there is a substantial body of data on this reaction [4, 5, 6, 7, 8].

Quasielasical scattering experiments with electron projectiles yield a description of the relevant physics. They provide essential insight into the microscopic structures in terms of the momentum distribution of the constituent nucleons. The momentum distribution is a powerful quantity for exploring the physics of the nuclei. However, it is not an observable and can only be extracted in the context of a reaction model.

Coincidence $^2H(e,e'p)n$ reactions are well suited for NN interaction studies because, below the pion production threshold (300 MeV), the final state is completely

specified. There exists a substantial body of data on nucleon-nucleon (NN) scattering below the pion-production threshold which is well described by modern potential models for the NN interaction [9]. These models describe differently the short-range structure predicting different high-momentum components of the deuteron wave function. The simplest model of the deuteron electro-disintegration is the Plane Wave Impulse Approximation (PWIA). In this picture, the proton knocked by the virtual photon does not further interact with the unobserved neutron. The lack of re-interaction implies that the momentum of the neutron is the negative of the initial proton momentum. Final state interaction or interaction between the outgoing nucleons after the primary interaction, can significantly change the momentum of the detected nucleon and therefore the inferred initial momentum of the nucleon. Quantitative comparison with the data allows the extraction of the model parameters as well as the quantification of the interaction effects such as FSI, MEC and IC. The present study of the deuteron helps to pin-point these effects so that more quantitative statements about the deuteron wave function can be made. In the present work the investigated reaction is the electro-disintegration of the deuteron at Q^2=3.5 (GeV/c)^2 and recoil momenta (or missing momenta) up to 500 MeV/c. Cross sections of the $^2H(e,e'p)n$ reaction were measured over a range of recoil momenta to test the validity of various relativistic models such as PWIA, standard Glauber Approximation (which neglects the momentum of the recoil neutron) [10, 11] and General Eikonal Approximation (GEA) [12, 13, 14]. The cross section of the reaction is measured for different missing momenta values (200 MeV/c, 400 MeV/c

and 500 MeV/c). The deuteron's short range structure is probed by measurements performed in high missing momenta kinematics. At very large momentum transfers, one hopes to be able to explore the transition from the regime where observables are best described by nucleon degrees of freedom to the regime where the inclusion of quark/gluon degrees of freedom provides a better description of the interaction [15].

1.1 Quasielastic electro-disintegration of the deuteron.

Electron scattering is a useful tool for studying nuclear structure. As the energy transfer increases the wavelength of the virtual poton decreases and the structure of the nucleons themselves can be studied. The interaction in electron scattering is well understood and calculable in Quantum Electrodynamics (QED) [1]. It produces minimal disturbances to the target when compared to other means of investigation such as hadronic probes.

The elementary process of electro-disintegration of the deuteron, within the one-photon exchange approximation (OPEA) is illustrated in Fig. 1 in which an incident electron and a proton exchange a virtual photon. The vector momenta of the incident and scattered electrons define the scattering plane. The struck proton momenta, $\vec{p}_f$, and the momentum transfer 3-vector, $\vec{q}$ define the reaction plane. The angle between these two vectors is denoted by θ_{pq}. The target four momentum in the Lab reference frame is given by $P = (M_d, \mathbf{0})$. The angle between the scattering and the reaction planes (out-of-plane-angle) is denoted by ϕ. The electromagnetic

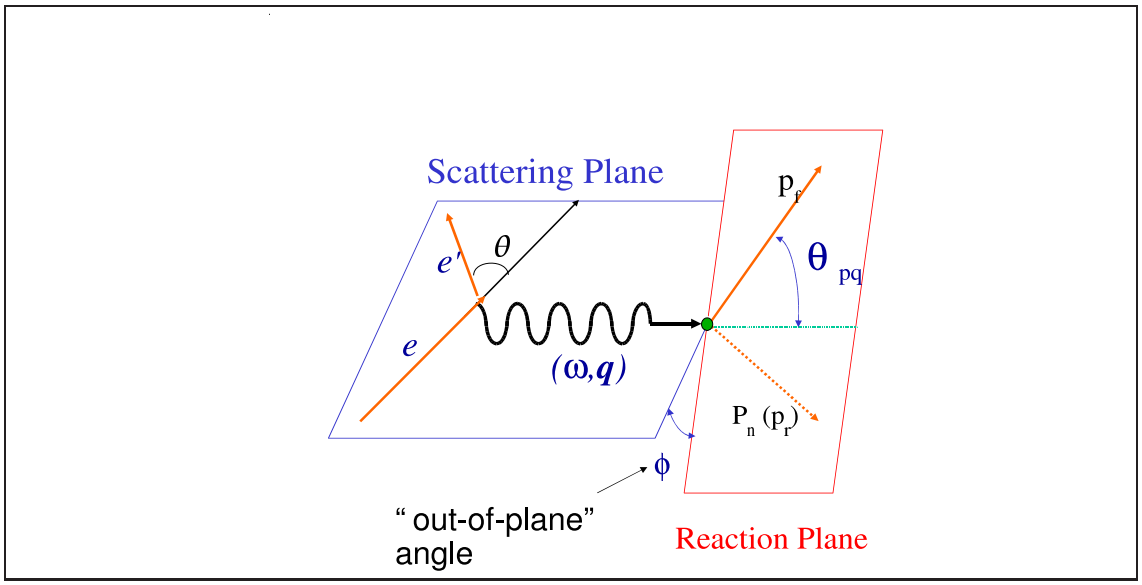

Figure 1: Schematics of the deuteron electro-disintegration reaction.

interaction is mediated by the exchange of a virtual photon, which lies in both planes. The incoming and scattered electrons are treated as plane waves. In the case of PWIA the virtual photon is absorbed by a bound nucleon having a certain initial momentum, $\vec{p}_i$. The struck nucleon leaves the nucleus and is detected having a momentum, $\vec{p}_f$. The residual nucleon has a recoil momentum, $\vec{p}_n$. As the momentum transfer to the target increases, the wavelength of the virtual photon decreases and finer and finer structures of the target can be resolved.

From inclusive $^2H(e,e'p)X$ reactions, in which only the scattered electron is detected, we know that at low-momentum transfer, the elastic peak is the dominant feature of the energy loss spectrum of the scattered electron. When the energy of the virtual photon approaches the value $\frac{Q^2}{2 \cdot M_P}$ (where $Q^2 = |\vec{q}|^2 - \omega^2$ and ω is the energy transferred to the struck nucleon) the electron scatters quasielastically off the proton. As the energy transfer increases the excitation of the nucleon resonances

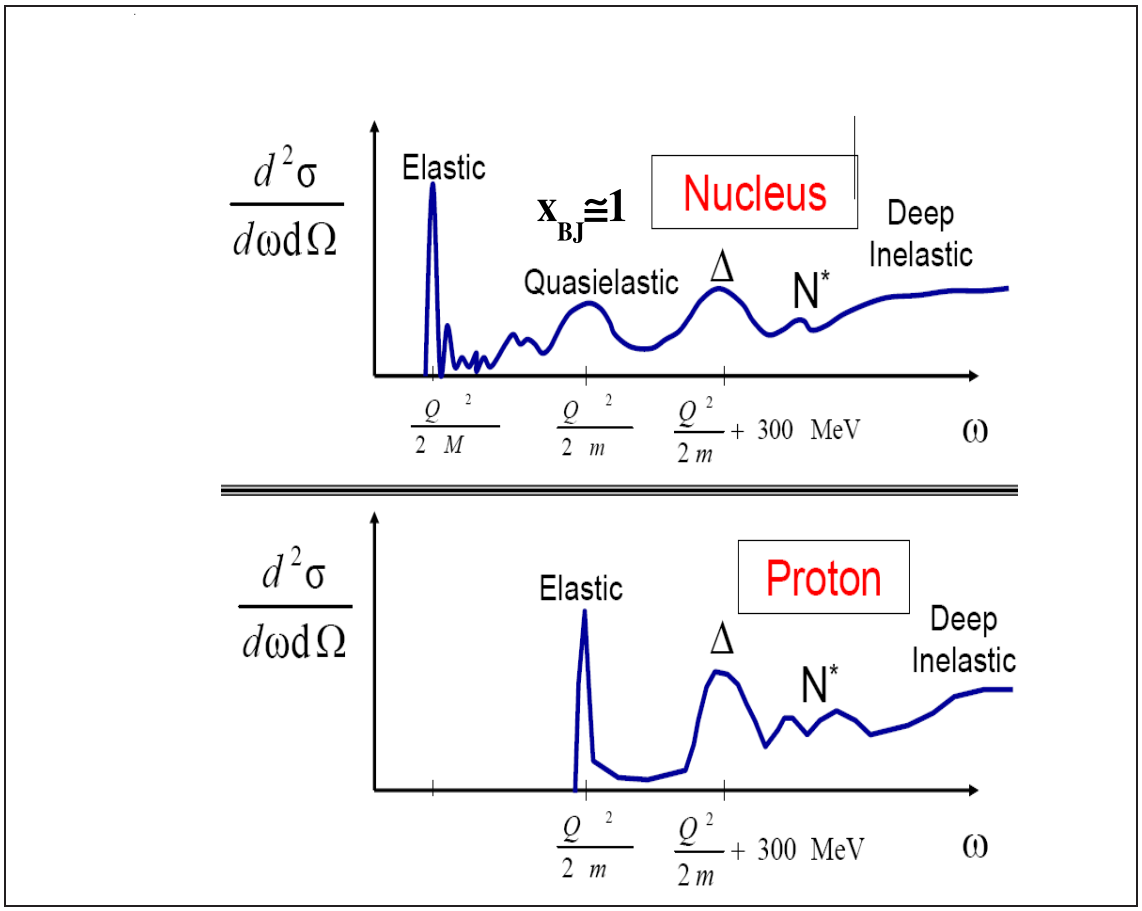

Figure 2: General features of the electron-deuteron scattering cross section as a function of the energy of the virtual photon for a fixed Q^2.

become relatively important. The nucleons become excited to Δ and N* states and the reaction is called *inelastic scattering*. At very high energy and momentum transfers, the wavelength of the virtual photon is so small that the interaction occurs with the individual quarks and the scattering is said to be *deep inelastic* (DIS).

Experiment E01-020 at Thomas Jefferson National Accelerator Facility (Newport News, Virginia) probes the short range properties of the deuteron by investigating the quasielastic ($x_{Bj} \approx 1$ where $x_{Bj} = Q^2/2 \cdot m_P \cdot \omega$) electro-disintegration of the deuteron $^2H(e, e'p)n$ at high missing momenta.

1.2 The motivation for the experiment

The microscopic structure of the nuclei at small distances was practically unexplored before experiment E01-020 [16]. At short distances nucleons in nuclei may be significantly overlapped [14] and high momentum and energy must be transferred to study such configurations of nucleons. This experiment provides a systematic study of the $^2H(e,e'p)n$ reaction down to very short distance scales. It includes kinematics from below to above quasi-free peak (see Fig. 2). To access the shortest time-space distances, experiment E01-020 transferred a high four-momentum to the nucleus and high missing momenta kinematics were selected. There are four main mechanisms competing in the semi-exclusive electro-disintegration reaction, in which the energetic proton is detected in the final state (reaction depicted in Fig. 3):

- Plane wave impulse approximation (PWIA) in which the virtual photon knocks out the bound nucleon which propagates to the final state without further interactions with the residual system.
- Final state interaction (FSI), in which the knockout nucleon re-interacts with the residual system,
- Meson exchange current contributions (MEC) in which the virtual photon, γ^*, interacts with the mesons exchanged between the two nucleon system,
- Isobar current (IC) contributions in which the virtual photon produces Δ-isobar which re-interacts with the residual system.

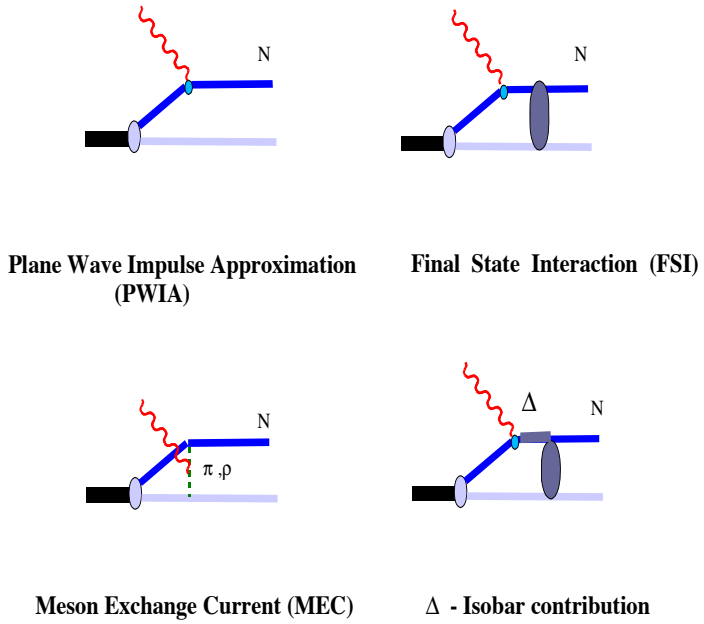

Figure 3: Photon deuteron scattering through different mechanisms: PWIA, FSI, MEC, IC.

Experiment E01-020 studied a large kinematical range to distinguish the role played by these interaction mechanisms. In order to unravel the deuteron short-range structure, one must either select kinematics which minimize FSI, MEC and IC reaction effects or correctly account for such effects. Coincidence measurement allows the initial state of the detected nucleon inside the target nucleus to be inferred, as long as it is assumed that the struck nucleon exits from the system without further interaction. In Fig. 4 the vector momenta involved in the electron induced deuteron break-up reaction is shown: $\vec{p}_f$ is the measured value of the proton momentum, $\vec{q}$ is the measured momentum transfer, and $\vec{p}_R$ is the momentum of the undetected neutron. The easiest way to study the small distance properties of deuteron is the exploration of the PWIA diagram. The difficult part is to disentangle the contributions of the other interactions effects. It can be shown [19] that by providing

a large four-momentum transfer to the nucleus and selecting specific kinematics in which $x_{Bj} \geq 1$ one can considerably suppress MEC and IC effects. One of the main obstructions remains, FSI is practically energy independent at high energies of the outgoing nucleon. FSI can change the cross section at high recoil momenta by an order of magnitude or more. These large effects result from the strength at low initial proton momentum, p_i, appearing at higher inferred p_i due to neutron-proton (np) rescattering in the final state as shown in Fig. 5.

At high energies, when the momentum of the outgoing proton exceeds $\sim 1GeV/c$ the eikonal regime is established. In this case FSI effects depend strongly on the angular kinematics. This requires a careful consideration of angular orientation of the momentum of the rescattering particles.

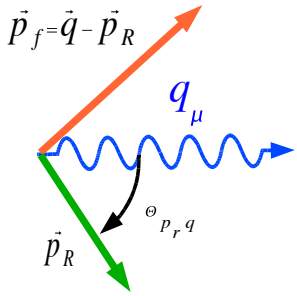

Figure 4: Momentum conservation in the electron-induced deuteron break-up reaction. $\vec{p}_R$ is also referred to as $\vec{p}_s$ when the neutron is a spectator in the reaction (no FSI effects case). $\theta_{p_{rq}}$ is the angle of the outgoing neutron with respect to $\vec{q}$.

When the proton is detected along $\vec{q}$ ($\theta_{nq} = 0^0$) the experimental setting is called "parallel" or "longitudinal" kinematic. We distinguish two cases here:

1. $\vec{q} > \vec{p}_f$ when p_{miss} is parallel to $\vec{q}$ (parallel kinematics).

2. $\vec{q} < \vec{p}_f$ when p_{miss} is parallel to - $\vec{q}$ (anti-parallel kinematics).

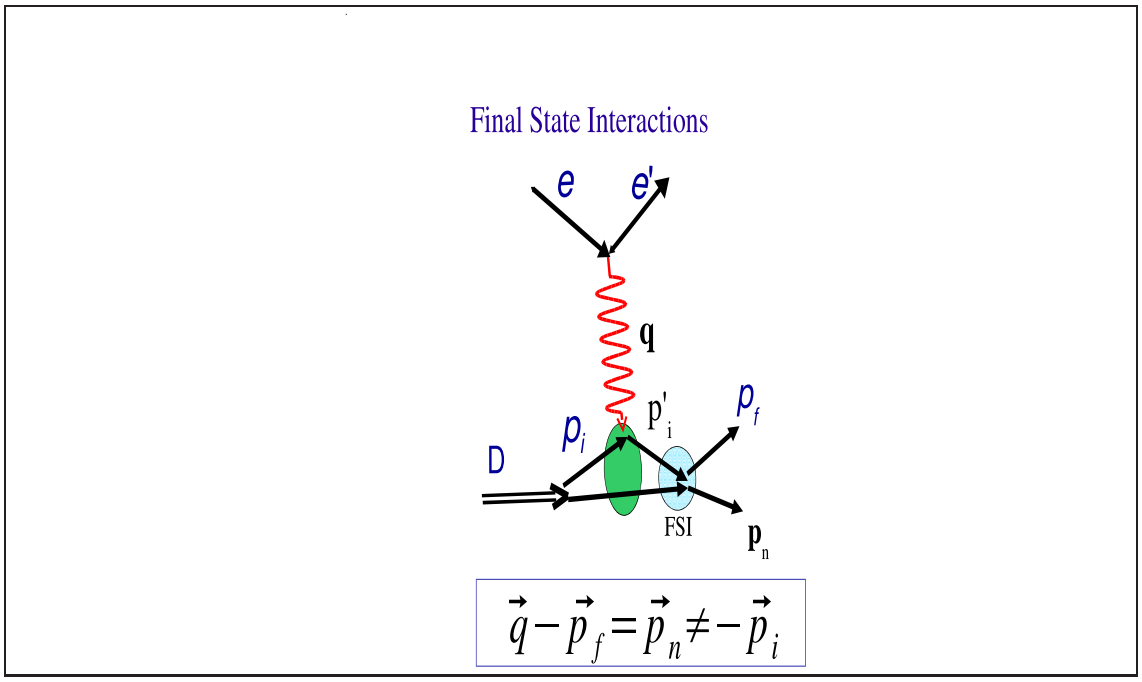

Figure 5: Final State Interaction Mechanism. Here $\vec{p}_n$ is the momentum of the undetected neutron. Due to FSI $\vec{p}_n$ is not equal the neutron momentum before the γ^* p interaction.

When the proton is detected on either side of $\vec{q}$ and $\vec{q} \approx \vec{p}_f$, momentum conservation requires that $\vec{p}_{miss}$ be close to perpendicular to $\vec{q}$ and the kinematic setting is called "perpendicular" or "transverse" kinematics.

Fig. 6 illustrates the transverse and the longitudinal kinematics in PWIA, were $\mathbf{k_f}$ and $\mathbf{k'_f}$ are the vector components of the incoming and scattered electrons. When FSI reaction effects are present low initial proton momentum can be misinterpreted as higher initial proton momentum due to np rescattering in the final state. In the eikonal regime of FSI such effects are likely to be large in perpendicular kinematics, but can be substantially reduced in parallel/anti-parallel kinematics as shown in Fig. 7.

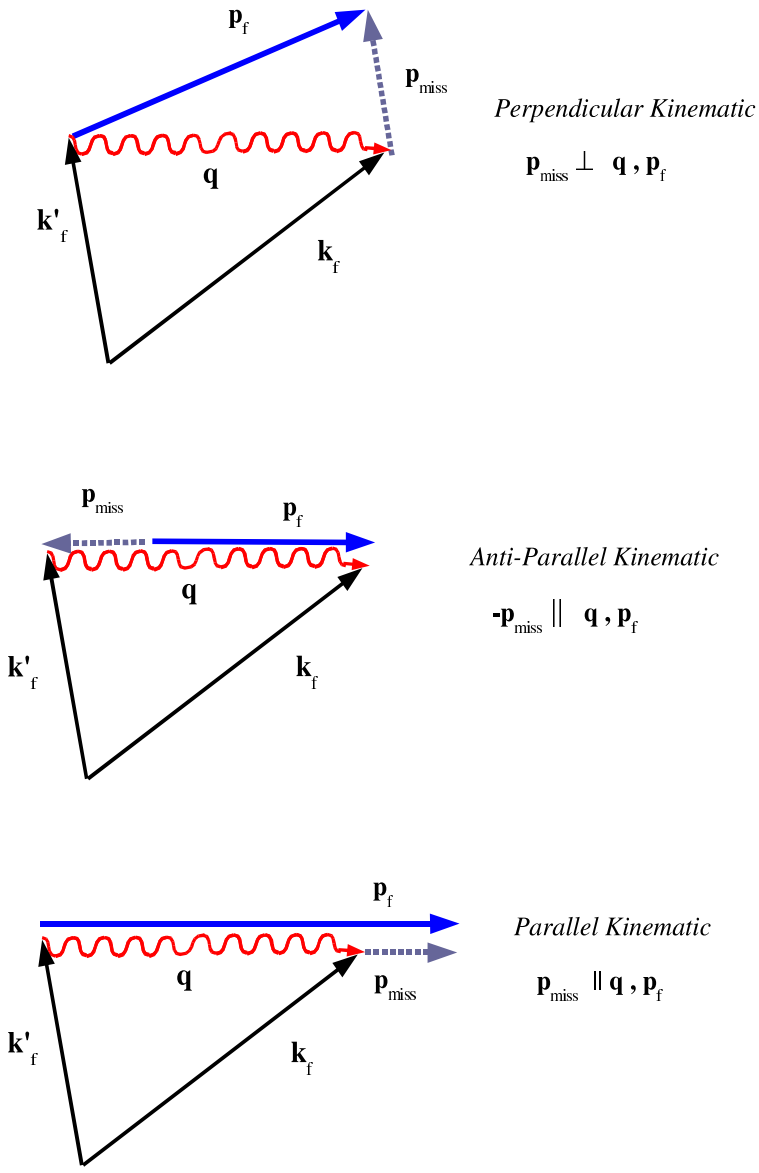

Figure 6: Diagrams of the transverse and longitudinal kinematics in PWIA.

Theoretical studies [20] showed that in transverse kinematics, the PWIA curve is overwhelmed by the FSI effect by orders of magnitude. Therefore, high momentum components cannot be studied in experiments performed in transverse kinematics. In parallel kinematics PWIA and FSI effects are in competition and a quantitative

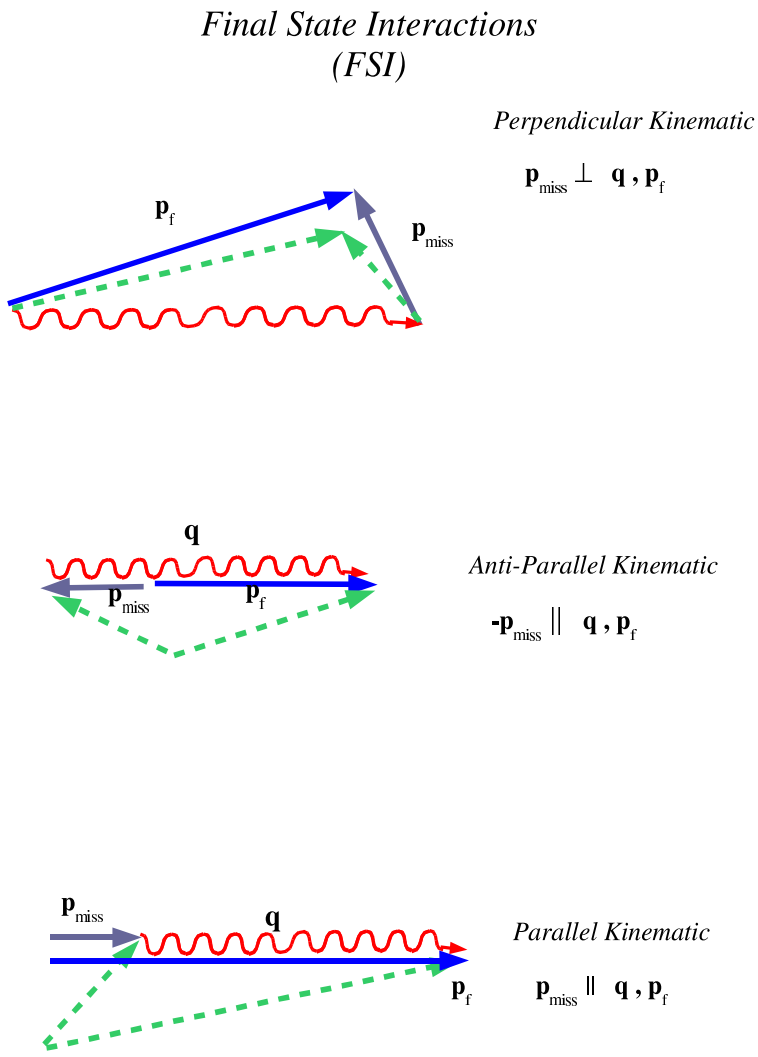

Figure 7: Rescattering diagrams for transverse and longitudinal kinematics. The dashed arrows show the "*true*" values of the proton momenta before *np* rescattering in the final state.

understanding of their interplay is the goal of this experiment. The ratio of the experimental cross section for the deuteron electro-disintegration to the cross section

in the plane wave impulse approximation (PWIA - see Fig. 8) tends to 1 for low missing momenta: $\frac{\sigma^{GEA}}{\sigma^{PWIA}} \approx 1$. This indicates that there are no important FSI effects at these missing momentum values. In this range of nucleon momenta the reaction proceeds mainly through the PWIA mechanism depicted in Fig. 10. FSI effects become important at missing momenta values above 200 MeV/c.

For protons detected along $\vec{q}$ each kinematics emphasizes different aspects of the reaction. At energy transfers above the quasi-free peak ($x_{Bj} > 1$) non-nucleonic effects (MEC and IC) are minimized since the energy transfer is relatively low. The angular distribution of the neutrons in the final hadronic center-of-mass system was studied for a fixed 4-momentum transfer Q^2 and missing momenta, p_{miss}. This allows us a quantitative evaluation of the FSI effects. Such a quantitative study is facilitated via comparison to a generalized eikonal approximation (GEA), expected to be valid at high momentum transfer (which also means high neutron-proton relative momenta in the final state). The conventional Glauber approximation, in which the momentum of the recoil nucleon is neglected in calculation of FSI, predicts a large peak in the angular distribution at angles θ_{nq} around 90^0 about the $\vec{q}$ direction [16]. However, calculations within GEA in which relativistic effects due to finite momentum and excitation energies of recoil nucleons are consistently taken into account [13] predict the peak in the angular distribution at an angle θ_{nq} around 70^0 [14], where θ_{nq} is the angle between the transferred momentum and the direction of the outgoing neutron. Proper treatment of relativity effects is essential at kinematics where the deuteron short-range structure is probed, namely high p_{miss} kinematics. One of the goals of

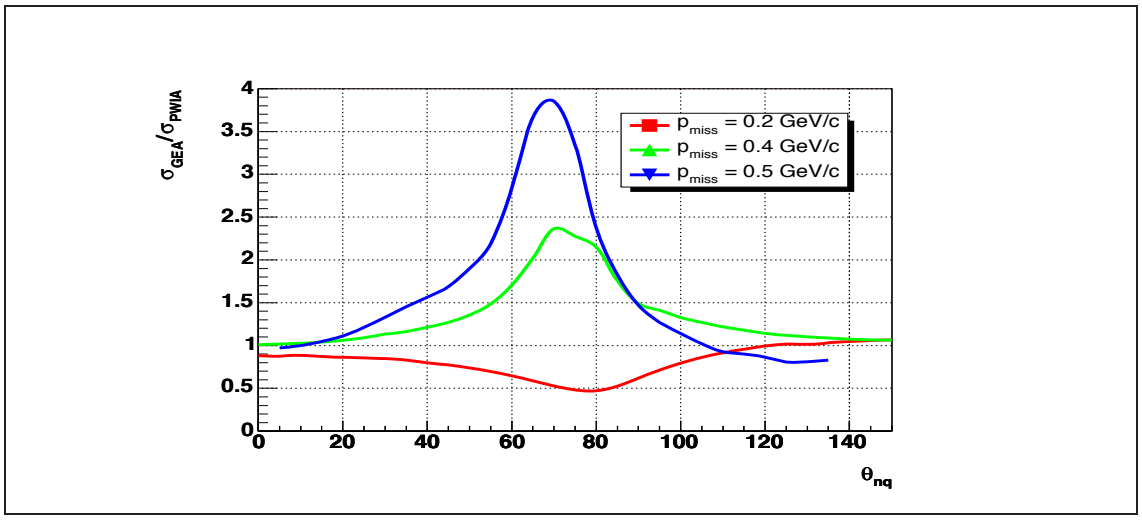

Figure 8: Calculated ratio between σ^{GEA} and σ^{PWIA} at $Q^2 = 4\ (\frac{GeV}{c})^2$.

the present experiment was to check the predictions of GEA. A separation of the interference response function, R_{LT}, was also performed in quasi-elastic kinematics, testing the validity of relativistic models for the $^2H(e,e'p)n$ reaction. This study is not presented here as it was itself the subject of a different Ph.D. Dissertation [21].

1.3 Existing Data

The available body of world data on the $^2H(e,e'p)n$ reaction is large. This proves the importance of this reaction in nuclear physics. Experiments have been carried out at many laboratories such as MAMI (Mainz, Germany), SLAC (Standford, CA, USA), NIKHEF (Amsterdam, The Netherlands), MIT-Bates (Middleton, USA), ALS (Saclay, France) and CEBAF (Newport News, VA, USA). CEBAF and MAMI are able to provide very high-intensity, continuous wave (CW) beams. These have made possible coincidence experiments in kinematical regions which could not be

explored previously. The short-range structure of the deuteron can be revealed by measuring very high recoil momenta in the $^2H(e,e'p)n$ reaction. Prior to the availability of of CW, the cross sections could be measured for large missing momenta ($p_{miss} \sim 0.5 GeV/c$) only at relatively small momentum transfers ($Q^2 \sim 0.1 (GeV/c)^2$) or for large Q^2 only at relatively small missing momenta($p_{miss} \leq 0.5 GeV/c$). Experiments carried out in the last decade at CEBAF, MAMI, NIKEF and MIT-Bates benefited from the availability of high-duty cycle beams. These experiments explored the $^2H(e,e'p)n$ reaction by measuring either the cross section over a large missing momenta range or by extracting various response functions.

Several experiments measured cross sections of $^2H(e,e'p)n$ at low Q^2 for a wide range of missing momenta [5, 6, 9, 22]. It has been found that with increasing recoil momentum FSI, MEC and IC increase dramatically and PWIA model becomes invalid. Fig. 9 shows the $^2H(e,e'p)n$ cross section measured at MAMI [6] and Arenhovel's calculations that includes FSI, MEC and IC contributions [23].

The cross section is well reproduced by theory up to $\sim$ 350 MeV/c, while for higher p_{miss} there are discrepancies between theory and experiment.

Experiments intended to extract various response functions have been carried out at various electron accelerators [7, 8, 17, 25, 18, 24, 26, 27, 28]. In general, the response functions were extracted for low missing momenta ($p_{miss} < 200 MeV/c$). Longitudinal and transverse response functions (R_L and R_T) have been measured at NIKEFF [7, 8], MIT-Bates [26] and Saclay [25].

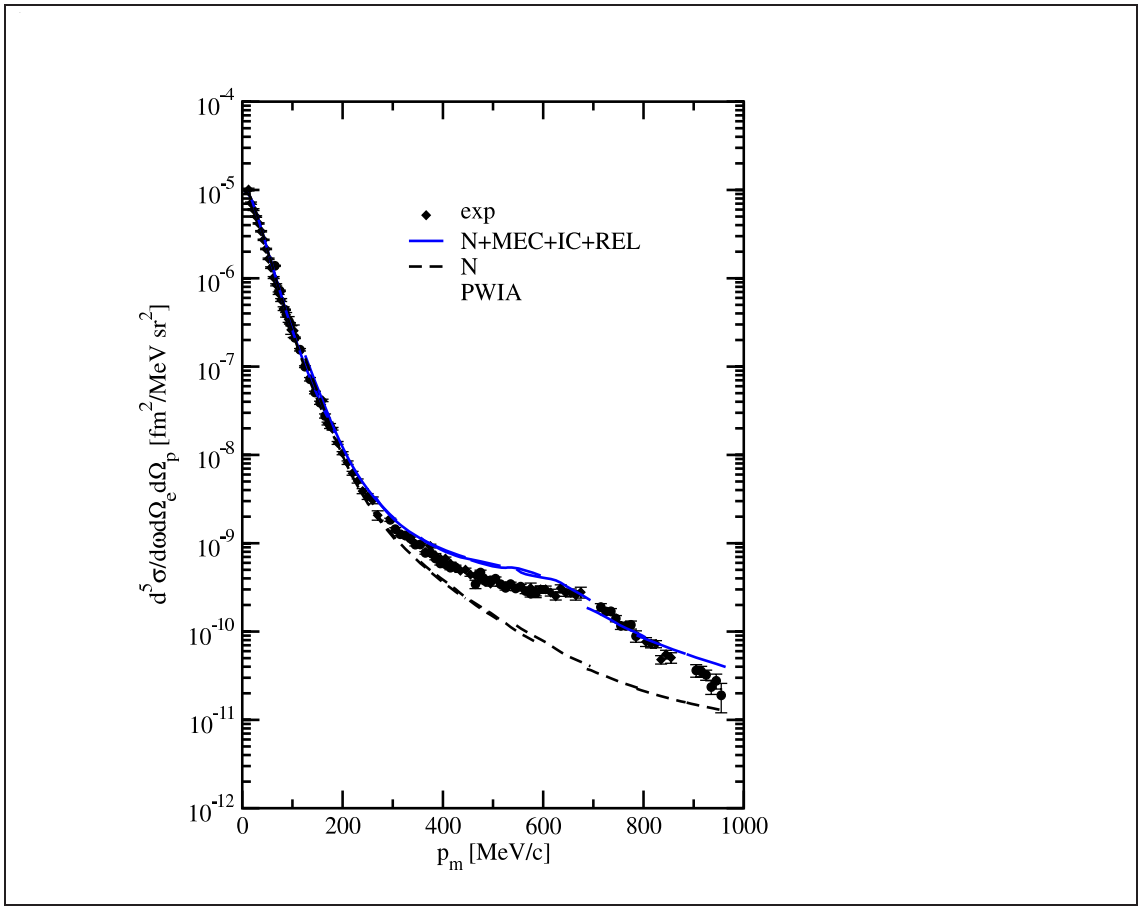

Figure 9: $^2H(e,e'p)n$ cross section measured at MAMI (varying Q^2) [6].

Several experiments involving measurement of the ejected proton polarization have been carried out at MIT-Bates [29, 30, 31]. Due to limitations in the energy, several attempts failed to access the short distance structure of the deuteron [5, 22]. For the Turck-Chieze and high recoil Blomqvist data, the kinematics were in the delta-region. In this region the lack of a knowledge of the reaction mechanism makes it difficult to deduce aspects of the deuteron structure. Cross section measurements at high Q^2 were done at SLAC for low recoil momenta [18].

The Mainz measurement [6] sampled recoils momenta up to 928 MeV/c. It was found out that the main part of the cross section arises from the interaction with

the neutron, while the detected proton is a spectator. Within this proton spectator picture, the actual internal momentum probed in this process is the momentum of the detected proton (not the momentum of the neutron). Furthermore, the kinematics were in the delta-region of the inclusive (e,e') spectrum which imposed the inclusion of virtual nucleon excitations in order to obtain agreement with the data

In contrast, the experiment E01-020 at JLAB could examine large recoil momenta at or even below quasi-free kinematics. In this kinematical range the extraction of the deuteron structure is less model-dependent. It is stressed that JLAB is the only facility in the world where such a study could be undertaken.

1.4 The ^{2}H(e,e'p) reaction

The momenta of the two nucleons in the deuteron nucleus (at rest) are equal in magnitude and opposite in direction. When we strike one nucleon with initial momentum, $\vec{p}_m$, in the pair, the other nucleon will have a momentum, - $\vec{p}_m$. The missing momentum, $\vec{p}_{miss}$, is the momentum of the undetected nucleon, $\vec{p}_{miss} = -\vec{p}_m$ and $\vec{p}_{miss} = \vec{q} - \vec{p}_f$. A short overview of the PWIA mechanism and the Final State Interaction mechanism depicted in Fig. 10 and Fig. 11 is given here. In PWIA, the residual system, the neutron is a spectator and the momentum of the neutron is refered to as $\vec{p}_s$ (the s indices stands for spectator) or $\vec{p}_R$ (with the indices R coming from the word residual).

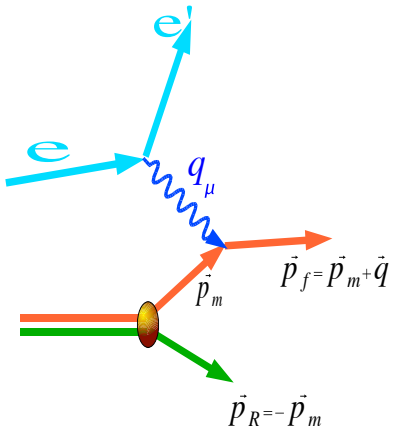

Figure 10: Feynman diagram of the deuteron electro-disintegration in the Plane Wave Impulse Approximation.

The initial momentum in PWIA can be related to $\vec{p}_f$ and $\vec{q}$ as follows:

$$\vec{p}_m = \vec{p}_f - \vec{q}. \tag{1}$$

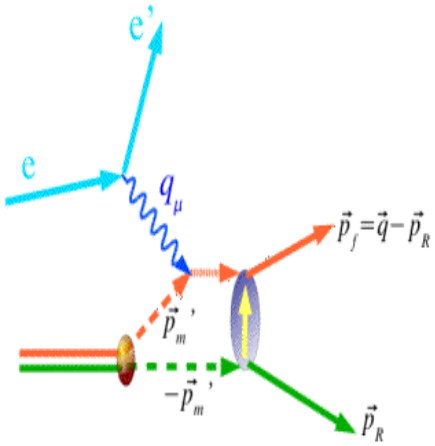

Figure 11: Feynman diagram of the deuteron electro-disintegration. Final State Interaction mechanism.

The larger the initial momentum, $\vec{p}_m$, the closer are the two nucleons in the deuteron nucleus. Thus increasing the relative momentum of n and p allows us to probe two nucleons at short separations.

The relative motion of the two nucleons is completely described by the wave function in the momentum space $\Phi(p)$ and the relative momentum can be written:

$$\vec{p}_{rel} = \frac{\vec{p}_p - \vec{p}_n}{2}, \text{which becomes in the Lab frame } \vec{p}_{rel} = \frac{\vec{p}_m - (-\vec{p}_m)}{2} = \vec{p}_m. \quad (2)$$

In PWIA, by substracting the transfered momentum, $\vec{q}$, from the measured final momenta of the emerging proton, $\vec{p}_f$, we obtain the missing momentum $\vec{p}_f - \vec{q} = \vec{p}_m$. In the FSI process - see Fig. 11, this relation does not hold true because of the rescattering of the two nucleons. So $\vec{p}_n = -\vec{p}_m$ is not the initial momentum of the nucleon inside the deuteron nucleus. When studying high missing momenta configurations, one has to correctly acount for FSI effects and/or select kinematics where this effects are minimized.

2 Kinematics

We consider kinematics in which the deuteron breaks up into a proton and a neutron, with no other particles, such as pions, in the final state. Within the convention that the first component of a four-vector represents the total energy (rest energy plus kinetic energy) and the other three components represent the vector momenta involved, we define the four momentum vectors of the incoming and scattered electrons, e and e' and the four-momentum transfer q:

$$e = (E_e, \vec{p}_e) \quad \text{and} \quad e' = (E_{e'}, \vec{p_e'})$$

$$q = e - e' = (\omega, \vec{q}) = ((E_e - E'_e), (\vec{p}_e - \vec{p_e'})). \quad (3)$$

The four vector q determines the energy and momentum transferred to the nuclear target. Its components are the electron energy loss, ω, in the laboratory system and the momentum transfer, $\vec{q}$.

The square of the four momentum transfer, q^2, is the mass of the virtual photon.

$$q^2 = (e - e')^2 = ((E - E'), \vec{q})^2 \tag{4}$$

When neglecting the mass of the electron, one can write q^2 as:

$$q^2 = -4 \cdot E \cdot E' \cdot \sin^2 \frac{\theta_e}{2} \tag{5}$$

where θ_e is the electron scattering angle in the laboratory. Since q^2 is negative for virtual photons, the convention $Q^2 = -q^2$ is used.

As mentioned previously, rescattering describes the process of a proton-neutron scattering after the primary *(e,e'N)* reaction. This leads to a change of the energy and momentum of the outgoing proton. In the PWIA case one assumes that the entire momentum, q, is transferred to a single nucleon. If this nucleon is detected with a final momentum, p_f, its original momentum can be inferred to be:

$$p_i = p_f - q = -p_{miss} \quad \text{with} \quad |p_{miss}| = |p_i| \tag{6}$$

The missing momentum is the initial momentum of the spectator neutron when the interaction between the virtual photon and proton takes place. We do not explicitly measure it, we calculate it using four-momentum conservation. When FSI are

present, a misleading E_{miss}, p_{miss} are reconstructed. The np interaction after the primary *(e,e'p)* reaction leads to changes in the momentum and energy of the detected proton. Energy and momentum are transferred to the deuteron target, at rest in the Lab frame ($P_D = (m_D, 0)$), through the virtual photon. As a result of this transfer, the deuteron breaks up into its component nucleons - the proton and the neutron, each with the corresponding four momenta, p_p (or p_f) and p_n (or p_R), respectively. From the four momentum conservation it follows:

$$P_\mu^D + q_\mu = p_p + p_n \tag{7}$$

where $p_p = (E_p, p_p)$ and $p_n = (E_n, p_n)$, with the energies of the nucleons being the sum of the rest energy and the kinetic energy : $E_p = m_p + T_p$, and $E_n = m_n + T_n$.

By measuring the momenta and angles of the scattered electron and the knockout proton the missing momentum, $\vec{p}_{miss}$, and the missing energy, E_{miss}, are reconstructed:

$$\vec{p}_{miss} = \vec{q} - \vec{p}_p \qquad\qquad E_{miss} = \omega - T_p - T_n \tag{8}$$

E_{miss} is equal to the deuteron binding energy 2.225 MeV (the energy needed to remove the nucleon from a particular state within the nucleus). Here T_p and T_n are the kinetic energies of the knockout proton and neutron. When assuming that the virtual photon interacts with the proton, the mass squared of the system recoiling against the electron (i.e the photon-proton system) is given by an invariant quantity:

$$W^2 = -Q^2 + 2\omega(M_D - E_n) + 2\vec{q}\cdot\vec{p}_n + {M_D}^2 - 2E_n M_D + {m_n}^2, \tag{9}$$

where M_D is the deuteron mass and E_n is the neutron total energy. Another useful invariant quantity is the Bjorken scaling variable, x_B:

$$x_B = \frac{Q^2}{2 \cdot p \cdot q} = \frac{Q^2}{2 \cdot m_p \cdot \omega}. \tag{10}$$

where $Q^2 = \vec{q}^2 - \omega^2$ with $\vec{q}$ the momentum and energy of the virtual photon and m_p is the proton's mass. x_B is interpreted in the quark-parton model as the fraction of the target nucleon's momentum carried by the struck quark. The condition where x_B is approximately 1 is called quasielastic scattering. The Bjorken x depends entirely on the electron kinematics. In the E01-020 experiment data were taken at kinematics below and above the quasielastic peak (see Appendix A) meaning:

$$0.83 \leq x_{Bj} \leq 1.52 \tag{11}$$

During E01-020 we have focused on measuring the angular distribution of the cross section for the $(e, e'p)$ reaction and the corresponding cross section $\sigma(\theta_{nq})$ or $\sigma(x_{Bj})$. The variables θ_{nq} and x_{Bj} are related through 4 momentum conservation (eq. 7). Using Eq. 5 and Eq. 10 and neglecting the mass of the electron one arrives at the following expression for the x_{Bj} variable:

$$x_{Bj} = 1 - \frac{T_n}{m_n} - \frac{2T_n}{\omega} + \frac{\vec{q} \cdot \vec{p}_n}{m_n \omega} \tag{12}$$

where T_n is the kinetic energy of the outgoing neutron, m_n, is the mass of the neutron, ω is the energy transfer, $\vec{q}$ and $\vec{p}_n$ are the vector momentum of the virtual photon and of the neutron, respectively. Eq. 12 relates x_{Bj} to the angle θ_{nq} between $\vec{p}_n$ and

$\vec{q}$ which appear in the $\vec{q} \cdot \vec{p}_n$ scalar product. Fig. 12 shows the relation between θ_{nq} and x_{Bj}.

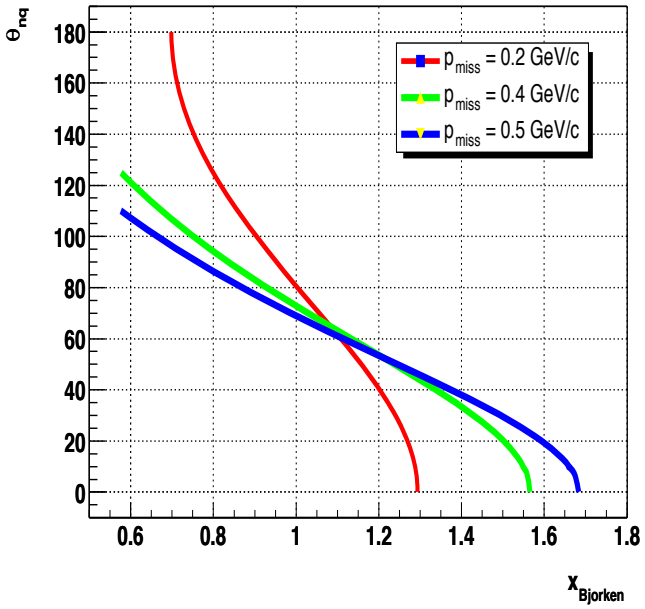

Figure 12: θ_{nq} vs. x_{Bj} for Q^2=3.5 (MeV/c)^2.

In order to vary the angle θ_{nq} we changed the energy transfer $\omega = E - E'$, the electron scattering angle and adjusted the proton setector. During the experiment Q^2 was kept constant.

3 Generalized Eikonal Approximation

The semi-exclusive process $e + d \rightarrow e + n + p$ in which the scattered electron and the scattered proton are detected can proceed via competing reaction mechanisms. The frameworks used to treat the FSI effects in modeling A(e,e'p) reactions can roughly be divided in two major classes. In the "low energy" regime ($p_p < 1$ GeV/c) most models use a potential to determine the scattering wave function for the ejected proton. At higher energies ($p_p > 1$ GeV/c) a Glauber model is used. The theoretical framework for the calculation of high energy semi-exclusive nucleon knockout from nuclear targets at large $\vec{p}_{miss}$ or recoil momenta of residual nucleons is based on effective Feynman diagram rules and is described in detail in [14]. The result of this approach is the Generalized Eikonal Approximation (GEA), which is reduced to a Glauber approximation when the nucleon recoil is neglected.

3.1 Plane Wave Impulse Approximation

In the general type of the reaction schematically shown in Figure 1, a large momentum $q \equiv (\omega, q)$ is transferred to the nucleus ($\vec{q} > 1$ GeV/c). The final state in the reaction consists of the fast proton that carries almost the entire momentum of the virtual photon ($\mathbf{p_f} \approx \mathbf{q}$), with $|\mathbf{q}| \sim$ 2-3 GeV/c. The other nucleon in the final state (the undetected neutron) has a relatively low momentum in the final state (p_s, $p_m \sim$ 500 MeV/c). The energy of the residual system is much lower than the energy of the knockout proton: $E_n = E_f - \omega \ll E_f$. $\mathbf{p_m} = \mathbf{p_f} - \mathbf{q}$ is the missing momentum of

the reaction, $E_f = \sqrt{m^2 + p_f^2}$, E_n is the energy of the residual nuclear system (the neutron) and m is the mass of the nucleon.

The electron part of the reaction is calculated from quantum electrodynamics (QED). Therefore, when considering electron scattering from nucleons and nuclei, the leptonic part of the process can be assumed to be well under control. The uncertainties in the model of the reaction come from the electron-nucleon (e-N) vertex and from the dynamics of the nucleons. The scattering process of an electron off a free (or on-shell) nucleon can be computed in a model-independent fashion. The electromagnetic coupling for a bound (or off-shell) nucleon has a more complicated structure than for free nucleons. The electromagnetic coupling, characterized by the fine structure constant $\alpha = e^2/\bar{h} \cdot c \approx 1/137$, is relativelly small and one only needs to consider the lowest order electromagnetic process involved. This lowest order one-photon exchange approximation is generally accepted to be sufficiently accurate.

The probability that the photon knocks out the proton from the deuteron nucleus is given by the product of a probability amplitude to find a proton with momentum p in the deuteron and the probability amplitude that the virtual γ photon scatters from the proton. The amplitude, A_0, which describes the knockout process for an exclusive scattering in the framework of PWIA can be presented as follows.

$$A_0 = \phi_D(p_i) \cdot A_{eN}(p_m) \tag{13}$$

where: $\phi_D(p_i)$ is the wave function of the deuteron, and $A_{eN}(p_m)$ is the amplitude of the $e-N$ scattering for a nucleon, N, with momentum, p_m. The $e-N$ cross section,

σ_{eN}, is proportional to the square of the scattering amplitude: $\sigma_{eN} \sim {A_{eN}}^2$. In [14] it is shown that the covariant Feynman amplitude corresponding to the impulse approximation diagram of Figure 10 can be written:

$$A_0^\mu = \sqrt{(2\pi)^3 2E_s}\psi_D(p_s)j^\mu(p_s, q), \tag{14}$$

where $\psi_D(p_s)$ is the non-relativistic deuteron wave function, and $j^\mu(p_s, q)$ is the electromagnetic current for a bound nucleon.

3.2 FSI - Single Rescattering Amplitude

The experiment was designed to study the FSI diagram for $\vec{p}_m$ values up to $500\frac{MeV}{c}$. In the diagram corresponding to FSI (Fig. 5) the equality $\vec{p}_i = \vec{p}_m = \vec{p}_f - \vec{q}$ does not hold because the rescattering of the two nucleons happens after the interaction between the photon and the proton. In the high energy regime, the amplitude corresponding to single rescattering can be calculated within the eikonal approximation. One such approximation is the Generalized Eikonal Approximation, in which rescattering amplitudes can be calculated using effective Feynman diagram rules [13]. The Feynman diagram representation of the deuteron electro-disintegration in the OPEA modelling is shown in Fig. 13.

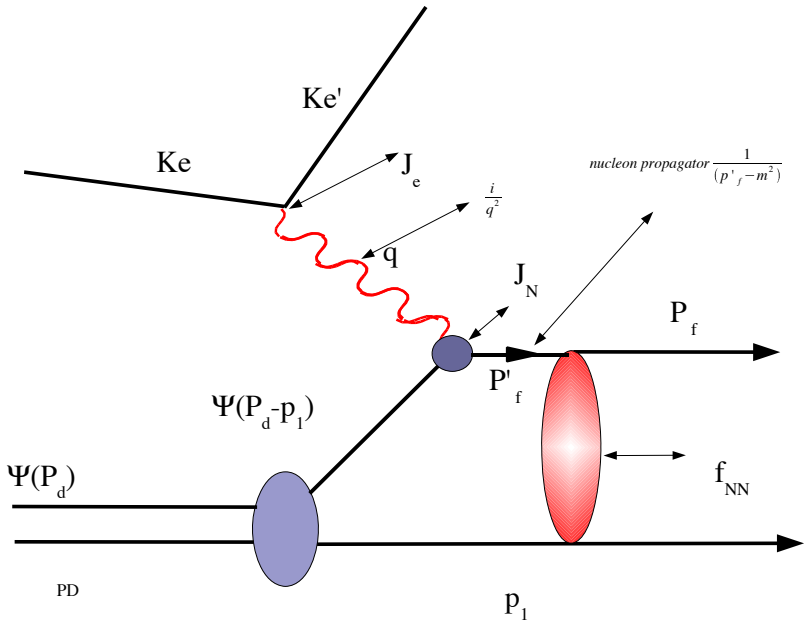

Figure 13: Feynman diagram of the (e,e'p)n reaction in the One Photon Exchange Approximation (OPEA) with FSI effects included.

The corresponding re-scattering covariant Feynman amplitude can be written [13] in the following form:

$$A_1^{\mu} = -\frac{(2\pi)^{\frac{3}{2}}\sqrt{2E_s}}{4i}\int \frac{d^2k_t}{(2\pi)^2} f_{pn}(k_t)\cdot j^{\mu}_{\gamma^* N}(p_D - \tilde{p}_s + q, p_D - \tilde{p}_s)\cdot$$
$$\cdot[\psi_D(\tilde{p}_s) - i\psi'_D(\tilde{p}_s)] \qquad (15)$$

where k_t is the transverse component of the momentum transfered during NN rescattering. The neutron-proton scattering amplitude, f_{pn}, is parameterized in the following form: $f_{pn} = \sigma^{pn}_{tot}(i+\alpha)e^{-\frac{B}{2}(p_3-p_1)^2_{\perp}}$, where σ^{pn}_{tot}, α and B are known experimentally from NN scattering data.

3.3 The Cross Section of Deuteron Electro-disintegration

Assuming the PWIA to be valid (no re-scattering), the differential cross section for $D(e,e'p)n$ reactions factorizes into an elementary $\gamma^* N$ cross section and a spectral function [32, 33, 34]:

$$\frac{d^5\sigma}{dE'_e \cdot d\Omega_e \cdot d\Omega_p} = K\sigma_{ep} S(E_{miss}, \vec{p}_{miss}) \tag{16}$$

where $dE'_e, d\Omega_e, d\Omega_p$ are the phase space factors of the electron and proton, K is a known kinematical factor and σ_{ep} is the off-shell electron-proton cross section. The spectral function $S(E_{miss}, \vec{p}_{miss})$ is defined as the joint probability of finding a proton of momentum, $\vec{p}_{miss}$, and removal (missing) energy E_{miss} within the nucleus. This function contains the nuclear structure information for a given nucleus. This factorization makes the investigation of the nuclear structure very easy. Single-particle distributions can be probed in detail using Eq. 16. Note that for deuteron target $S \sim \Phi_D^2(p_m)$. FSI effects however distort the simple picture following from PWIA. To take into account the FSI effects we start by writing the cross section of the deuteron electro-disintegration reaction using the electron and deuteron electromagnetic tensors as follows [14]:

$$\frac{d\sigma}{dE'_e d\Omega'_e d^3p_f/2E_f d^3p_s/2E_s} = \frac{E'_e}{E_e}\frac{\alpha^2}{q^4}\eta_{\mu\nu} T_D^{\mu\nu} \delta^4(p_D + q - p_f - p_s), \tag{17}$$

where $\eta_{\mu\nu} = \frac{1}{2}Tr(\hat{k}_2\gamma_\mu\hat{k}_1\gamma_\nu)$. $k_1 \equiv (E_e, \vec{k}_1)$ and $k_2 \equiv (E'_e, \vec{k}_2)$ are the four-momenta of incident and scattered electrons respectively.

In this representation, the electromagnetic tensor $T_D^{\mu\nu}$ of the deuteron is given by:

$$T_D^{\mu\nu} = \sum_{spin} (A_0 + A_1)^\mu (A_0 + A_1)^\nu, \tag{18}$$

where A_0 and A_1 correspond to the impulse approximation and single rescattering amplitudes discussed in previous sections. In this case, the bound nucleon's electromagnetic current can be factorized out of the integral in Eq.(15). Then, one arrives to the distorted wave impulse approximation (DWIA), in which the scattering cross section could be represented as a product of the off-shell eN scattering cross section-σ_{eN} and the distorted spectral function-$S_D(p_f, p_s)$.

$$\frac{d\sigma}{dE'_e d\Omega'_e dp_f} = p_f^2 \sigma_{eN} S_D(p_f, p_s). \tag{19}$$

The distorted spectral function can be represented as follows

$$S(p_f, p_s) = \left| \psi_D(p_s) - \frac{1}{4i} \int \frac{d^2 k_t}{(2\pi)^2} f_{pn}(k_t) \cdot [\psi_D(\tilde{p}_s) - i\psi'_D(\tilde{p}_s)] \right|^2 . \tag{20}$$

3.4 Estimation of FSI effects

To analyze the effects of rescattering in the cross section we calculate the ratio of the cross section of Eq.(19) to the cross section calculated within plane wave impulse approximation Eq.(16). Based on the above discussed factorization, for this ratio one obtains:

$$T = \frac{\sigma^{PWIA+FSI}}{\sigma^{PWIA}} = \frac{S_D(p_f, p_s)}{|\psi_D(p_s)|^2}. \tag{21}$$

Figure 14 shows the theoretical calculation of T [14] as a function of the recoil nucleon angle θ_{sq} with respect to $\mathbf{q}$ for different values of recoil nucleon momentum.

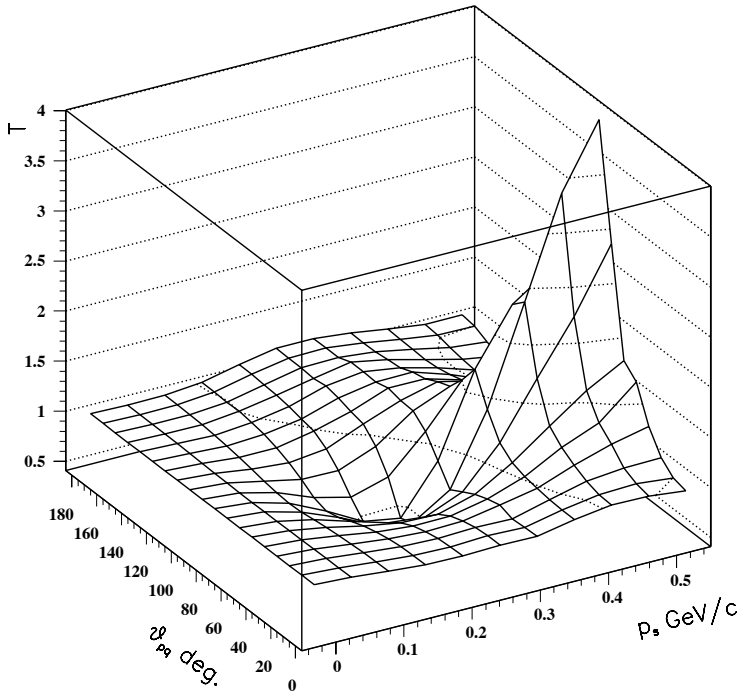

Figure 14: The dependence of the transparency T on the angle, θ_{sq} and the momentum, p_s of the recoil nucleon. The angle is defined with respect to $\mathbf{q}$ [14].

At recoil nucleon momenta $p_s \leq 300 MeV/c$, T has a minimum and generally $T < 1$ while at $p_s > 300 MeV/c$, $T > 1$ and has a pronounced maximum.

In order to understand the behavior of T we can write the cross section of the process, in a simple fashion, as the square of the total amplitude:

$$\sigma \sim S_D \sim |A_{tot}|^2 = |A_0 + A_1|^2 = |A_0|^2 + 2 \cdot ReA_0 \cdot A_1 + |A_1|^2. \tag{22}$$

However, it is known that in the high energy limits f_{NN} is predominantly imaginary $f_{pn} = \sigma_{tot}(i+\alpha)e^{-\frac{B}{2}k_\perp^2}$ with $\alpha \ll 1$. As a result, A_1 becomes negative which results to:

$$\sigma \sim |A_{tot}|^2 = |A_0 + A_1|^2 = |A_0|^2 - 2 \cdot A_0 \cdot A_1 + |A_1|^2 \tag{23}$$

where $|A_0|^2$ is the PWIA term, $2A_0 \cdot A_1$ is the interference or screening term and $|A_1|^2$ is called the double scattering term.

$$\sigma \sim S_D \sim |A_{tot}|^2 = |A_0 + A_1|^2 \tag{24}$$

$$T = \frac{|A_{tot}|^2}{|A_0|^2} = 1 - 2 \cdot \frac{|A_0| \cdot |A_1|}{|A_0|^2} + \frac{|A_1|^2}{|A_0|^2} \tag{25}$$

Inserting Eq.(20) into Eq.(21) one obtains for T:

$$T \approx 1 - \frac{1}{2}\left|\frac{\psi_D(p_s) \cdot \int \frac{d^2k_\perp}{(2\pi)^2} f_{pn}(k_\perp) \cdot [\psi_D(\tilde{p}_s) - i\psi'_D(\tilde{p}_s)]}{\psi_D^2(p_s)}\right| + \frac{1}{4}\frac{\left|\int \frac{d^2k_\perp}{(2\pi)^2} f_{pn}(k_\perp) \cdot [\psi_D(\tilde{p}_s) - i\psi'_D(\tilde{p}_s)]\right|^2}{\psi_D^2(p_s)}. \tag{26}$$

The structure of T is explained by the fact that f_{pn} is mainly imaginary $f_{pn} = \sigma_{tot}(i+\alpha)e^{-\frac{B}{2}k_\perp^2}$ with $\alpha \ll 1$. The importance of the contribution from the PWIA and FSI amplitudes can be very different, depending on the kinematic configuration. The second term in Eq.(26) is the interference term which has a negative sign. In kinematics where the interference term is dominant, the *pn* rescattering results in the screening of the overall cross section, thus $T < 1$. The maximal screening is found at $p_{st} \approx 200 MeV/c$ at which the square of rescattering term (third term in Eq.(26))

is small, and $T \leq 1$. As p_s increases, the relative contribution of the square of the rescattering term becomes dominant and T becomes larger than 1. The rescattering term becomes larger than the interference term due to the fact that the interference term, in T, grows as $\sim 1/|\psi_D(p_s)|$ while the rescattering term is $\sim 1/|\psi_D(p_s)|^2$.

4 Experimental setup

4.1 Overview

Experiment E01020 was carried out at the Thomas Jefferson National Accelerator Facility (JLab) in Newport News, Virginia, Hall A, in the Fall of 2002. The accelerator can provide high quality continuous wave (CW) electron beam simultaneously to the three experimental halls. The average electron beam current delivered to Hall A for this experiment was ~ 100 μA.

The accelerator at Jlab can accelerate electrons up to 6 GeV by recirculating the beam for a total of five passes through two superconducting linear accelerators (linacs), each producing an energy gain of 600 MeV per pass. After passing through the first linac the electrons are focused and separated according to their energies by a magnetic field in the recirculation arcs and redirected to the second linac (see Fig. 15). When the desired energy of the beam is attained, the beam is delivered to one of the three experimental halls. The two linear accelerators consist of twenty cryomodules each. There are eight superconducting niobium cavities in each cryomodule. The

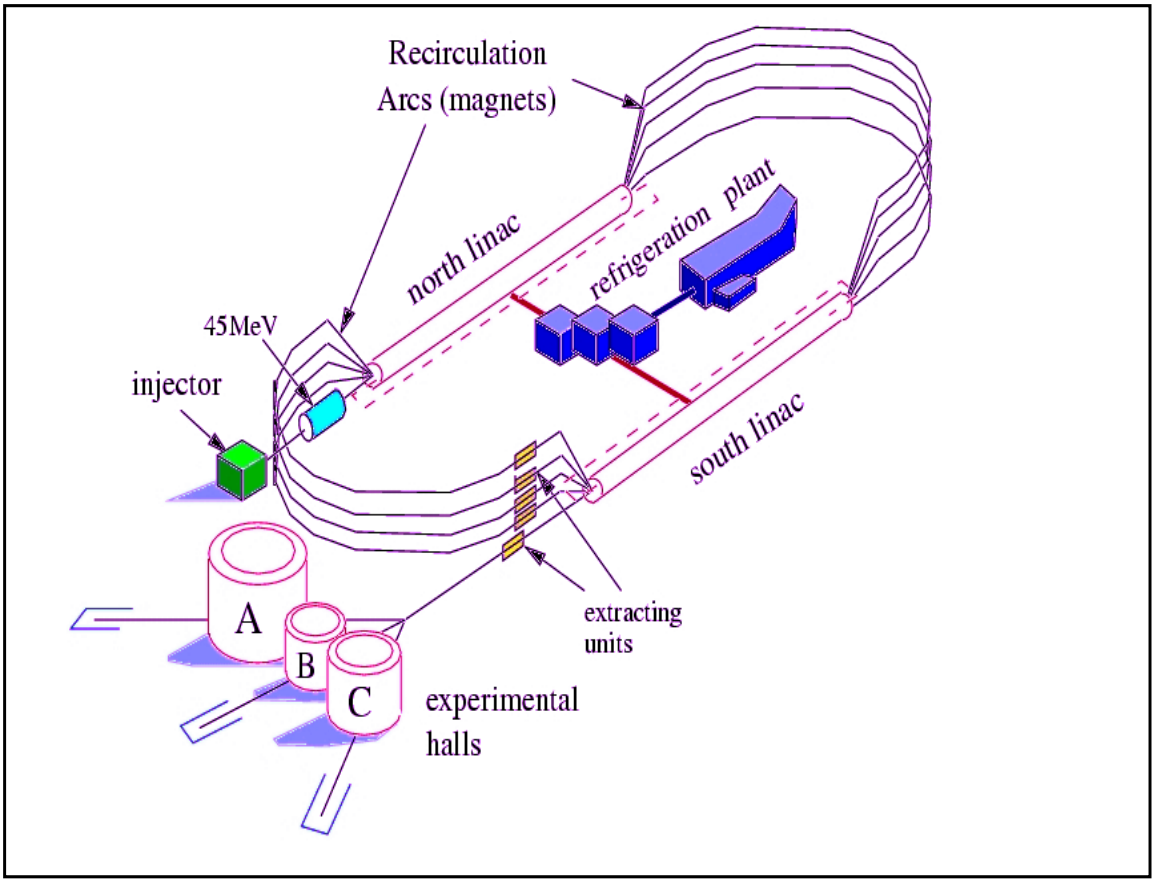

Figure 15: The accelerator at Jefferson Lab [35].

cavities are cooled down to a temperature of 2 K. The radio waves which drive the cavities, have a frequency $\nu_{RF} = 1.497$ GHz. This frequency yields a distance between the electron packets, $\frac{c}{\nu_{RF}} = 20.04$ cm. In contrast to earlier linear electron accelerators, which produce a pulsed electron beam, the CW beam delivered by Jlab has no pulse structure (besides its micro structure due to the HF electric field used in the accelerator cavities). The micro structure of the beam consists of short (1.67 ps) bursts of beam. For coincidence measurements such as the one in this experiment the signal-to-noise is one of the most important parameters. The pulsed electron beam

accelerators used in the past are not suitable for coincidence experiments when the cross section to be measured is very small and the instantaneous rates in the detectors were very high [36]. The range of the beam current is from 1 μA to 190 μA. For the E01-020 experiment the beam energy was 5.0 GeV.

4.2 Beam energy measurement during E01-020

Precise information on the energy and the current of the incident electron beam is essential for accurate cross section measurements. For the E01-020 experiment, the beam energy was measured by two independent methods. One method is the arc energy measurement and the second method is the *ep* method. The beam energy measurement by the arc method is done in the arc section of the beam line and is performed by deflecting the electron beam in a known magnetic field. The bending angle of the beam is 34.3^o. The momentum of the beam is calculated knowing the magnitude of the magnetic field and the net bend angle through the arc. The systematic (absolute) uncertainty for the arc energy method ranges from 6.8×10^{-5} GeV, at an incident energy of 4 GeV to 1.2×10^{-4} GeV, at an incident energy of 5 GeV [37].

The *ep* method to measure the beam energy is based on elastic scattering of the electron beam off a proton target. This method employs two sets of detectors symmetrically placed about the nominal beam direction. The scattered electron and recoil proton are detected in a pair of detectors on either side of the beam, and the

other pair of detectors is placed at a complementary angle (symmetric about the beam). Ideally both detector pairs should measure the same value of the incident energy. However, if the beam direction does not coincide with the symmetry axis of the detector array, each pair will measure a different energy. For a given pair, the energy can be expressed in terms of the electron and proton angles with respect to the beam, θ_e and θ_p respectively. The energy of the beam is determined from two-body kinematics [38]:

$$E = M_p \frac{\cos(\theta_e) + \frac{\sin(\theta_e)}{\tan(\theta_p)} - 1}{1 - \cos(\theta_p)} \tag{27}$$

The relative energy $\frac{\delta E_{beam}}{E_{beam}}$ can be determined up to an accuracy of 2×10^{-4} [37]. The two methods of beam energy measurements agree with each other within 3×10^{-4} (relative uncertainty).

4.3 Beam current monitor

To monitor the beam current a parametric DC current transformer monitor (Unser monitor), a pair of cavities, the associated electronics and a data acquisition system were used. This beam current monitor device, (BCM), is described in detail in the Hall A Operational Manual [39]. The beam current was measured with three resonant cavity beam current monitors (BCM 1, 2 and 3) and with the Unser monitor. The Unser monitor is designed for non-destructive beam current measurement and providing an absolute reference. The monitor is calibrated by passing a known current through a wire inside the beam pipe and has a nominal output of 4 mV/μA.

As the Unser monitor's output signal drifts significantly on a time scale of several minutes, it cannot be used to continuously monitor the beam current. The more stable cavities are then used to determine the beam current and charge for each run. Two resonant cavity monitors are placed on either side of the Unser Monitor acting as waveguides. The cavities are tuned to the frequency of the beam (1.497 GHz) resulting in voltage levels at their outputs which are proportional to the beam current. The output from the cavities is converted into an analog DC voltage level. The regular RMS to DC output is linear only for currents from about 5 μA to somewhere well above 200 μA. Because is non-linear for lower currents a set of amplifiers with differing gains (x3 and x10) was introduced thus extending the non-linear region to lower currents. There are 3 signals coming from each BCM, the unamplified BCM1 and the amplified BCM3 and BCM10 signals. The beam current monitors are used to determine the beam charge during a run having known the acquisition time for each run. The BCM final signals are stored in the EPICS data stream. The ratio of the unamplified and amplified (times 3) charge readings is shown in Fig. 16.

4.4 Beam position monitor-BPM and rastering

To determine the position and the direction of the beam on the experimental target point, two Beam Position Monitors (BPMs) are located at distances 7.524 m and 1.286 m upstream of the target position [39]. The BPMs consist of a 4-wire antenna array of open ended thin wire strip lines tuned to the fundamental RF frequency of 1.497 GHz of the beam. The relative position of the beam is determined to within

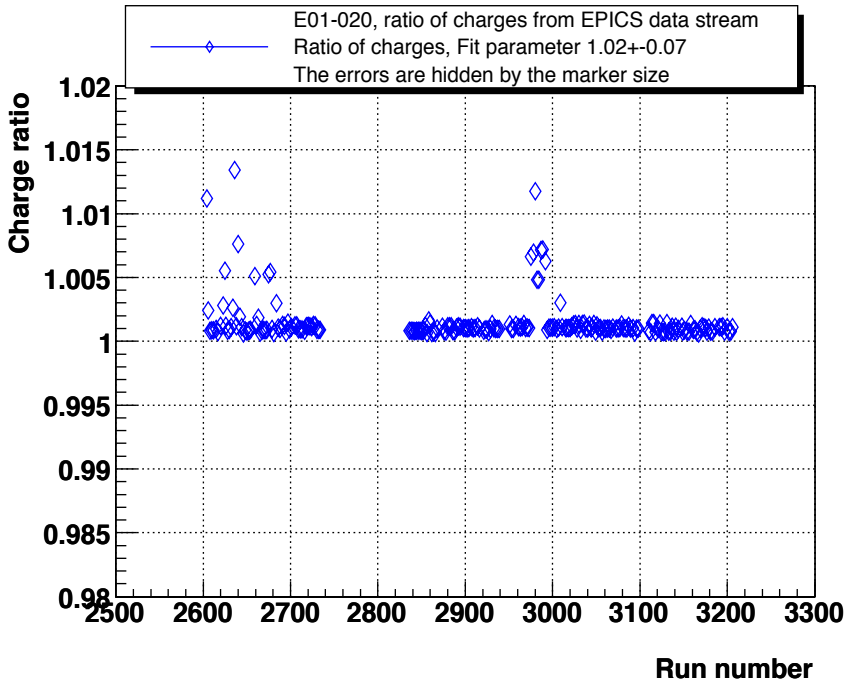

Figure 16: Ratio of the charge measurements as extracted from the EPICS datastream for the E01-020 experiment.

100 μm for currents above 1 μA. The absolute position of the BPMs can be calibrated with respect to the scanners (superharps) which are located adjacent to each of the BPMs at 7.353 m and at 1.122 m, respectively, upstream of the target.

A superharp consist of a frame (fork) and three tungsten wires along with its associated electronics. Two of them measure the beam profile in the horizontal Y direction, the third one in the X direction. When the fork is moved in the beam by the stepper motor, each wire crosses the electron beam and secondary emitted electrons produce a signal that is detected and amplified. The positions of the wires are accurately known, which makes absolute position measurements possible and allows one to determine the widths of the beam in the X and Y directions.

An Analog-to-Digital Converter (ADC) measures the signal on the wires and a position encoder measures the position of the ladder as they pass through the beam. Using the position and the ADC information measurements, the position and profile of the beam are extracted. The accuracy of the beam position given by superharp readout is ~ 10 μm. This is adequate for reconstructing the actual width of the beam which is ~ 100 μm (FWHM) in both directions. The scanners are surveyed on a regular basis and determine the absolute position of the beam in the Hall A coordinate system. The information that the BPMs provide is periodically written into the EPICS data stream (every 3-4 seconds) with a time stamp. At the location of the experimental target, a BeO target on the target ladder provides a visual beam spot. When the liquid deuterium target was used, the incident electron beam was rastered in the horizontal and vertical directions to distribute the deposited heat and to prevent large local density fluctuations in the liquid target. The rastering is achieved by a set of coils placed in the beam line in the horizontal and vertical plane. A triangular current passes through the coils, generating a magnetic field which deflects the incident electron beam. The unrastered size of the beam was $\sim$ 100 μm. The rastering system used frequencies of 17.7 kHz and 24.4 kHz for the horizontal and vertical directions respectively. During the E01-020 experiment the beam raster's size was 2.0×2.0 mm^2 or 4.0×4.0 mm^2 (Fig. 17).

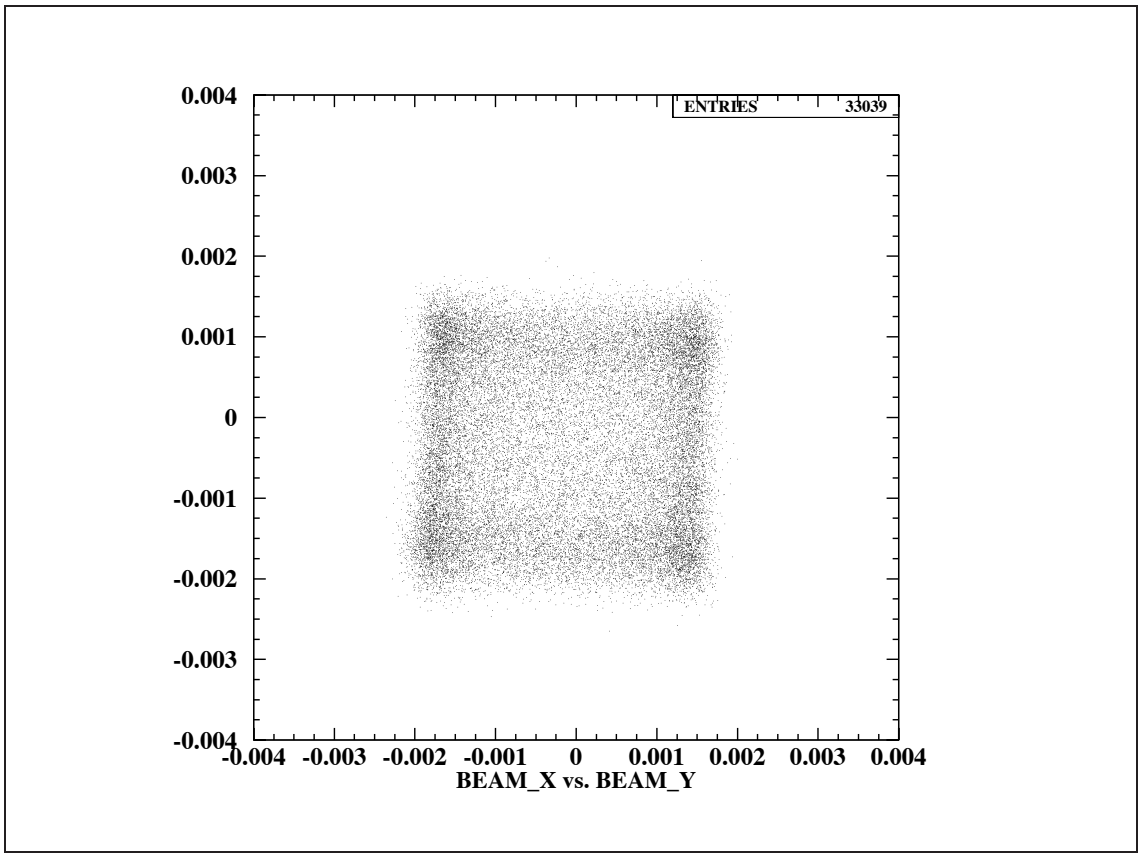

Figure 17: Rastered beam size 2.0×2.0 mm^2 on target for E01-020.

4.5 Target

The target assembly used during E01020 consisted of a target ladder (see Fig.18) with liquid cryogenic and solid targets. Remotely controlled stepper motors allowed the vertical movement of the ladder such that the desired target could be positioned in the beam path. On the ladder there were three target loops each containing a long ($\sim$ 15 cm) and a short ($\sim$ 4 cm) cylindrical cell and various solid targets. The axes of the loops are along the beam direction. The loops were filled with liquid helium, liquid hydrogen and liquid deuterium. The two cells usually filled with liquid ^{4}He, were not operational during E01020. The liquid deuterium target,

H_2, was used for production runs and solid targets were used for optics studies, calibrations, and background subtraction. A target cell replica, made of aluminum, is used to correct the data taken with liquid deuterium cell for contributions from the aluminum walls. These so called "dummy" targets are flat aluminum targets placed at the approximative position of the endcaps of the cryotargets and made of the same type of material as the endcaps themselves. The thickness of the aluminum in the "dummy" targets is about ten times the thickness of the walls of the cryogenic target. The thickness of the aluminum in the "dummy" targets is chosen such that the time dedicated to empty target measurements is significantly reduced when comparing to "production" data acquisition time. The ^{12}C target was used for optics studies (see section 4.9.1). When the beam is incident on a BeO target, it causes the target to glow. This target is used for a visual inspection of the beam position. At the bottom of the solid target ladder is the empty target, which is essentially an aluminum foil with a circular hole cut in it through which the beam goes straight through the scattering chamber to the beam dump.

The entire target system is installed inside a scattering chamber together with the cooling and gas handling systems, temperature and pressure sensors. The scattering chamber is a large cylinder (inner radius $\sim$ 100 cm) and a height of $\sim$ 90 cm) with relatively thick aluminum walls ($\sim$ 5 cm). The main purpose of the scattering chamber is to protect thermally and mechanically the targets used in physics experiments. The chamber has openings for the entrance/exit of the beam such that the beam passed through no material before interacting with the target (except the

target wall). There are several windows for the visual inspection of the target and a pumping port for attaching the vacuum pumps. Scattered particles exited the scattering chamber through thin aluminum windows (each window was 18 cm tall). The scattering chamber exit windows for both the electron and hadron spectrometer were made of 40 μm thick aluminum sheet (5052-H34 alloy, density: 2.68 g/cm^3).

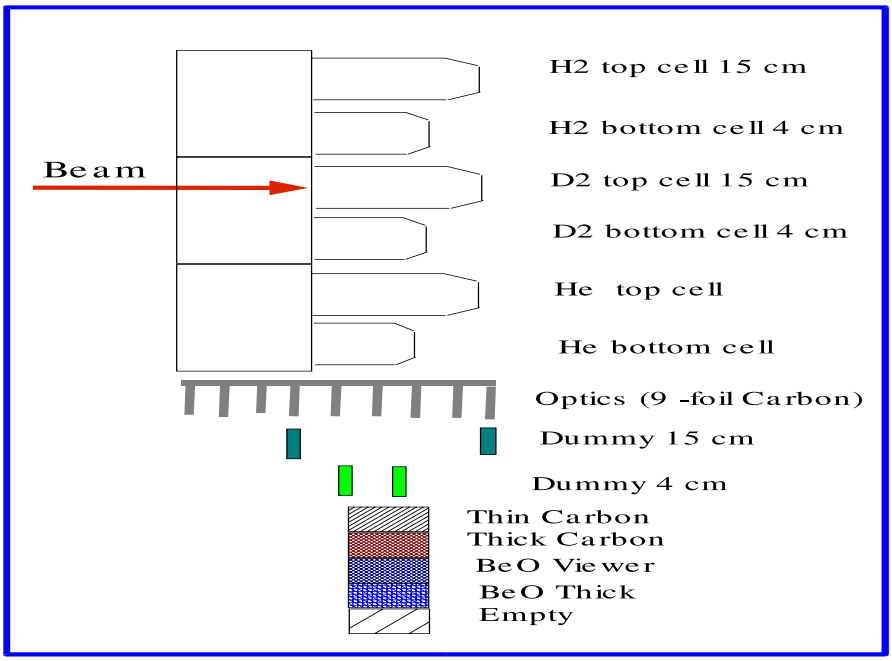

Figure 18: Hall A schematic of the target ladder.

The loops were mounted on a common aluminum cell block which was connected to a heat exchanger. An axial fan mounted inside the heat exchanger forces the target liquid to circulate through the cells. The target fan speed was fixed at 60 Hz.

4.6 Hall A high resolution spectrometers

The Hall A experimental apparatus is described in reference [37] and only a short overview will be given here. During experiment E01-020 the scattered electrons and the knockout protons were detected in coincidence in two High Resolution Spectrometers (HRS). The spectrometers have similar detector packages, consisting of

- Vertical Drift Chambers (VDC) for particle track reconstruction
- A gas Cerenkov detector for electron-pion discrimination
- A lead glass detector for particle identification purposes

The hadron HRS stack includes a third scintillator plane, S0. The S1 and S2 scintillator planes utilize 2" photomultiplier tubes while the S0 plane has 5" PMTs. The basic layout of the HRS's is shown in Fig. 19. The HRS are designed for high resolution measurements of particle momenta, particle angles, and positions. The HRS is composed of three superconducting quadrupole magnets, Q1, Q2, and Q3, and one superconducting dipole magnet(QQDQ configuration). The design value for the maximum momentum accessible to the HRS magnet system is 4 GeV/c. The quadrupoles provide some of the focusing properties of the spectrometer and to a large extent its momentum acceptance. The central momentum measured by the spectrometer (P_0) is related to the central magnetic field by the constant of the spectrometer: $P_0 = \Gamma B_0$. Both of the HRS have proven to provide a momentum resolution of better than 2×10^{-4}, and a horizontal angular resolution of better

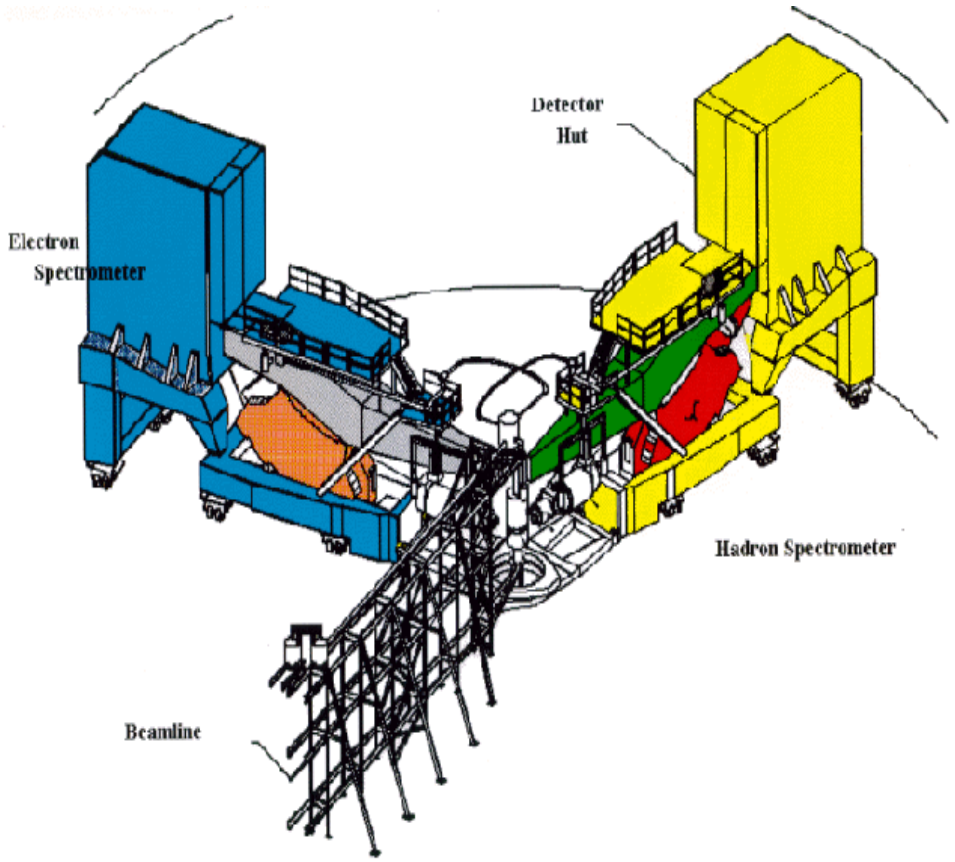

Figure 19: Thomas Jefferson National Laboratory Hall A High Resolution spectrometers [35].

than 2 mrad with a design maximum central momenta of 4 GeV/c. The selection of a charged particle depending on its momentum is achieved by the curvature of a charged particle traveling through the dipole magnetic field which is proportional to the particle's momentum. The dipole field can be set to any central momentum value between 0.3 and 4.0 GeV/c. The central ray particle trajectory is the reference for the symmetry plane of the spectrometer system. The path length of a particle entering the spectrometer system and following the path of a central ray is 23.4 meters between the target and the spectrometer's exit window.

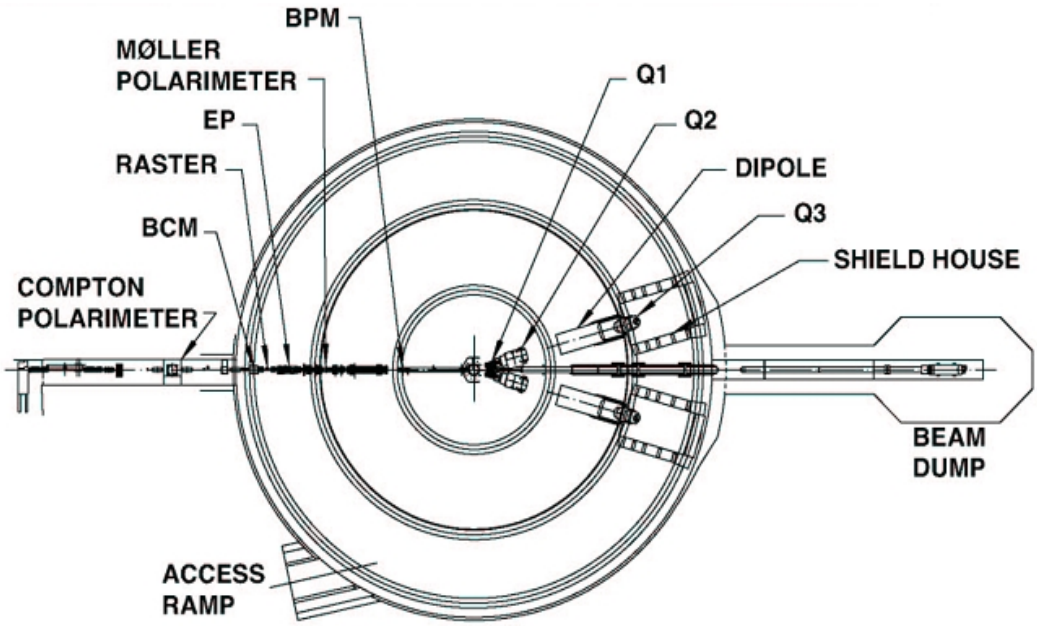

Figure 20: Schematic layout of Hall A indicating the instrumentation along the beam line [37].

HRS General Characteristics	
Configuration: QQDQ	Horizontal angular acceptance: ±28 mr
Bending angle: 45^0	Vertical angular acceptance: ±60 mr
Momentum range: 0.3 - 4.0 GeV/c	Solid angle (rectangular shape): 6.7 msr
Optical length: 23.4 m	Horizontal angular resolution: 0.6 mr
Momentum resolution (FWHM):	2.5×10^{-4}

Table 1: General characteristics of the Hall A spectrometers.

The role of the spectrometers is to select, record, and identify particles emerging from a reaction in the target within a certain phase space in momentum and solid angle which is defined by the acceptance of the spectrometer. The quadrupoles determine the transverse and in-plane focusing properties of the spectrometer and, to a large extent, its acceptance. Q1 and Q2 focus in the non-dispersive (horizontal) direction while Q3 focuses in the dispersive (transverse) direction. A schematic layout of the

quadrupoles and dipole is presented in Fig. 20. The scattering angle of the incident particles can be varied between 12.5^0 and 125.05^0 by rotating the entire spectrometer around the Hall A center. The general characteristics of the Hall A spectrometers are listed in Table 1 [37].

4.7 Detectors package

The detector packages used during the E01-020 experiment are listed in tables 2 and 3.

Detector Configurations for E01-020 (see Fig. 21 and 22)
Right arm (hadron arm) for detecting protons :
VDC: Two Vertical Drift Wire Chambers S1, S2, S0: Trigger scintillator counters A1: 1st Aerogel Cerenkov counter, $n = 1.015$ (fall running period only) A2: 2nd Aerogel Cerenkov counter (spring running period only), $n = 1.0554$

Table 2: Detector package for HRS hadron arm

Left arm (electron arm) used for e^- and π^- detection:
VDC: Two Vertical Drift Wire Chambers S1, S2: Trigger scintillator counters GC : Gas Cerenkov counter (1 m long), $n = 1.0004$ Pion rejector counter

Table 3: Detector package for HRS electron arm

The hadron arm detector package is illustrated in Fig. 21 and the electron arm detector package is shown in Fig. 22. Both packages include two vertical drift chambers (VDCs) that provide a precise measurement of the position and angle of the knock-out hadrons (scattered electron) at the spectrometers focal plane. This information is further combined with the knowledge of the spectrometer optics to determine the

position and angle of the particles at the target. Scintillator detectors were used in both arms to select coincident events.

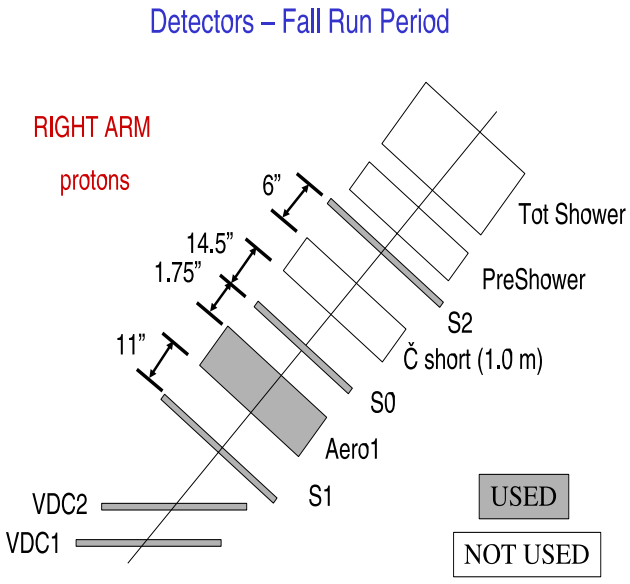

Figure 21: Detectors configuration during E01-020, hadron (right) arm.

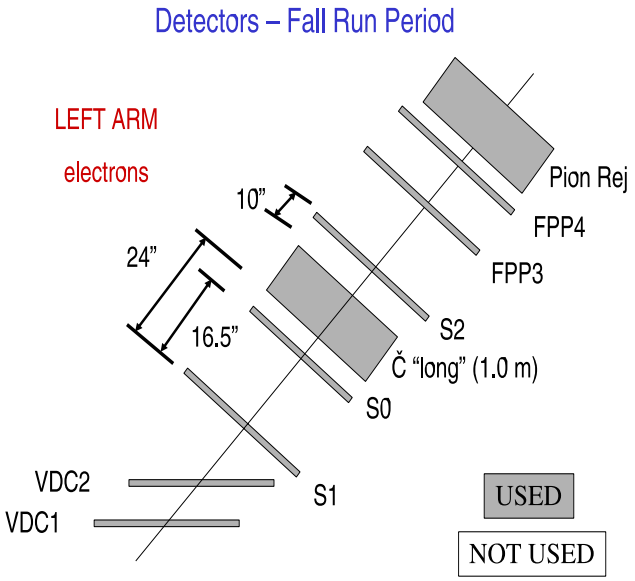

Figure 22: Detectors configuration during E01-020, electron (left) arm.

In the electron arm spectrometer additional gas Cerenkov and lead-glass shower counters were used for electron/π^- discrimination.

4.7.1 Scintillator detectors

Each of the HRS detector packages (hadron arm and electron arm) contains two planes of trigger scintillators $S1$ and $S2$ (see Fig. 23) that were used to generate the trigger and to provide the time-of-flight (TOF) information between the two arms. The TOF between the electron and the hadron arm scintillators was used to identify e-p coincidences. Plane S1 consists of six counters (paddles) with the dimensions

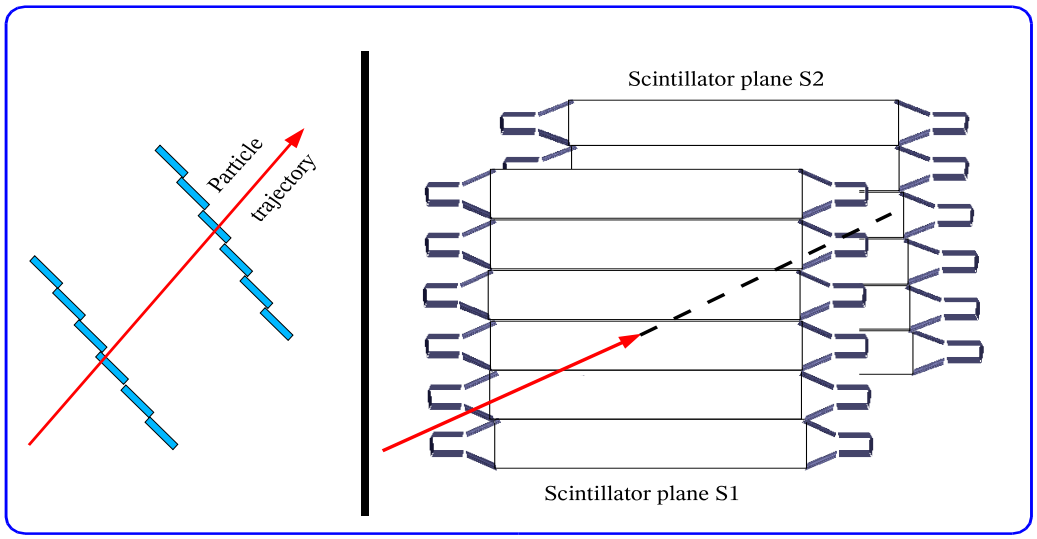

Figure 23: Schematic layout of the scintillator detectors.

0.5 cm × 30 cm × 36 cm and plane S2 has six counters with the dimensions 0.5 cm × 37 cm × 60 cm. Each counter is viewed from both ends by 2 inches Burle 8575 Photomultiplier Tubes (PMT) with a time resolution of 200 ps per plane. Plane S0 in the hadron arm consists of nine counters 2.5 cm × 40 cm × 155 cm viewed

from both ends by 5 inches PMT Burle 8854. When charged particles pass through the paddles, they ionize the atoms in the material. The liberated electrons excite molecular levels in the scintillator, which decay back by light emission. The light emitted along the length of the paddles will be collected by PMTs, one at each end of the bar. The light that is not emitted along the length of the paddle, but hits the surface of the scintillator at greater angles than the critical angle, will be completely reflected and will also reach the PMTs. The HMS scintillators are wrapped with one layer of aluminum foil and two layers of Tedlar to make them light tight.

The scintillator planes are perpendicular to the spectrometer central ray. The time necessary for a particle to travel the distance between the two scintillator planes allows the calculation of the speed of the particle. The first scintillator plane, S1, is located at a distance of 1.5 meters from the center of the first VDC plane. The second scintillator plane, S2, is located at a distance of 3.5 meters from the center of the first VDC plane. The active area of the first scintillator plane is about 170 $\times$ 35 cm^2 whereas the active area of the second scintillator plane is about 220 $\times$ 54 cm^2.

The scintillator paddles are narrow strips (5 mm) of $BC404$ scintillator material (polyvinyl toluene, PVT) with acrylic light guides at each end. The paddles overlap over a 5 mm region to maximize efficiency.

4.7.2 Vertical drift chambers

The HRS tracking detectors consist of two vertical drift chambers (VDCs) that provide a precise measurement of the position and angle of both recoil electron and

knockout hadron. This information, combined with the knowledge of the spectrometer optics, determines the position and angle of the particles at the target. Each of the two vertical drift chambers used for particle tracking is composed of two wire planes, U and V. The distance between the U and V wire planes is 26 mm. The wires of the V planes are perpendicular to the wires of the U planes, and all wires make an angle of 45^o with respect to the dispersive and transverse directions (see Fig. 24). The VDCs in each arm are 50 cm apart from each other. The gas mixture flows

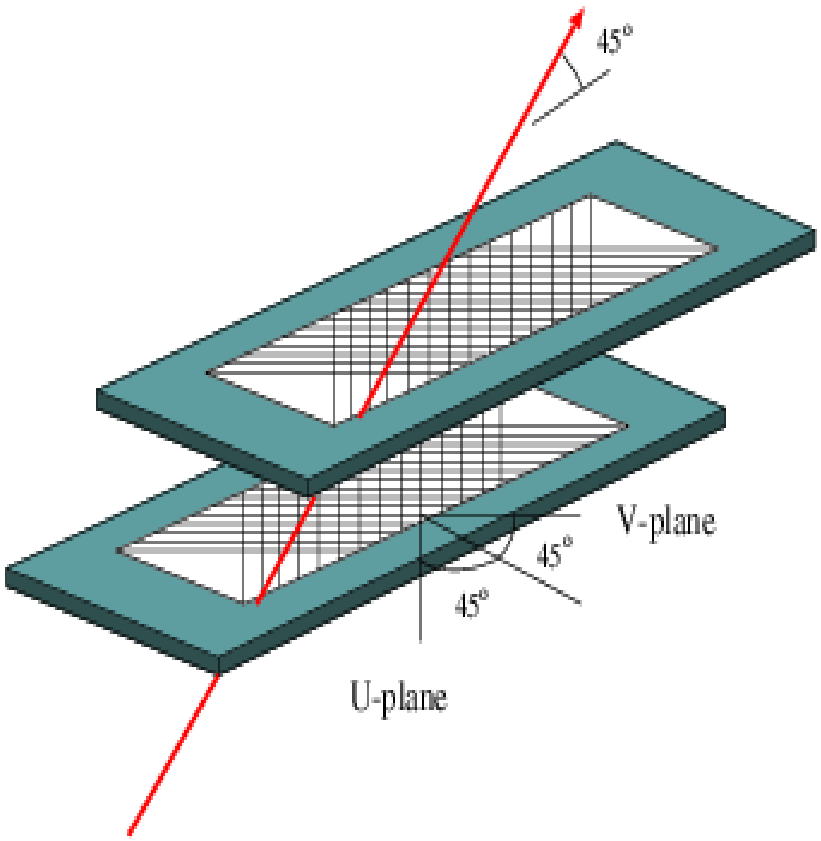

Figure 24: VDC U and V planes [35].

continuously with a rate of 10 l/hour. As charged particles pass through the chamber gas in the VDCs, they ionize a large number of molecules. The electrons produced

by a particle along its path drift to the anode along the direction of the electric field lines defined by the high voltage planes and the signal wires. The electric field lines are mainly perpendicular to the wire plane, except in the vicinity of the wire. The potential difference between the cathode planes and the wires is approximately 4 kV. Close to the anode wire, the electric field is so strong that that the electrons can ionize other atoms and molecules of the gas and produce an avalanche of electrons. The primary ionization is amplified with a gain of the order 10^6. The drift direction is perpendicular to the wire plane. Therefore, the largest drift distance is determined by the distance between the wire plane and the cathode plane (see Fig. 25). The drift time is recorded by a Time to Digital Converter (TDC) which is triggered by the wire that fired, and stopped by the scintillator trigger. The drift distance can be calculated from the drift time (see Fig. 25).

The charge is collected in the form of analog pulses on the signal wires. By knowing the drift velocity of the electrons in the argon-ethane mixture, the distance from the wire that fired to the particles trajectory is extracted from the corresponding TDC reading. The drift chamber TDCs measure the time that the wire detected the electrons created by the ionization of the chamber gas, relative to the time of the trigger. Using the scintillator TDCs to determine the time that the particle passed through the focal plane (relative to the trigger), we can determine the time it took for the electrons created by the ionizing particle to 'drift' to the wire. This drift time is converted into a drift distance. By calculating the distance for all the wires that fired when a particle passed through the VDC the trajectory of the particle

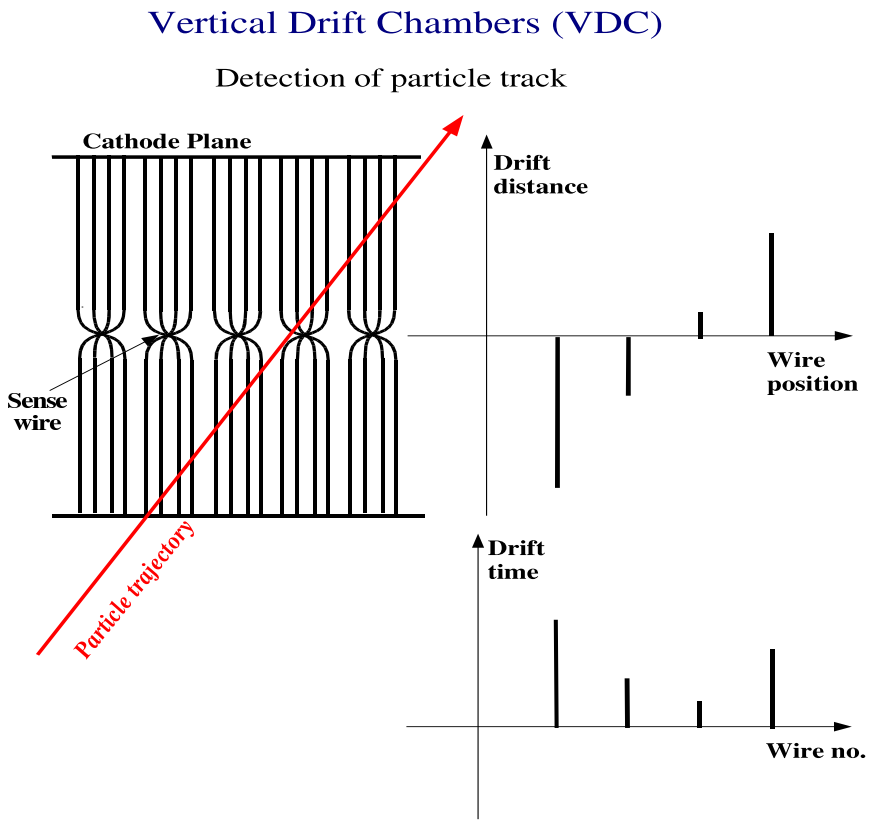

Figure 25: VDC - Determination of particle track from the drift time.

can be determined (see section 4.11). The angular resolution of the VDC (FWHM) is approximately 0.3 mrad. The position resolution in the dispersive and transverse directions is 225 μm (FWHM)[40].

4.7.3 Gas Čerenkov

The Cerenkov detector follows the scintillation detectors (Figures 21 and 22), and is used to discriminate between electrons and pions and to remove the cosmic background contribution in single-arm measurements. Cerenkov light is generated in the radiator gas (CO_2). The index of refraction for CO_2 at atmospheric pres-

sure is $n = 1.00041$. The Cerenkov angle can be determined from the equation $cos(\theta_{Cher}) = 1/(n \cdot \beta)$ [41], where n is the refraction index and β is the particle velocity in units of c. The cone's oppening angle is calculated from the particle velocity and the index of refraction of the gas: $\theta = arccos\frac{1}{\beta \cdot n}$. For the known refraction index, the threshold β, to produce Cerenkov light is determined to be $\beta_{Thr} = \frac{1}{n} = 0.99959017$. This corresponds to a momentum threshold, $p_{Thr} = \frac{m_0 \cdot c}{\sqrt{1-\beta^2}} = 4.8$ GeV/c for producing Čerenkov radiation by π in the Gas Čerenkov detector (m_0 is the rest mass of the particle).

4.7.4 Lead-Glass Shower Counter

The lead-glass shower counter, also used to separate electrons from pions and other backgrounds, consists of 40 blocks arranged in a 4 $\times$ 10 array on an aluminum base. Each block was 10 $\times$ 10 cm^2 in cross section and 25 cm long. They were made of DF6 -type lead glass with a density of $\rho = 5.18\ g/cm^3$.

High energy charged particles interact with matter mainly through bremsstrahlung and pair production, respectively. Each of these processes create photons and electrons (positrons) which further interact similarly, thus producing a shower (cascade) of secondary particles. The lead-glass counter detects the energy deposited when an electron enters the lead-glass. A high energy electron will radiate photons through Bremsstrahlung in the calorimeter, which will in turn generate positron-electron pairs. These pairs will also radiate photons, and a shower of particles (photons, electrons, and positrons) will be generated. The PMTs on the lead-glass blocks detect

the Cerenkov light given off by the charged particles. This signal is proportional to the total track length of charged particles in the calorimeter (for particles above the Cerenkov threshold) which is in turn proportional to the energy of the initial electron.

4.8 Experimental data acquisition

The tool used to convert the electronic signals from the detectors to a physics event recorded on a disk is the CEBAF ON-line Data Acquisition (CODA) system [42]. The CODA data acquisition system uses hardware Read Out Controllers (ROC's), an event builder (EB) and an online analyzer. The function of a ROC is to read the processed signals from the detectors and transffer it to the recording computers. The EB combines the information coming from the ROC's and incorporates it into a common event format. The online analyzer system has the purpose to analyze and write the data to the hard drive, from where it is transferred to larger storeage devices (tapes). The online analyzer package analyzes the data while acquiring it. This allows one to monitor the status of the equipment used in the experiment such as target position, magnet currents, detector high voltages, beam energy, beam position and scalers.

4.8.1 Data acquisition system

A network of computers is used to run the CODA acquisition system which is controlled by a single Run Control process. The Run Control function is to run the

subsystems ROCs, event builder (EB) and event analyzer (EA) and event recorder (ER) (see Figure 26). The signals from the detectors are proccessed by the monitoring electronis consisting of commercial Analog to Digital Convertors (ADCs), Time to Digital Convertors (TDCs) units and scalers in FASTBUS and VME crates. The FASTBUS interface can read out up to 10,000 detector channels. The system requires over 20 front-end crates (FASTBUS and VME). The Readout Control (ROC) software is an interface to Front-End crates. There are three independent ROCs, each of them reading/recording a fragment of the information associated with an event. The data from each ROC are sent to the EB which checks to detect missing data. The ER writes the data for each event to the disk. In addition to the physics event information beam related devices were read out on an event by event basis (BCM monitors and the beam raster). The spectrometer magnet settings, along with the target information (temperature, pressure, coolant flow) were accessed and sent into the data stream as well.

4.8.2 Trigger Setup

The single arm and coincidence triggers in Hall A are schematically displayed in Fig. 27. The PMT anode pulses from scintillators provided the primary detector signals. The signals from the detectors were delivered to the ADCs and to a discriminator. The discriminator sets an output whenever it detects a signal greater than its threshold whose leading edge lies within a narrow time window. The discriminator threshold, the window width and offset are all controlled via VME settable registers.

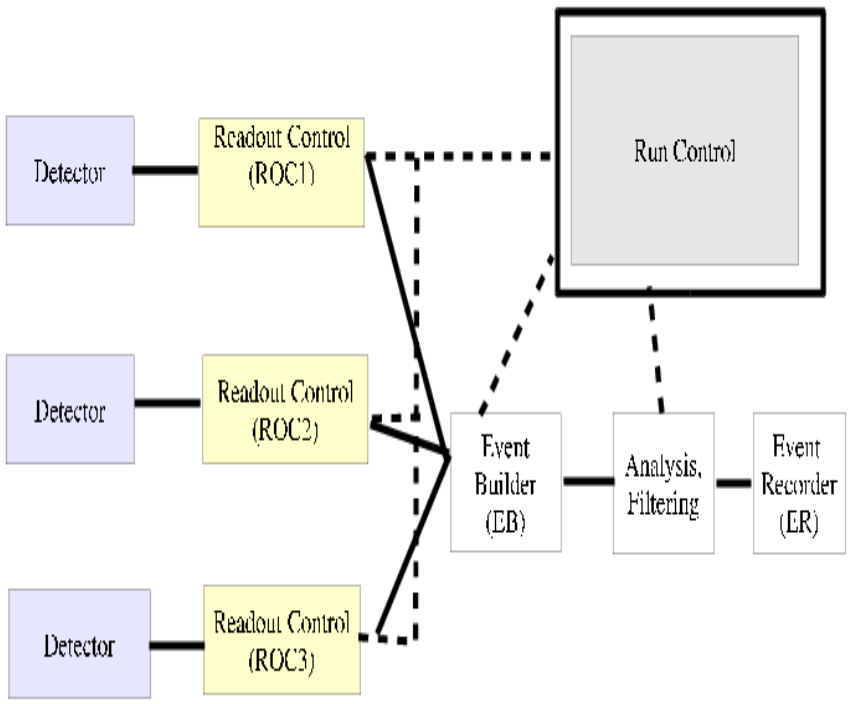

Figure 26: Data flow diagram: controllers called *Readout Controllers* (*ROCs*) read out different components of a detector. The data buffered in the controller is transmitted over the network to be analyzed [42].

The discriminator time-over-threshold signals are compared to signals coming from other scintillator detectors. For coincidence experiments a coincidence is formed between the spectrometer arms. The main trigger is formed by requiring that scintillator planes S1 and S2 both fired. So, this means that one requires that one paddle in S1 and one in S2 both got a hit in both of their PMTs (4 PMTs in total). The coincidence between spectrometers is formed in an overlap AND circuit. The Right Spectrometer singles triggers are called T1, the Left Spectrometer triggers are called T3, and the coincidence triggers are T5. Other triggers can be formed which require other detectors in order to measure the efficiency of the main trigger. The most important is T2 on the R-arm and T4 on the L-arm, whose definition has changed

over time. For our experiment the trigger T2 is formed when 2 out of 3 detectors fire from among the S1, S2, and a 3rd detector like S0 or the Cerenkov detector. The Hall A HRS trigger system is remotely configured by CAMAC modules. During an experiment delays need to be adjusted for the timings of triggers that change with particle momenta and particle ID. These delays are relevant for coincidence setup only. The signals from the detectors are then put into the Memory Logic Units (MLUs). The output of the MLUs for this experiment are ORs and ANDs of all detectors, which had a hit in them. The memory lookup units (MLU in the Fig. 27) in each spectrometer arm generated a logical output ($S-ray$) when both PMT's of a scintillator paddle (in the first scintillator plane $S1$) fired and both PMT's (in the second scintillator plane $S2$) of an adjacent or coincident paddle fired.

The coincidence trigger, $T5$, is formed by sending the single arm S-ray triggers (described above) to a logical AND unit. There is a time window setup of approximately 100 ns for the coincidence to be accepted as such. The number of events for every trigger type is recorded by a running scaler, which is read and logged by the DAQ every 10 seconds. Although all triggers can fire the DAQ, T5 has priority while other triggers are prescaled, which means only a fraction of these events are recorded. This fraction is set using prescale factors (PS1, PS2, PS3, PS4 and PS5). The encoding of the analog signals and the transfer of the digitized signal to the computer buffers takes $\sim 700\mu$s. During the E01-020 experiment all triggers were prescaled except for the coincidence trigger, $T5$.

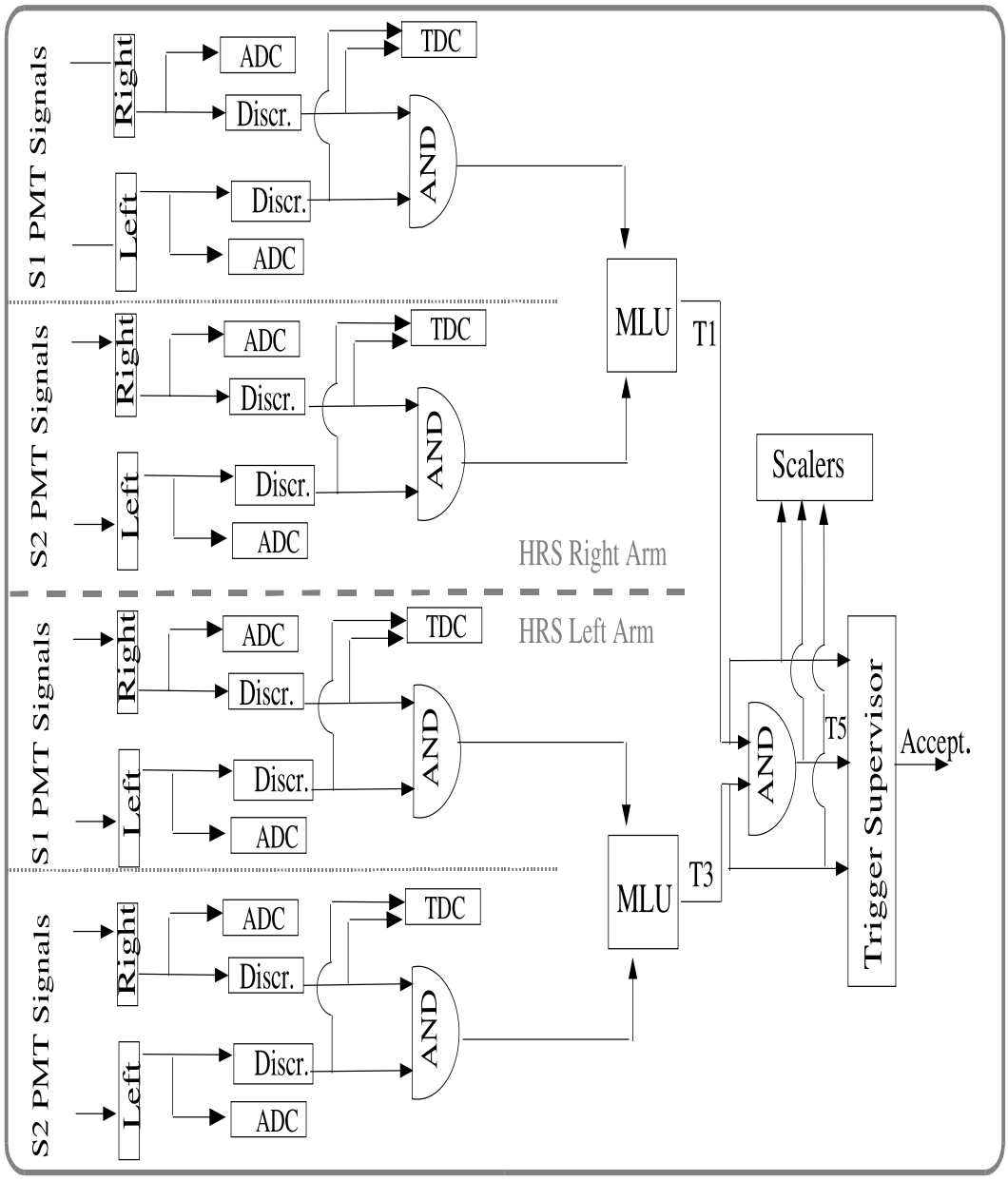

Figure 27: Single arm and coincidence triggers for E01-020.

4.8.3 Electronic and computer deadtime

Dead time is the time during which the DAQ has to reject valid events because it is not yet ready to process them. This occurs when either the trigger electronics is still

processing the previous event and is not able to accept the new event (Electronic Dead Time - EDT), or because the trigger supervisor is still processing the signals from the previous event and writing it to disk (Computer Dead Time -CDT). The life time is defined as 1-DT. The deadtimes, EDT and CDT occur when the rates are high (larger than 10 KHz) and the detection system is not able to keep up with these rates. The data analyzed in this dissertation were mostly at low rate. For

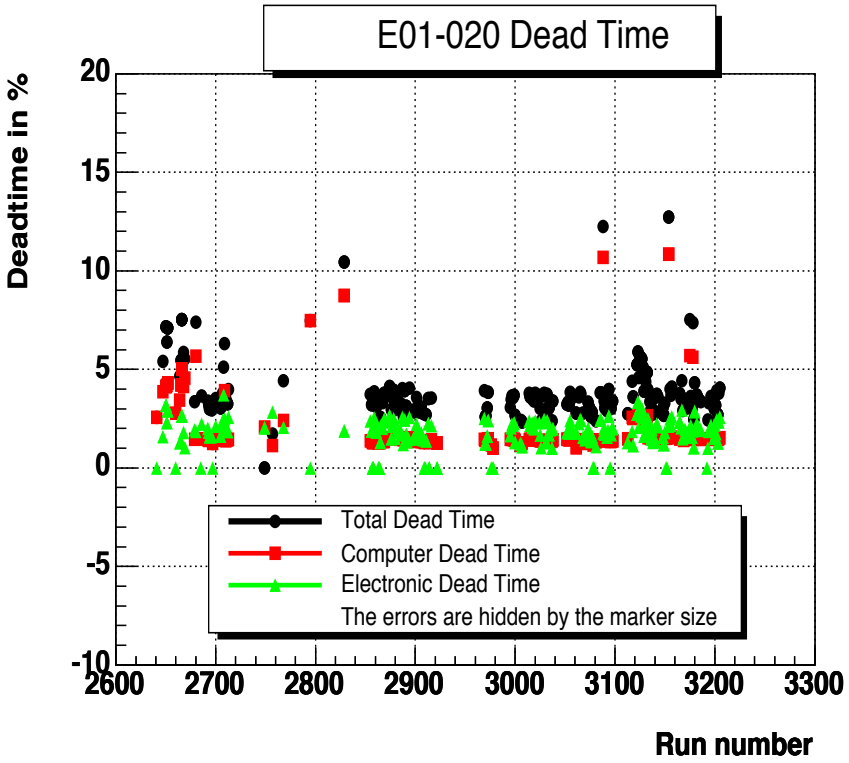

Figure 28: Deadtime vs run number.

this reason, the EDT was considered negligible. The deadtime correction factor of the acquisition system is the ratio of the number of events measured by the scaler associated to trigger T5 to the total number of coincidence events found in each run. To determine the electronic deadtime, we started running without the memory

lookup unit [44]. The trigger was formed by an overlap (logical AND) of the two scintillator planes S1 and S2. In this way the electronic deadtime was reduced. A fortran code, developed by Bodo Reitz [44], to calculate the electronic deadtime was also used in previous experiments. The code is based on the ratio of triggers to accepted triggers measured using the scalers from the TDCs and from the calibrating pulsers.

The deadtime for coincidence events is given by the following expresion: DT_{Coinc} = 1 - LT_{Coinc}, where the livetime for coincidence events is given by LT_{Coinc}= $CLT \cdot ELT_L \cdot ELT_R$. CLT is the computer live time, CDT is the computer dead time, EDT_L and EDT_R are the electronic deadtimes in the electron and hadron arm respectively The expresion for the live times are CLT = 1- CDT, ELT_L = 1-EDT_L and ELT_R = 1-EDT_R, respectively (ELT_L and ELT_R are the electronic live times). Then, the coincidence dead time is given by:

$$DT_{Coinc} = 1 - (1 - CDT) \cdot (1 - EDT_L) \cdot (1 - EDT_R) \tag{28}$$

4.9 Calibration procedure

4.9.1 Spectrometer Mispointing

By design, the spectrometers are not constrained to remain along a radius as they move around the hall central bearing. Various factors like the arc- length, direction and speed of the move change the spectrometers pointing by as much as 74 mm in a non-reproducible manner [37]. This section presents the method used for determining the mispointing of the Hall A High Resolution Spectrometers. The spectrometers had to be moved to meet each of the kinematics requirements for the angle of the scattered electron and the angle of the knockout proton. Thus, consequently the spectrometer mispointing needed to be determined for each kinematic setting. The method uses single arm data taken with carbon targets, either single foil or 9 foils targets, and the target position survey data.

From the analysis of these data one can determine the offset between the centers of the Hall Coordinate System (HCS) and the Target Coordinate System (TCS). The mis-pointing is approximated by a parallel displacement of the spectrometer axis, represented by an offset vector $\vec{r}_{sp}$. The magnitude of the offset vector $\vec{r}_{sp}$ is D. Its components in HCS are x_{sp} and z_{sp}.

A full description of HCS and TCS cartesian systems can be found in reference [45]. For convenience a short overview is presented here: The Hall Coordinate System has its origin at the defined center of the hall. The center of the hall is defined by the intersection of the electron beam and the vertical symmetry axis of the target

system. The z axis is along the beam line and points in the direction of the beam dump. The y axis is vertically up.

A Target Coordinate System is defined for each spectrometer. The z_{tg} axis is a line perpendicular to the sieve slit surface of the spectrometer which is going through the mid point of the central sieve slit hole and points away from the target. The center of the TCS it is defined to be at a fixed distance from the central sieve slit hole. This distance called Z_0 given in reference [46] is 1.181 m for electron (left) arm and 1.178 m for the hadron (right) arm. The origin of the TCS is defined to be the point on the z_{tg} axis at the distance Z_0 from the sieve surface. The x_{tg} axis is parallel to the sieve slit surface pointing vertically down. In the ideal case the origin of the TCS coincides with the hall center. The out of plane (Θ_{tg}) and the in-plane angle (Φ_{tg}) are given by $\frac{x_{tg}}{Z_0}$ and $\frac{y_{tg}}{Z_0}$ respectively (see Fig. 29).

4.9.2 Calculation of Spectrometer Pointing Offsets

The reconstructed target variables y_{tg}, ϕ_{tg}, the spectrometer angle θ (entered as a positive value for left arm and negative values for right arm) and the beam position ($Beam\_x$) are used to calculate the spectrometer offset. Initially one uses a header file in which the spectrometer offsets for both right ($specr\_offset$) and left ($specl\_offset$) arms are set to zero.

The vertex (or reaction point) is defined as the intersection of the incoming electron trajectory (beam) and the scattered particle (electron or hadron) trajectory (see Fig. 29).

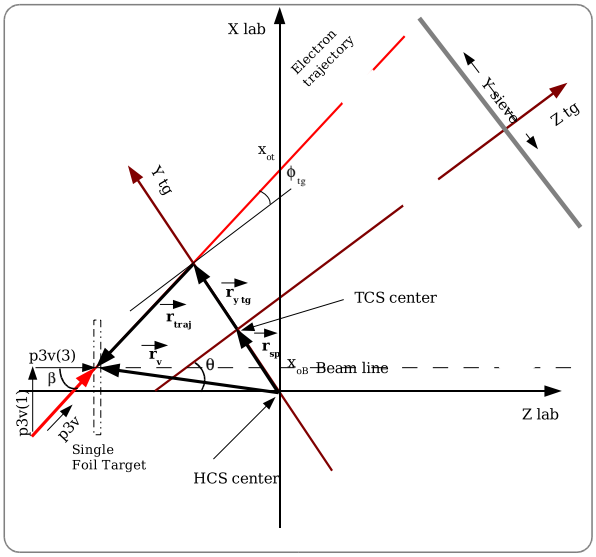

Figure 29: Hall A coordinates and target coordinates for electrons scattering from a thin foil target. Distances not to scale. θ is the spectrometer central angle. Note that the x_{tg} axis is vertically down and the y axis in the HCS (or Lab) is vertically up (out of the page).

The incoming electron trajectory in HCS is given by:

$$x_{Beam}(z) = x_{0B} + \tan(\theta_B) \cdot z \tag{29}$$

where x_{0B} is the point where the beam intersects the x axis in HCS and θ_B is the angle that the beam makes with the z axis in HCS. The scattered particle trajectory in HCS is given by:

$$x_{traj}(z) = x_{0t} + \tan(\beta) \cdot z \tag{30}$$

where x_{0t} is the point where the scattered particle (electron or hadron) intersects the x axis in HCS, and β is the angle that the particle trajectory makes with the z axis in HCS . The vertex is now given by:

$$x_{traj}(z) = x_{beam}(z). \tag{31}$$

In equation 31, the z-coordinate of the vertex is calculated as a function of y_{tg}, ϕ_{tg}, x_{sp}, z_{sp} and β where :

$$x_{sp} = D \cdot cos(\theta) \tag{32}$$

$$z_{sp} = -D \cdot sin(\theta) \tag{33}$$

$D = |r_{sp}|$ is the spectrometer parallel offset, θ is the spectrometer angle as obtained from video camera and encoder.

$$tan\beta = \frac{p_x}{p_z} \tag{34}$$

where p_x and p_z are momentum vector $\vec{p}$ components of the scattered particle in HCS ($\vec{p}3v$ in Fig. 29).

4.9.3 Spectrometer's parallel offset calculation

The vector diagram in Fig.1 allows the calculation of the spectrometer offsets using the vector equation:

$$\vec{r}_{sp} + \vec{r}_{y_{tg}} + \alpha \cdot \vec{r}_{traj} = \vec{r}_{vertex} \tag{35}$$

All vectors are given in HCS. The x and z components of the vectors in equation 35 are given below: $\vec{r}_{y_{tg}} = \begin{pmatrix} -y_{tg} \cdot sin(\theta) \\ -y_{tg} \cdot cos(\theta) \end{pmatrix}$ and $\vec{r}_{vertex} = \begin{pmatrix} -z_{tg} \\ x_{tg} \end{pmatrix}$

$\vec{r}_{sp} = \begin{pmatrix} z_{sp} \\ x_{sp} \end{pmatrix} = \begin{pmatrix} -D \cdot sin(\theta) \\ D \cdot cos(\theta) \end{pmatrix}$

$$\vec{r}_{traj} = \begin{pmatrix} cos(\theta + \phi_{tg}) \\ \\ sin(\theta + \phi_{tg}) \end{pmatrix} \text{ (unit vector)}$$

Where:

$\beta = \theta + \phi_{tg}$ (the angle that the scattered electron trajectory makes with the z axis in HCS) and α is a parameter (the distance between the vertex and the intersection of the scattered particle trajectory with the y_{tg} axis of TCS).

From the system of equations we determine α and D. The expression for D is as follows:

$$D = -ytg + \frac{Beam\_x \cdot cos(\beta) - z_{tg} \cdot sin(\beta)}{cos(\phi_{tg})} \tag{36}$$

where z_{tg} is the target position as given in the survey. The components of the offset vector can now be found using Eqs. 32 and 33.

A standalone code calculates x_{sp} and z_{sp} components of the spectrometer offset vector in the HCS using eqs. 36, 32 and 33. These calculated offsets are subsequently entered in the header file in the $specl\_offset$ (for left or electron arm) and $specr\_offset$ (for the right or hadron arm) rows. ESPACE is run again using these modified header files. The reconstructed reaction point ($react\_z$) should now agree with the target position z_tg in HCS as determined from the survey.

Results are sensitive to cuts and one should apply the same cuts for determining offsets and checking them. We applied the following cuts:

$$\mid \phi_{tg} \mid < 0.03\ rad,\ \mid \theta_{tg} \mid < 0.03\ rad,\ \mid y_{tg} \mid < 0.01\ m.$$

where: ϕ_{tg} is the horizontal angle of the particle trajectory relative to the z axis of the TCS, θ_{tg} is the vertical angle of the particle trajectory relative to the z axis of the TCS, y_{tg} is the y coordinate for an event in TCS.

4.9.4 Spectrometer's mispointing results

Fig.30 shows a typical $react\_z$ spectrum for a 9 foil carbon target. The corrected

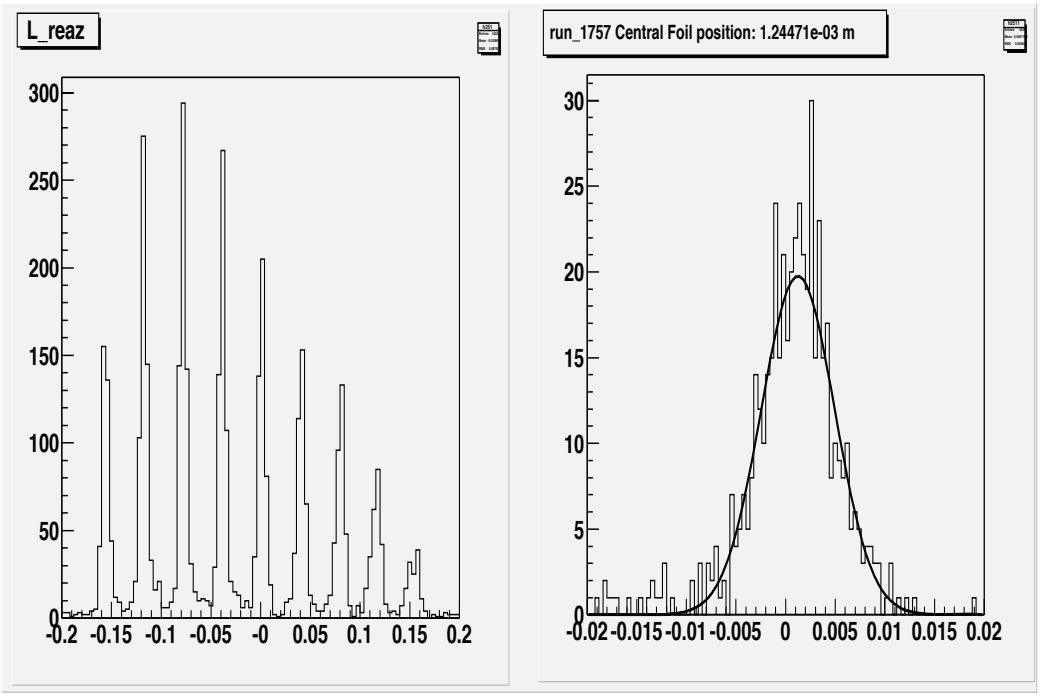

Figure 30: The 9 foil Carbon target as seen by left arm. The right panel shows the central foil position after mis-pointing correction. Data from run number 1757.

reconstructed values for the reaction point (mean of $react\_z$ distribution) for the left arm and the right arm offsets are presented in Table 4. The out-of-plane offset y_{sp} is set to zero.

Kin Q3	L_angle (^{0})	R_angle (^{0})	^{12}C run	x_off_L (m)	z_off_L (m)	x_off_R (m)	z_off_R (m)
d20	29.20	30.61	2675	4.44e-03	-2.51e-03	8.37e-04	6.24e-04
d40	29.20	35.01	2689	4.02e-03	-2.23e-03	-1.91e-03	-2.74e-03
d50	29.20	37.06	2716	4.43e-03	-2.46e-03	-1.72e-03	-2.47e-03
e20	29.20	33.80	2739	4.28e-03	-2.30e-03	4.27e-04	5.77e-04
e40	28.26	38.07	2747	4.47e-03	-2.40e-03	-1.81e-03	-2.41e-03
f20l	27.29	28.71	2801	4.30e-03	-2.16e-03	7.93e-04	1.44e-03
f40l	27.29	24.42	2872	4.10e-03	-2.08e-03	6.46e-04	1.42e-03
f50	27.29	43.77	2928	4.21e-03	-2.20e-03	-2.78e-03	-2.96e-03
g20	26.15	41.39	2961	3.79e-03	-1.87e-03	-7.32e-04	-8.16e-04
g40	26.15	46.26	3022	4.07e-03	-1.94e-03	-2.81e-03	-2.70e-03
g50	26.15	48.53	3023	3.84e-03	-1.90e-03	-2.92e-03	-2.59e-03
h20	25.59	40.96	3057	3.62e-03	-1.83e-03	2.13e-06	2.82e-05
i40	25.37	48.99	3110	3.45e-03	-1.66e-03	-2.80e-03	-2.47e-03
j40	24.83	48.69	3150	3.18e-03	-1.47e-03	-2.63e-03	-3.43e-03
j50	24.83	52.56	3161	3.89e-03	-1.71e-03	-3.37e-03	-2.60e-03

Table 4: The corrected values for the reaction point as reconstructed by ESPACE for the electron arm and the proton arm. When these offsets are used in the header files, the target position is correctly reconstructed. Optics target position was determined by survey report #A805 to be 1.2 mm upstream.

Same procedure was used for the right arm (spectrometer angle has to be included with a negative sign).

4.10 Boiling studies

Beam-induced density variations ('boiling') were studied in the Hall A cryotarget. The target used during the experiment was a cigar tube shaped cell filled with liquid deuterium (LD_2) for data production, and with liquid hydrogen (LH_2) for calibration purposes. The dependence of the LD_2 and LH_2 target density on the beam current and beam spot size, for a fixed kinematic, is presented here. While taking data the

beam was rastered over a nominally 2 mm × 2 mm square spot. A similar study was carried for the 4 mm × 4 mm raster size. The raster size refers to the spot at the target location. The data were taken at a fixed target fan speed of 60 Hz.

The physics of the target density changes in high power cryotargets is complex, as the flow is expected to be highly turbulent. As expected, we found that the density varies along the length of the target cell [47]. Runs 2641 - 2652 had a raster size of 4 mm × 4 mm and 2660 to 2669 had a raster size of 2 mm × 2 mm. The beam current ranged from 10 μA up to 90 μA. The data were analyzed with ESPACE [45] with no cuts at this level. Vertical Drift Chamber (VDC) variables were used to select valid, good events. In our experiment the electrons were detected with the left spectrometer and the singles events were recorded in triggers "T3". The proton spectrometer was the right arm (triggers "T1"). The events coincident in the two spectrometers were recorded into "T5" triggers.

4.10.1 Cuts Applied

Singles/coincidence events were selected by selecting T1, T3/T5 trigger type events.

VDC cuts were applied such that only events with three ore more hits in each wire plane and one track were selected. The endcaps of the cigar tube cell target were removed by applying a cut on the reconstructed target position along the beam direction, $|z| < 0.06$ m.

4.10.2 Boiling results

It was found out that the target density depends on the z position and the beam current. For each run, the reconstructed target position along the beam direction spectra (*react_z* spectra) was corrected for charge and computer dead time. The corrected value was divided by the average of the corrected yields for the lowest beam currents (I $\leq$ 40 μA). This procedure helps to minimize the statistical variations.

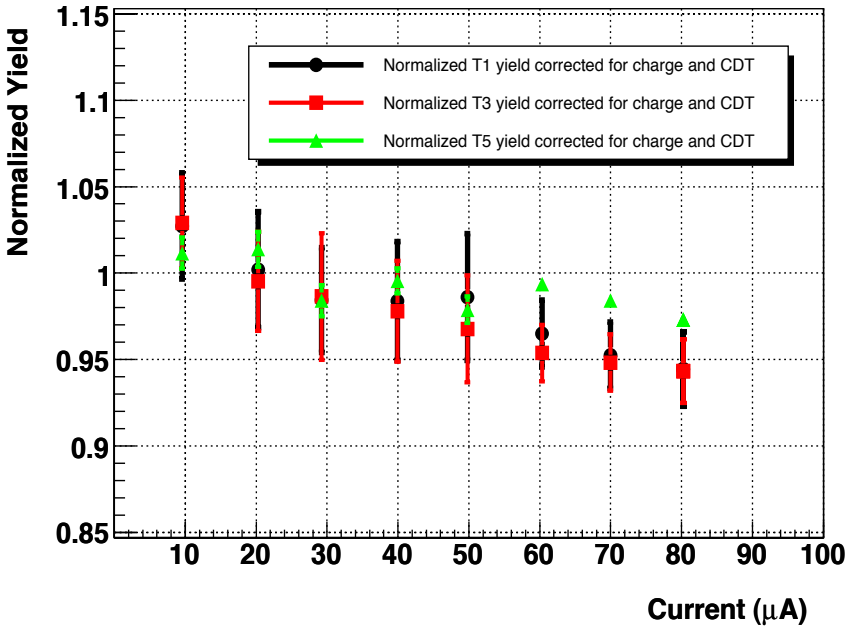

Figure 31: The normalized yields (normalized to the average corrected yields obtained for the lowest beam current), corrected for beam charge and computer dead time as a function of beam current, for each trigger type. The raster size is 2 mm $\times$ 2 mm.

The dependence of target density on the location along the beam, z, was examined in detail. In software the target was sliced in five pieces using cuts on the *React_z*

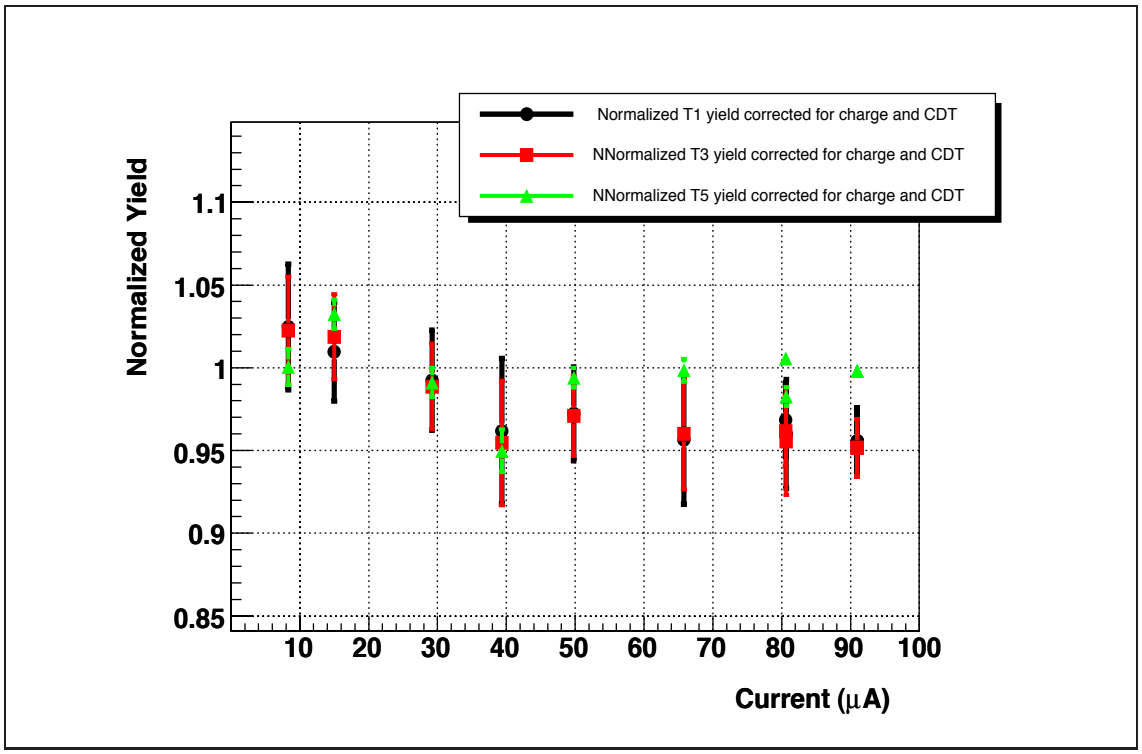

Figure 32: The normalized yields (normalized to the average corrected yields obtained for the lowest beam current), corrected for beam charge and computer dead time, for each trigger type as a function of beam current. Raster size is 4 mm $\times$ 4 mm.

variable. For each slice, the target density as a function of the depth z in the target and the beam current was examined. This combined dependence was studied for trigger types T1, T3 and T5's. From the linear fits to the slopes, shown in the Figs. 33, 34, and 35, it can be seen that there is little target density variation at the entrance of the target cell as a function of the beam current. For beam currents larger than 40 μA we can parametrize the density of the liquid D_2 target as:

$$\rho(z, I) = \rho_0 \cdot (1 + \alpha \cdot (z - z_0) \cdot (I - I_0)) \tag{37}$$

and as a constant ρ_0 for currents below 40 μA, where z is given in m, $z_0 = 0.05$ m, I is the beam current in μA, and $I_0 = 40\mu$A. The average value of α over the three trigger type's is (-0.0173 $\pm$ 0.0047).

React_z Slice (m)	T1 Slopes(μ A^{-1})	T3 Slopes(μ A^{-1})	T5 Slopes(μ A^{-1})
-0.05 , -0.03	-5.55e-04 $\pm$ 1.54e-04	-7.74e-04 $\pm$ 1.59e-04	0.35e-04 $\pm$ 0.43e-04
-0.03 , -0.01	-6.96e-04 $\pm$ 1.67e-04	-1.02e-03 $\pm$ 1.51e-04	-6.44e-04 $\pm$ 0.46e-04
-0.01 , 0.01	-8.44e-04 $\pm$ 1.73e-04	-8.27e-04 $\pm$ 1.52e-04	-1.05e-03 $\pm$ 0.33e-04
0.01 , 0.03	-1.30e-03 $\pm$ 1.69e-04	-1.14e-03 $\pm$ 1.41e-04	-8.74e-04 $\pm$ 0.52e-04
0.03 , 0.05	-1.96e-03 $\pm$ 1.59e-04	-1.95e-03 $\pm$ 1.30e-04	-1.69e-03 $\pm$ 0.43e-04

Table 5: The normalized yields (normalized to the average corrected yields obtained for the lowest beam current), corrected for beam charge and computer dead time, for each trigger type as a function of beam current and for each React_z slice. Raster Size 2 mm $\times$ 2 mm.

Results for the three trigger types (singles left-T3, singles right-T1 and coincidences-T5's) are consistent to one another within the error bars. The density reduction for currents below 40 μA is less significant and can be assumed to be constant. For LH_2, the target density fluctuations are roughly a factor of two larger at the same beam current and raster size, compared to deuterium [49]. Results are consistent with trends from previous experiments[47]. For beam currents above 40 μA, the liquid deuterium target in the cigar tube shaped target cell exhibits significant density variation, both with the beam current and the position along the beam. The density variation is more significant for the 2 mm $\times$ 2 mm raster beam size, when comparing to the 4 mm $\times$ 4 mm raster beam, as expected. The results for the data taken with a 4 mm $\times$ 4 mm raster indicate less density variation both with current and target depth z.

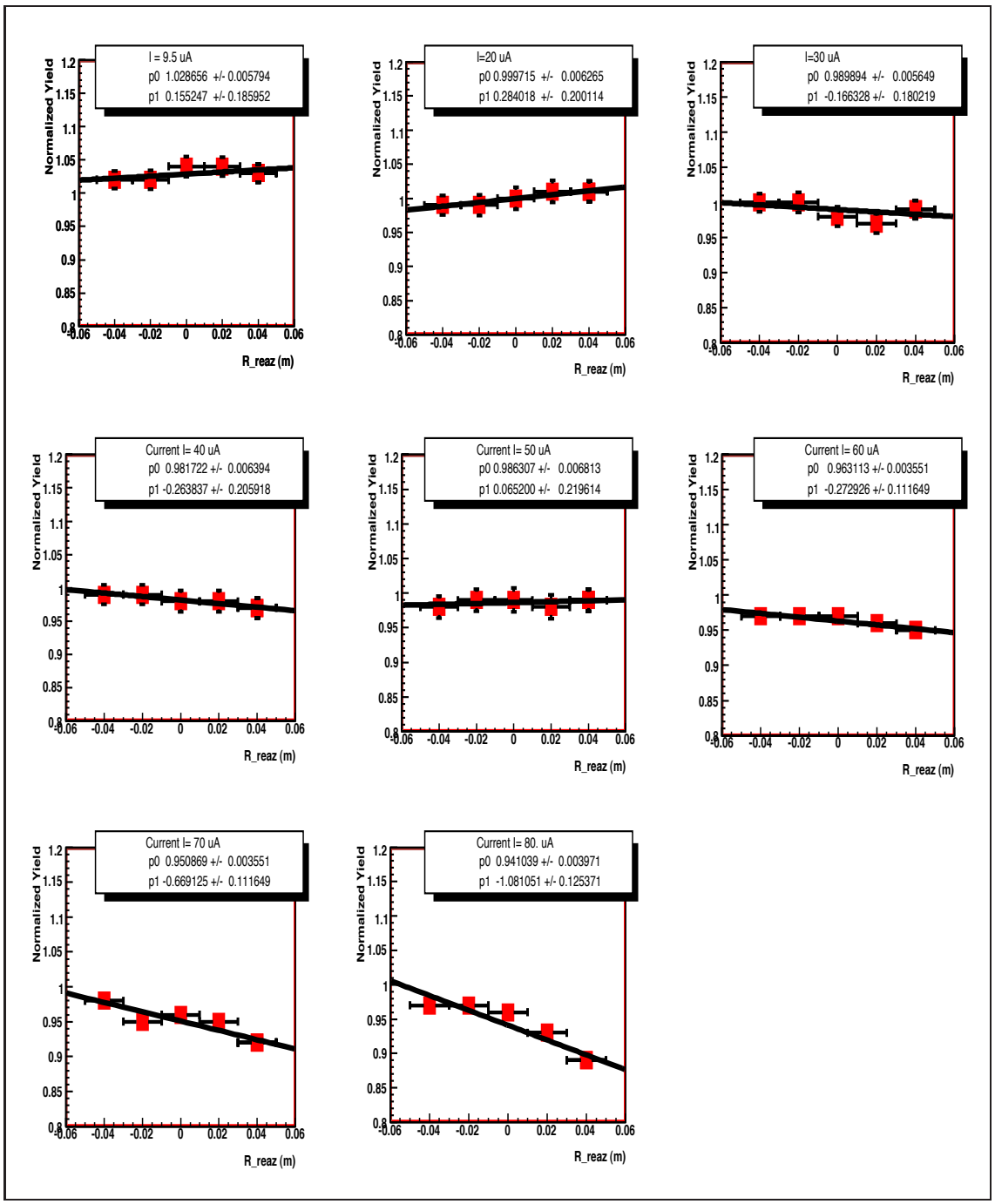

Figure 33: The normalized React_z spectra for T1 triggers for each of the eight runs used in the analysis. Each spectrum has been divided, channel by channel, by the average of the low current (I≤40 μA) runs. The current increases monotonically reading left to right and down the page. The raster size is 2 mm × 2 mm.

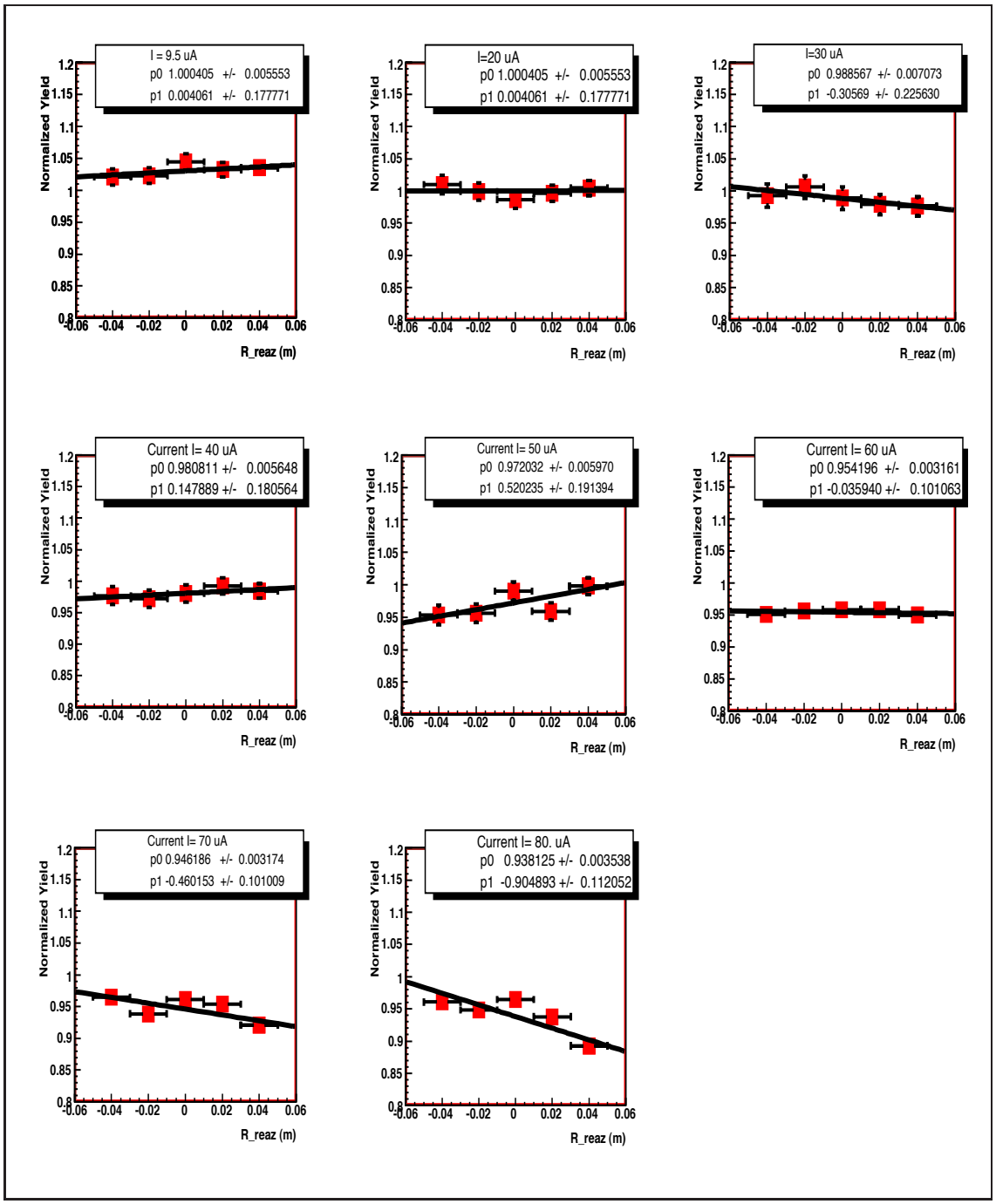

Figure 34: The normalized React_z spectra for T3 triggers for each of the eight runs used in the analysis. Each spectrum has been divided, channel by channel, by the average of the low current (I$\leq$40 μA) runs. The current increases monotonically reading left to right and down the page. The raster size is 2 mm $\times$ 2 mm.

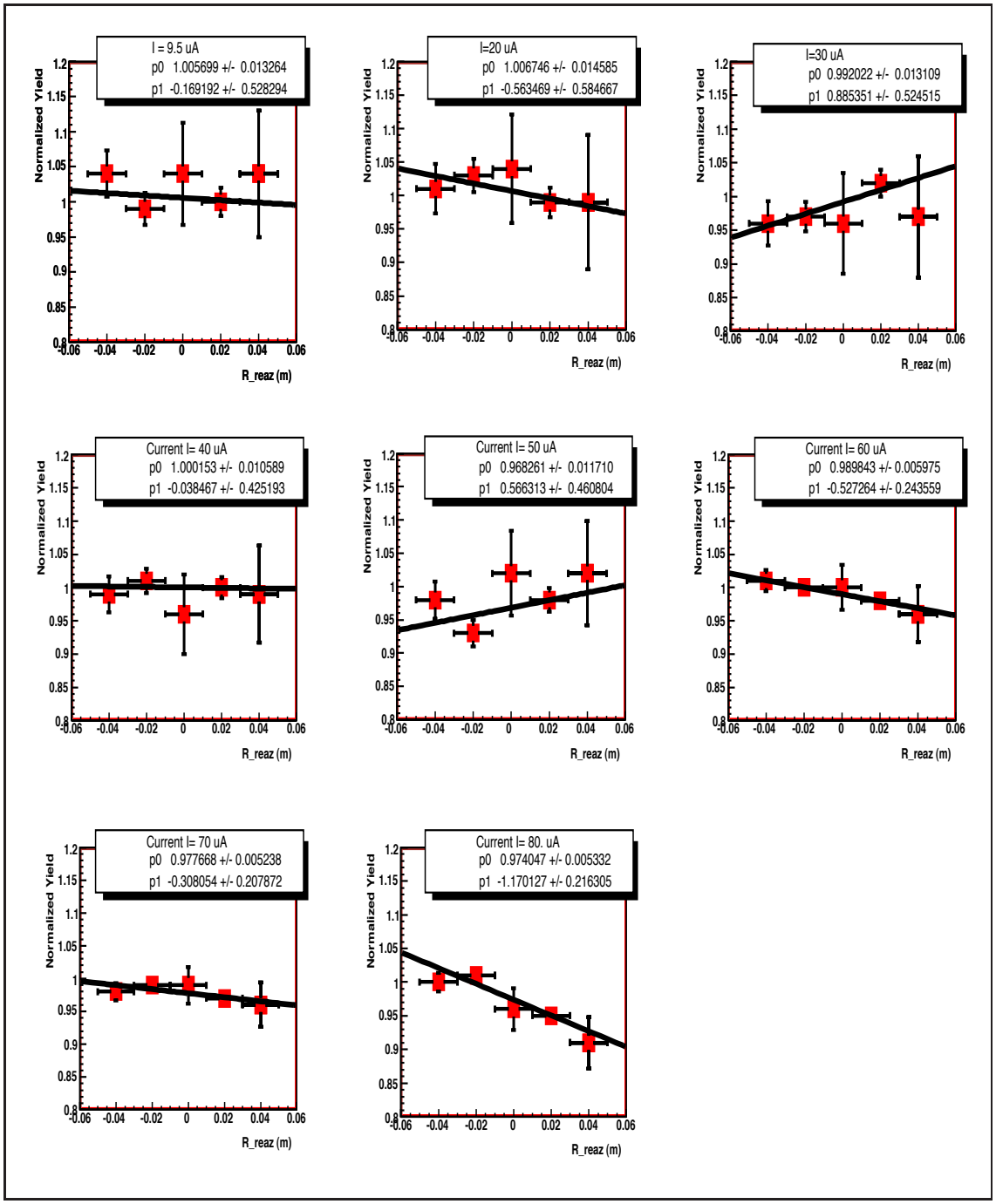

Figure 35: The normalized React_z spectra for T5 triggers for each of the eight runs used in the analysis. Each spectrum has been divided, channel by channel, by the average of the low current (I$\leq$40 μA) runs. The current increases monotonically reading left to right and down the page. The raster size is 2 mm $\times$ 2 mm.

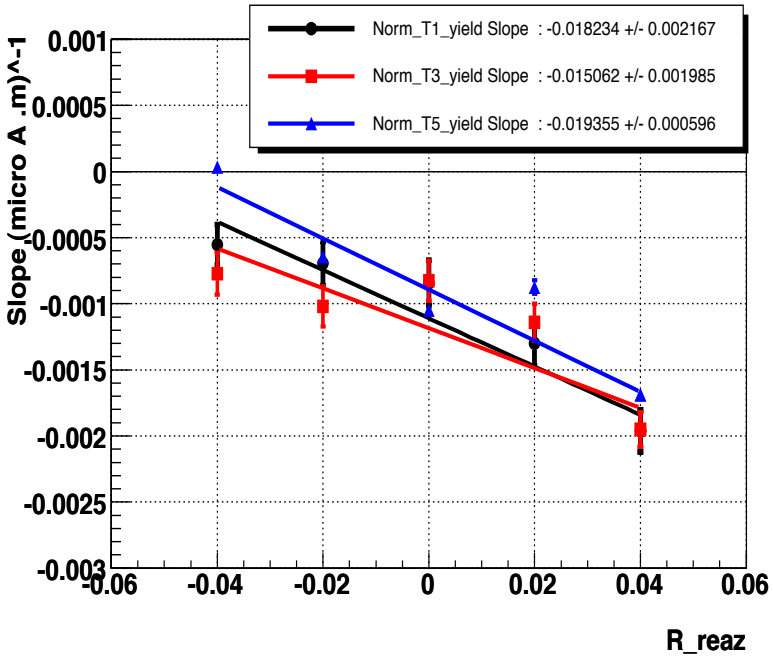

Figure 36: Slopes with respect to beam current of the React_z slopes for the normalized T1, T3 and T5 trigger rates vs. React_z. Raster size 2 mm × 2 mm. The React_z slices were 2 cm each.

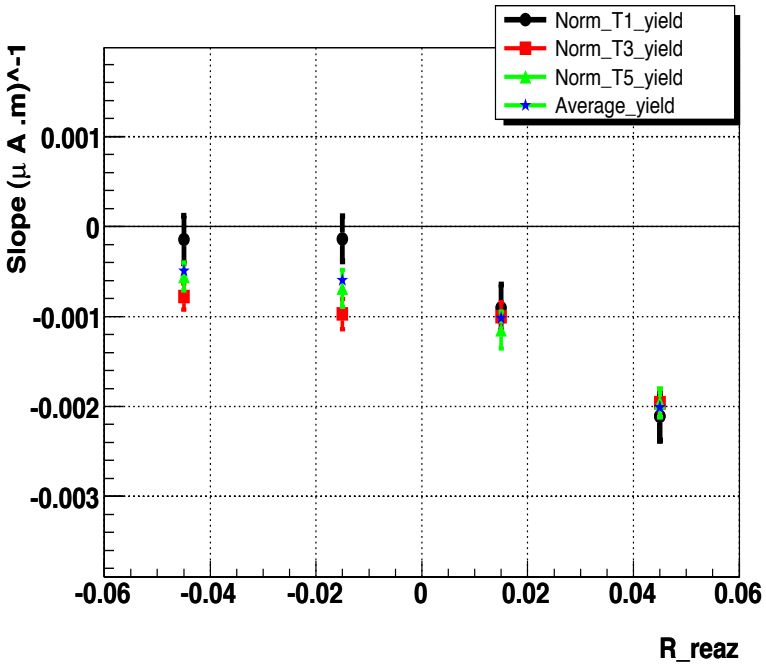

Figure 37: Slopes with respect to beam current of the React_z slopes for the normalized T1, T3 and T5 trigger rates vs. React_z. Raster size 2 mm × 2 mm. The React_z slices were 3 cm each.

4.11 Vertical drift chambers' efficiencies

In a study by Paul Ulmer [50] it is shown that large backgrounds are seen in the VDC. A large fraction of events had zero VDC hits, and many events also had multiple clusters in the VDCs. By reconstructing the tracks for multiple cluster events it was shown that particles outside the acceptance can scatter into the acceptance from pole-faces, apertures, exit window frame, within the spectrometer and from the exit window frame. The fraction of these kind of events depends on the kinematics settings. For kinematics on the tail of the quasielastic peak, these rescattered particles represented a significant fraction of the overall single-arm trigger

4.11.1 Tracking Efficiencies

Events are lost due to detector inefficiencies that cause triggers to be missed, inefficiencies in the drift chambers or tracking algorithm rejecting events. Even if a trigger is formed, there will be some events where there is incomplete information to reconstruct a track. The main sources of these type of inefficiencies are events where too many or too few wires fire in the drift chambers.

A reasonable assumption, involving only the VDC detectors, assumes that any real particle traversing the VDCs should produce three-or-more hits in EACH of the four wire planes. A cut was applied to the multiplicity variable (number of wires that give a signal for a given event), in all for planes (u1,u2,v1,v2), in the left (electron arm), and right arm (see Vertical Drift Chamber section, 4.7.2). The cut range was

(3,20) which means only events that fired between 3 and 20 wires in each of the 4 wire planes were accepted in the analysis. We label these kind of events $Mult\_3to20$. If we require the condition "$Ntrack == 1$" we select only the events with exactly one track. The cut "$Ntrack >= 1$" selects the events with at least one track.

The tracking efficiency is defined as the ratio between the number of events for which one track is found, divided by the number of 'good' events (i.e. the number of events for which we expect to have a real track). The efficiency is given then by:

$$\epsilon_{VDC} = \frac{N_{1Track}}{N_{Mult_{3to20}}} \tag{38}$$

where N_{1Track} are the events that passed the "$Mult\_3to20$" criteria and also gave rise to exactly one track in the track reconstruction algorithm. $N_{Mult_{3to20}}$ is the number of events for which is required only the "$Mult\_3to20$" criteria to be fulfilled. The track reconstruction algorithm finds all pairs and combinations of pairs of hits and fits the track. The denominator in the tracking efficiency formula consider events with a number of 3 to 20 hits in each of the four wire planes. Events lost due to this cut are either coming from background or are due to wire chamber inefficiencies.

4.11.2 VDC efficiencies results

The above cuts were applied to the data of the $Q^2 = 3.5$ (MeV/c)^2 kinematics. In the figures 38 and 39 the total HRSE efficiency, total HRSH efficiency and the coincidence efficiency are plotted versus run number.

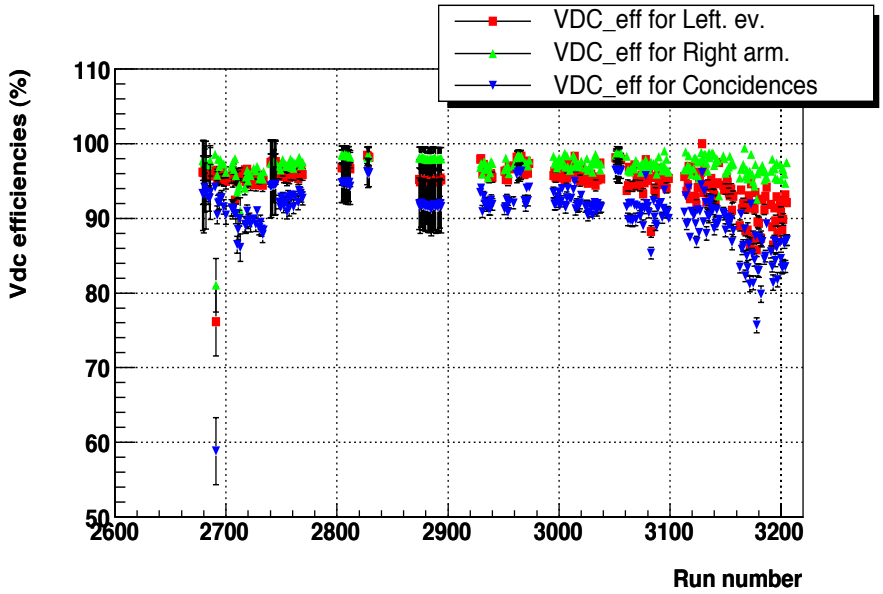

Figure 38: Vertical Drift Chamber Efficiencies (Multiplicity between 3 and 20 in each of the four wire planes).

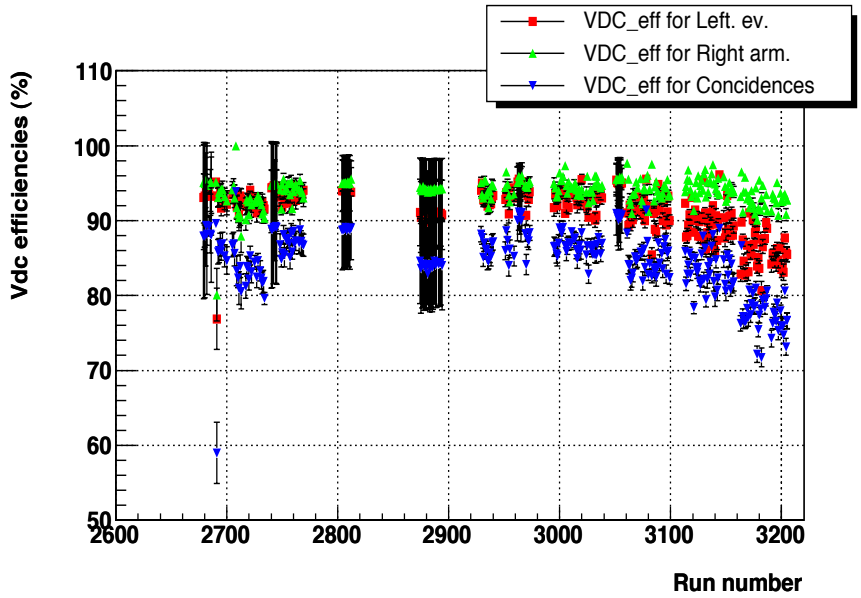

Figure 39: Vertical Drift Chamber Efficiencies (Multiplicity between 3 and 10 in each of the four wire planes).

4.12 Scintillator's efficiencies

Inefficiencies in the scintillators can cause a plane not to fire. In the right arm there is not a third scintillator paddle used to determine the efficiencies. T1 (T3) corresponds

to a good electron (proton) event. T2 (T4) triggers represent the electron events or loose R-arm (L-arm) trigger, used for measuring efficiency. Among the T2 and T4 triggers we can find events that are due to the inefficiency of the scintillators. The T1 and T3 triggers are produced when at least one paddle in the S1 and one paddle in the S2 scintillator planes fire in a verry norrow time window (coincidence). On top of this requirement the paddles which fire must satisfy the following geometrical condition: if padle i (i=1,6) fires in plane S1, either padlle i or i+1 (when i not equal to 6) or (i-1) (when i not equal to 1) fires in the S2 scintillator array. A good signal in the S1 (or S2) plane is defined as the coincidence between al least one left PMT and its corresponding right PMT of the paddle.

4.12.1 Cuts applied to determine the Scintillator's efficiencies

When calculating efficiencies, one needs to make sure that one uses a high quality sample of events in S1 when testing S2 (and in S2 to test S1). To obtain a high quality or clean events we use geomtrical cuts on the active area of the scintillators and require that the projected track crosses it. The point is that the cleaner the event sample, the better is the determination of the correction but of course at the expence of statistics. One needs to find the optimum between the quality of the event sample and the statistical error.

We clean the sample with the mean of VDC detectors. A good track cut implies good multiplicity, one cluster and exactly one track. The multiplicity is between 3 and 20 in the all the four planes. Exacly one cluster is required in all VDC planes.

Good physics events are selected by imposing cuts on the out of plane and the in-plane angles in the two spectrometers (variables denoted as Φ_{tg} and Θ_{tg}):

$$|\Phi_{tg}| \leq 0.02 \text{ rad} \quad \text{and} \quad |\Theta_{tg}| \leq 0.04 \text{ rad} . \tag{39}$$

4.12.2 Efficiency Calculation for the Electron Arm

Trigger T4 is defined as the coincidence of a sighal which comes from the S1 plane and a signal which comes from the plane S0, under the condition that plane S2 did not fire, or, the coincidence between S2 and S0 when S1 is missing. The number of T4 triggers can be calculated as follows:

$$N1_{T4} = N_0 \cdot \epsilon_1 \cdot (1 - \epsilon_2) \cdot \epsilon_3 \tag{40}$$

$$N2_{T4} = N_0 \cdot \ (1 - \epsilon_1) \cdot \epsilon_2 \cdot \epsilon_3 \tag{41}$$

where ϵ_1,ϵ_2 and ϵ_3 are the integrated efficiencies of the S1,S2 and S3 scintillator arrays respectively and N_0 is the number of incident particles on the detectors. The number of T4 triggers can be written as:

$$N_{T4} = N1_{T4} + N2_{T4}$$

The number of T3 triggers can be written as:

$$N3_{T3} = N_0 \cdot \epsilon_1 \cdot \epsilon_2 \cdot \epsilon_3 \tag{42}$$

We can extract the efficiencies of the S1 and S2 scintillator arrays by taking the ratios:

$$R_{13} = \frac{N1_{T4}}{N3_{T3}} = \frac{1-\epsilon_2}{\epsilon_2} \tag{43}$$

$$R_{23} = \frac{N2_{T4}}{N3_{T3}} = \frac{1-\epsilon_1}{\epsilon_1} \tag{44}$$

Then, ϵ_1 and ϵ_2 can be written as:

$$\epsilon_1 = \frac{1}{(1+R_{23})} \qquad\qquad \epsilon_2 = \frac{1}{(1+R_{13})} \tag{45}$$

4.12.3 Scintillator efficiencies results

The efficiencies ϵ_1 and ϵ_2 calculated using equation 45 , for all the runs in the Q3 kinematic, are shown in Fig. 40:

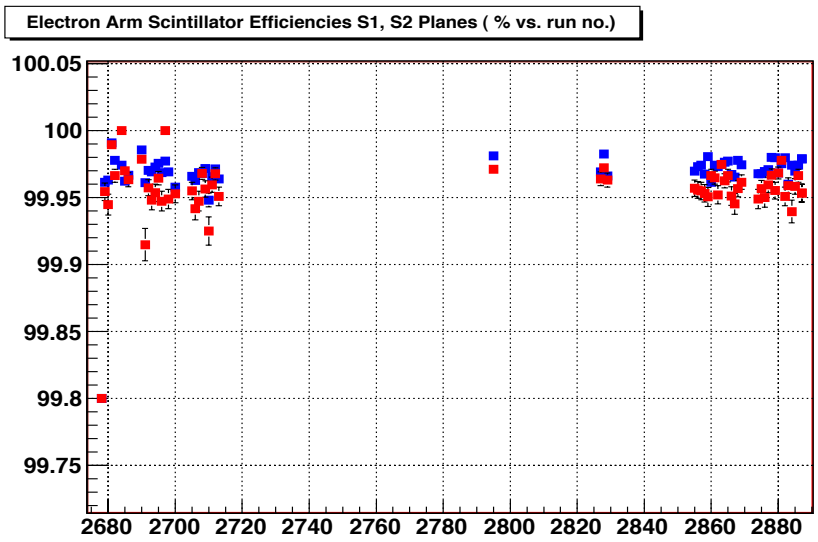

Figure 40: The integrated electron arm scintillator efficiencies for Planes S1 (blue) and S2 (red).

5 Gas Cerenkov efficiency

The electron spectrometer gas Cerenkov is described in Sec. 4.7.3. The electrons detected in the HRSE were separated from the π^- by a software cut which require that the sum of the ten ADC signals is greater than 150.

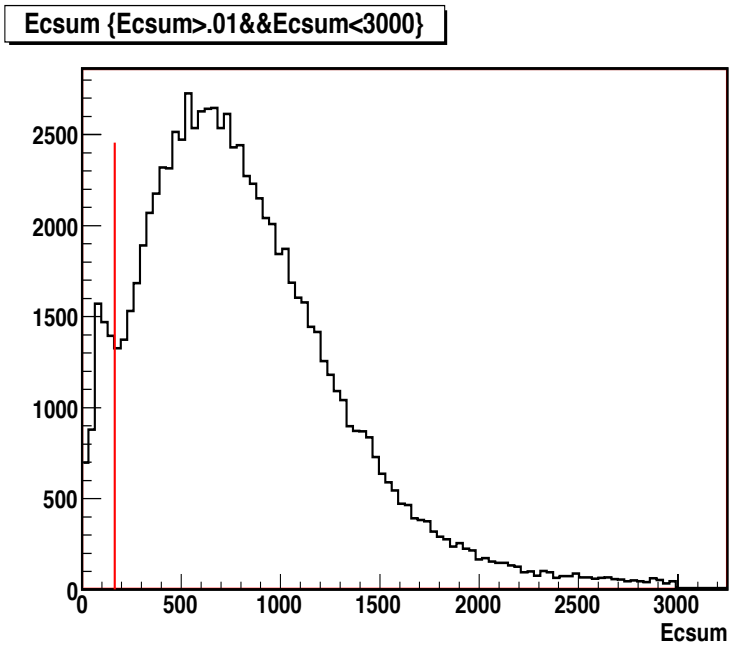

Figure 41: The distribution of the sum of the gas Cerenkov ADCs.

The gas Cerenkov inefficiency is defined as the fraction of electrons eliminated by the cut $ADC_{sum} > 150$. The inefficiency can be found by looking at the coincidence E_miss spectra for various cuts on the Cerenkon ADC_{sum} and calculating the fraction of events eliminated by the cut. A kinematic calculation shows that the π^-, truly coincident with a positively charged proton in the hadron spectrometer, are not kinematicaly allowed in the E_miss spectra of the $^2H(e,e'p)n$ reaction. Therefore, events found in the E_miss spectra when the $ADC_{sum} < 150$ cut is imposed are

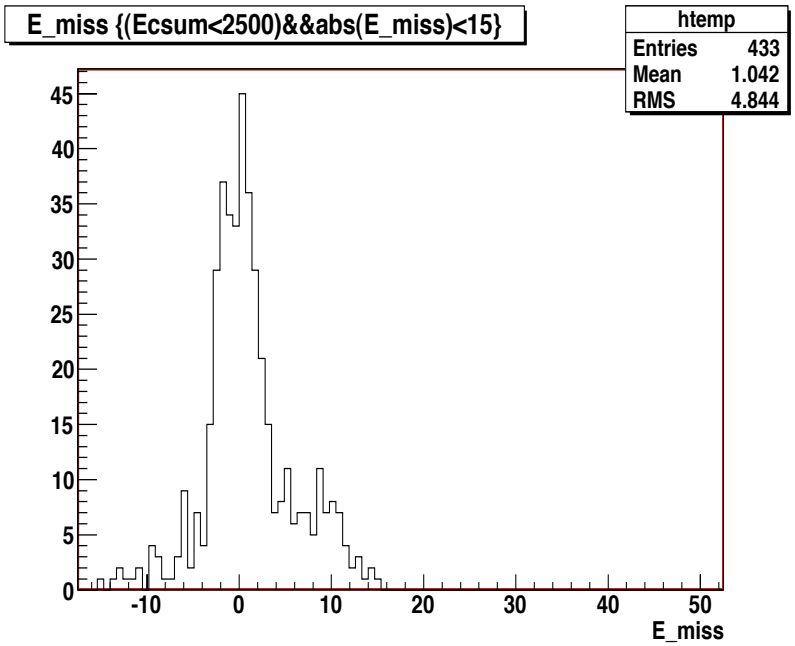

Figure 42: The distribution of the E_miss spectra when there is no cut on the sum of the gas Cerenkov ADCs. The analyzed run is 3006 in kinematics labeled $Q3D\_g40$

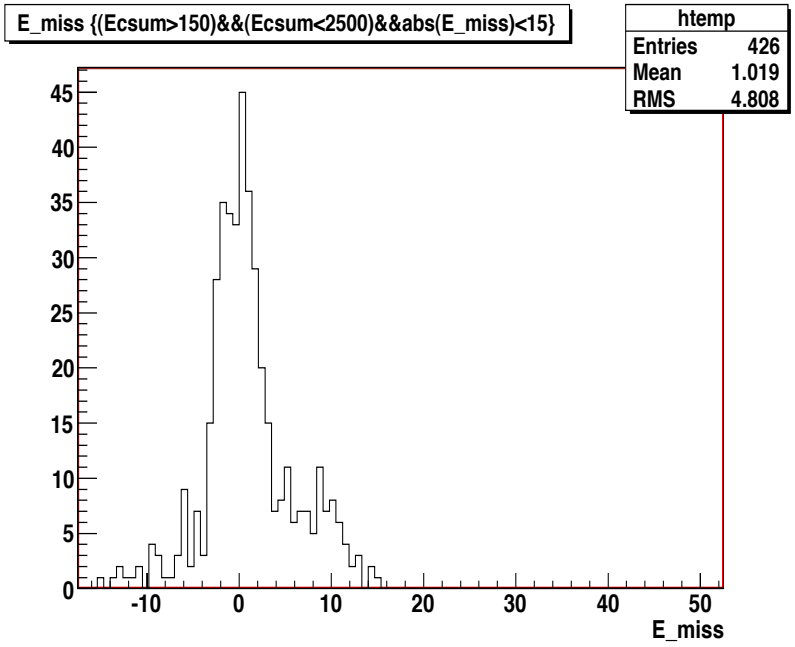

Figure 43: The distribution of the E_miss spectra when there is a cut on the sum of the gas Cerenkov ADCs. $ADC_{sum} > 150$.

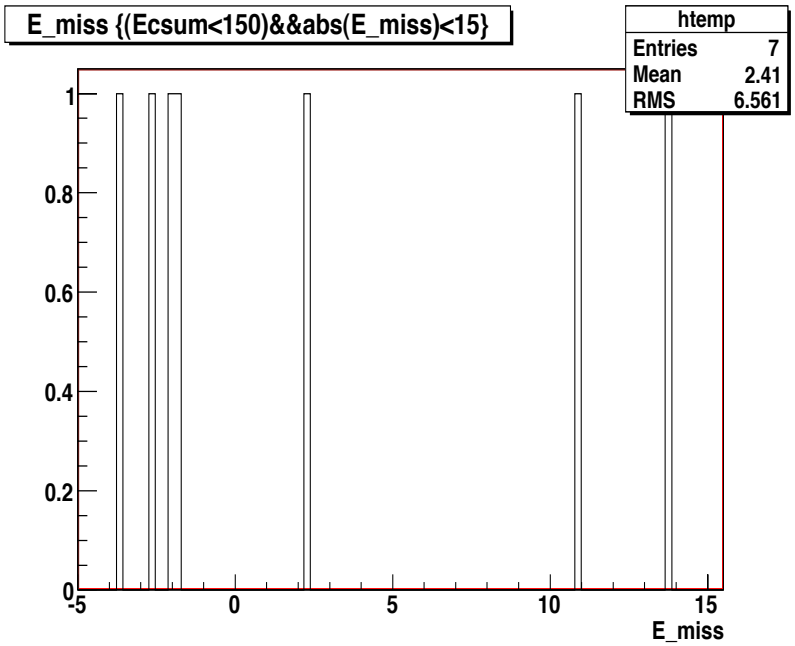

Figure 44: The distribution of the E_miss spectra when there is a cut on the sum of the gas Cerenkov ADCs. $ADC_{sum} < 150$.

electrons lost due to the Gas Cerenkov detector inefficiencies. The gas Cerenkov efficiency is found with the formula

$$\epsilon_{GC} = \frac{N_{adc\_cut}}{N_{tot}} \tag{46}$$

where N_{adc_cut} is the number of events in the spectrum after applying the cut $ADC_{sum} > 150$.

6 Scintillator timming correction

In order to detect particles which emerge from the same reaction in the target one has to determine a suitable coincidence timing window. The time between the arrival of the trigger signals in the two spectrometers is called time-of-flight (TOF). Ideally, the

TOF spectrum for particles from the same reaction should be a very narrow peak. Jitter, walk and drift are the three major factors limiting time resolution. Many systems include a non-negligible level of electronic noise, and this noise causes an uncertainty or jitter in the time at which the analog pulse crosses the discriminator threshold. "Walk" is the systematic dependence of the time marker on the amplitude of the input pulse. The higher amplitude pulse crosses the discriminator threshold earlier than the smaller pulse. With a leading-edge timing discriminator, smaller pulses produce an output from the discriminator later than larger pulses do. Drift is the long-term error introduced by component aging and by temperature variations in the discriminator circuits. In additon, the TOF spectrum is widenned by the spread in the particles momenta, path length differences for different kinematics, collection times in the scintillators and the time required by the electronics to produce the logical signal which can be used in the coincidence module. Corrections need to be applied in order to convert from the TDC value of the hit to the time of the hit. As the particle passes through the scintillator, the light has to propagate through the scintillator until it reaches the phototube. The raw time peak is additionally smeared because of the detector electronics (modules, cables and delays). All of the delays introduced between the event and the final TDC measurement must be corrected for in order to reconstruct the time of the event.

Since the optical properties of the spectrometers are well known and since the VDCs provide enough information to reconstruct the particle trajectories, the path length differences relative to the central trajectories and the corresponding 'correc-

tion' to the coincidence time can be calculated. The overall time it takes to reach the TDC is not important. What needs to be properly determined is the relative time between the scintillators. The relative delays in the scintillator cables and PMT responses of adjacent paddles can be found from the events in which a particle hits on everlaping region of paddles. The difference between the TDCs of the PMTs of adjiacent paddles yields the relative delay.

An other cathegory of events of interest for time related calibrated quantities are events in which a particle hits a pair of paddles from the two scintillator parallel planes. From the distribution of these events we find the relative delays between the paddles from a knowledge of the particle velocity and the trajectory at the focal plane. Fig.45 and 46 shows the β optimization for individual paddle before and after offsets corrections. The beta optimization was done for both spectrometers. After

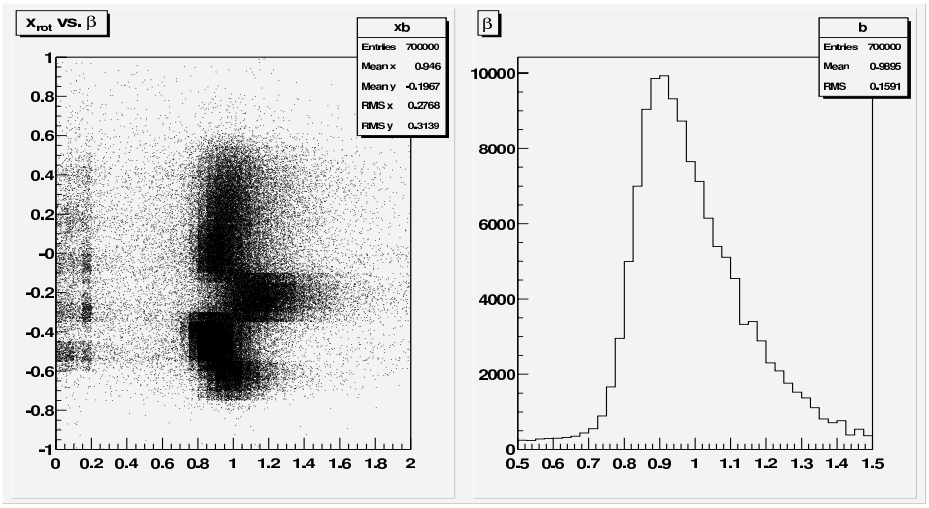

Figure 45: x_fp vs. β and β for individual paddle offsets before paddle-to-paddle time offsets optimization.

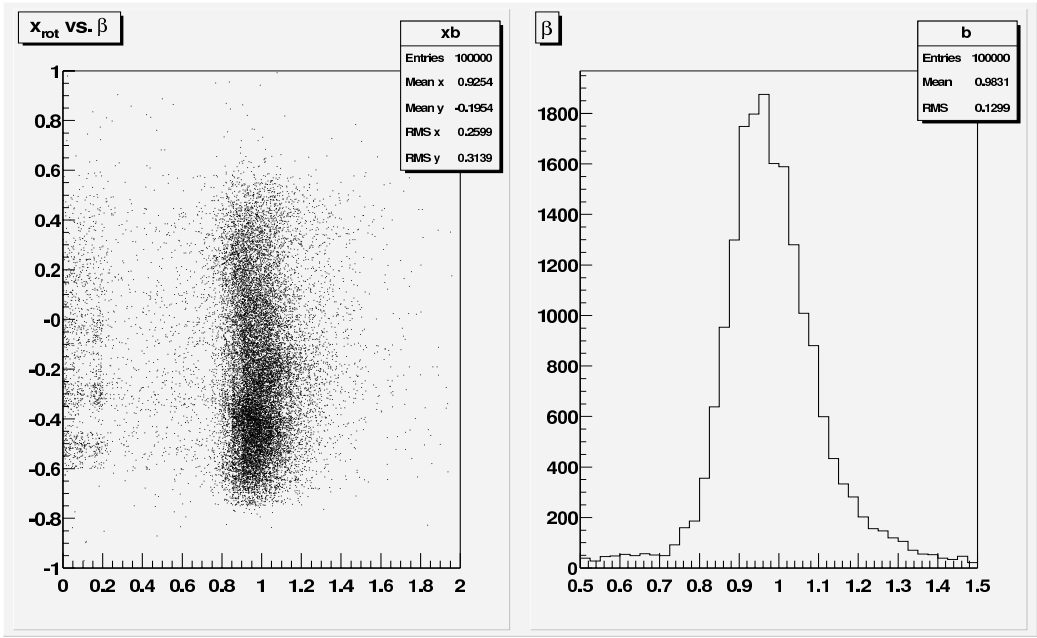

Figure 46: x_fp vs. β and β for individual paddle offsets after paddle-to-paddle time offsets optimization.

the paddle-to-paddle time offsets optimization was done for both HRSE and HRSH, the TOF for the particles was determined. Shown in Fig. 47 is a coincidence TOF spectrum from $^2H(e,e'p)n$ reaction. The typical FWHM of the spectrum was 2.3 ns (σ = 1 ns, FWHM = 2.3 σ).

7 Analysis

This section details the analysis methods used to extract final cross sections from the raw data tapes. The wire chambers were used to find the electron track and determine its momentum and scattering angle. Time-of-flight measurements between the front and rear scintillators in the hadron arm identified the knockout protons.

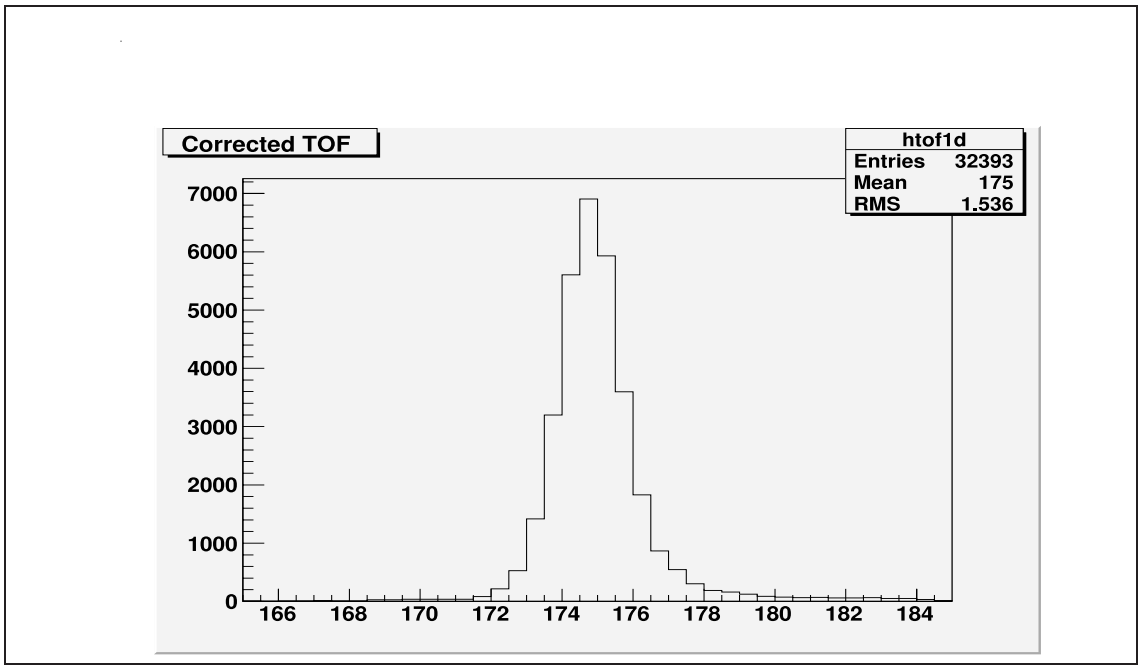

Figure 47: Corrected TOF. The coincidence time TDC spectrum for kinematics $Q3D\_d20$. One channel corresponds to 1 ns.

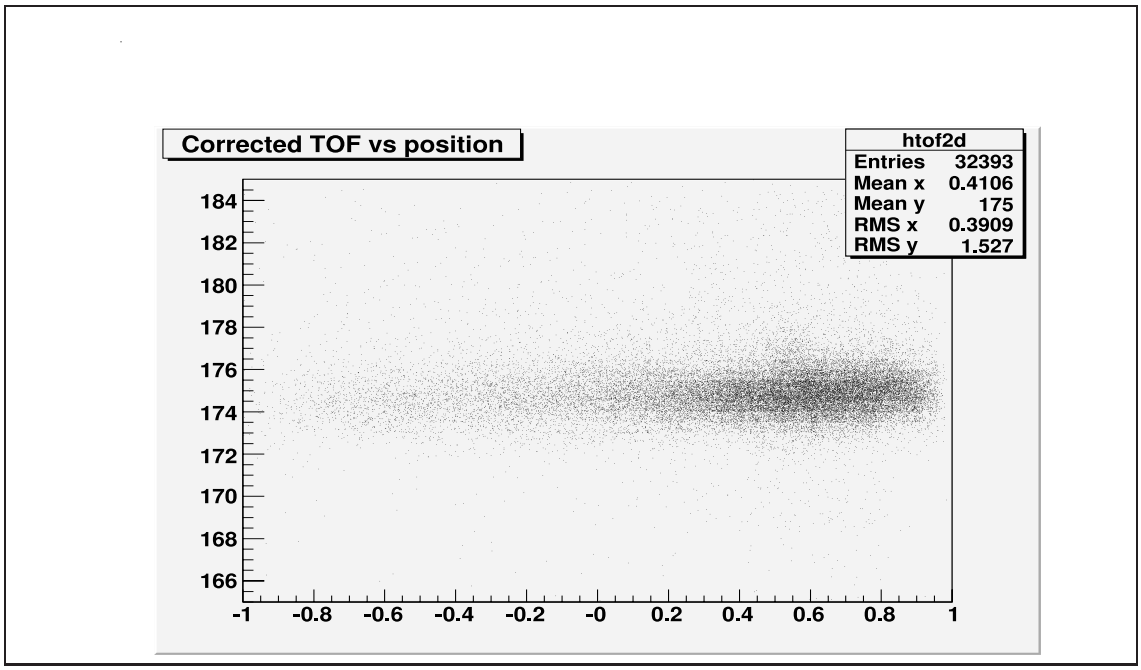

Figure 48: Corrected 2D TOF. The coincidence time TDC spectrum for kinematics $Q3D\_d20$

Time-of-flight measurements between the electron and proton arms were used to find the electron-proton coincidences. The resulting yields (missing momentum spectrum) were corrected for the experimental inefficiencies. Full MCEEP simulations including energy losses, radiative effects, multiple scattering in the target, and spectrometer resolutions were made. A set of final cuts were applied to ensure the match between data and simulation. The MCEEP generated phase space was used to extract final cross sections.

7.1 Event Reconstruction

The analysis of the raw data files was done using the standard Hall A ESPACE [45] event reconstruction software. ESPACE used a set of matrix elements for HRS to transform the position and angles of the particle measured in the wire chambers to the momentum of the detected particle and to its coordinates θ_{tg}, ϕ_{tg}, y_{tg} at the target. The coordinates (θ_{tg}, ϕ_{tg}, y_{tg}) of the particle at the target are in the spectrometer transport system, as defined in Fig. 29. By combining the reconstructed value of y_{tg} with the beam rastering information, ESPACE also reconstructs the position $react\_z$, the location of the reaction vertex, of the particle along the beam in the beam coordinate system (also defined in Fig. 29). Detector calibrations and optimizations were carried out using separate codes and the results were taken as input to the event reconstruction software. After the tracking and particle identification information is generated by the ESPACE analysis package, the physics analysis is carried out using ROOT [48], stand-alone C++, PYTHON, and shell scripts codes.

7.2 Applied Cuts

A set of cuts were applied to select coincidence events with "good track" and belonging to a stable beam period. "Good track" events were defined as events which produce one cluster in the VDCs and have multiplicity between 3 and 20 and generate at least one track in both HR spectrometers. These cuts were applied to the first analysis step using ESPACE where the two particle momentum vectors, missing mass and missing energy and the location of the reaction vertex was evaluated. The output of this analysis was stored event by event in ROOT files for further analysis. Subsequent analysis steps were carried out using ROOT. Further additional cuts are applied to the reconstructed target quantities in order to reject events that originate outside of the target but end up in the detectors after multiple scattering in the magnets or shielding. In order to identify the electron and protons coming from the same reaction we first applied a cut to the TOF (to select coincidence events). In addition, we apply a cut to the reconstructed missing energy.

- Event Type Cut

Electron-proton coincidences were selected by using a cut on the CODA event type 5. The single arm events are prescaled. The prescaling factor determine the fraction of single arm event written to tape. These events were selected by forming a logical AND between the single arm trigger and a pulse generator with an adjustable rate in the *"prescaler"*. For coincidence events (events of interest) the prescale factor was 1(PS5=1).

- Cut on stable beam period

During E01020 there were periods with a large number of beam intrerruptions (trips) during a run. In the final analysis, only the stable beam parts of each run were selected. A stable part of the beam was defined as follows: the beam current had to be larger than $5\mu A$ and the variation in the current had to be less than $5\mu A$. In addition, in order two allow the stabilization of the target density it was required that the beam was stable for 30 seconds before the start of the selected stable beam period.

- VDC Cut

Adjacent wires that fires in a chamber were treated as a single group. The number of wires in a group is called multiplicity. For a good event it was required that all multiplicities for all VDC planes in the two spectrometers must be equal or larger than 3 and to have at least one track in both spectrometer's VDCs.

- Coincidence time cut

A cut was applied to the TOF of each event, centered around the coincidence peak. The width of the cut was 5 ns (see Fig. 47). The primary means used to isolate true coincident events from the data is the coincidence time spectrum. A coincident electron should trigger a signal with a fixed time relation to the signal triggered by the corresponding proton. For uncorrelated electrons and protons the difference between the time of flight can take any value. The coincidence time spectrum of all events

exhibits a peak at a certain average value of TOF corresponding to true coincidences and a continuous background of accidental coincidences, spanning the whole width of the coincidence gate. The observed width of the background of accidental coincidences is equal to the width of the coincidence gate. In our experiment, the gate was set to T = 80 ns in order to accommodate a broad range of the proton's time of flight. At Q^2=3.5 $(GeV/c)^2$ the accidental rate was very low, almost unobservable.

- Cut on the reconstructed vertex position.

The target length extent was defined by a cut on the variable react_z, which is the position of the reaction vertex along the beam line. It was calculated from y_{tg} as measured in the HRS and the instantaneous beam position as determined from the beam rastering information calibration. The purpose of the *react_z* cut was to eliminate the contribution of the target walls to the (e,e'p) cross section (see Fig. 50). The *react_z* cut used throughout the (e,e'p) analysis was $|zreact| < 5cm$.

- Cut on the vertex position difference.

The variable *react_z* can be calculated using either the electron or the hadron arm. These calculations should give the same results for real coincidence events. The vertex z position difference between the electron arm and the proton arm was required to be less than 1.5 cm.

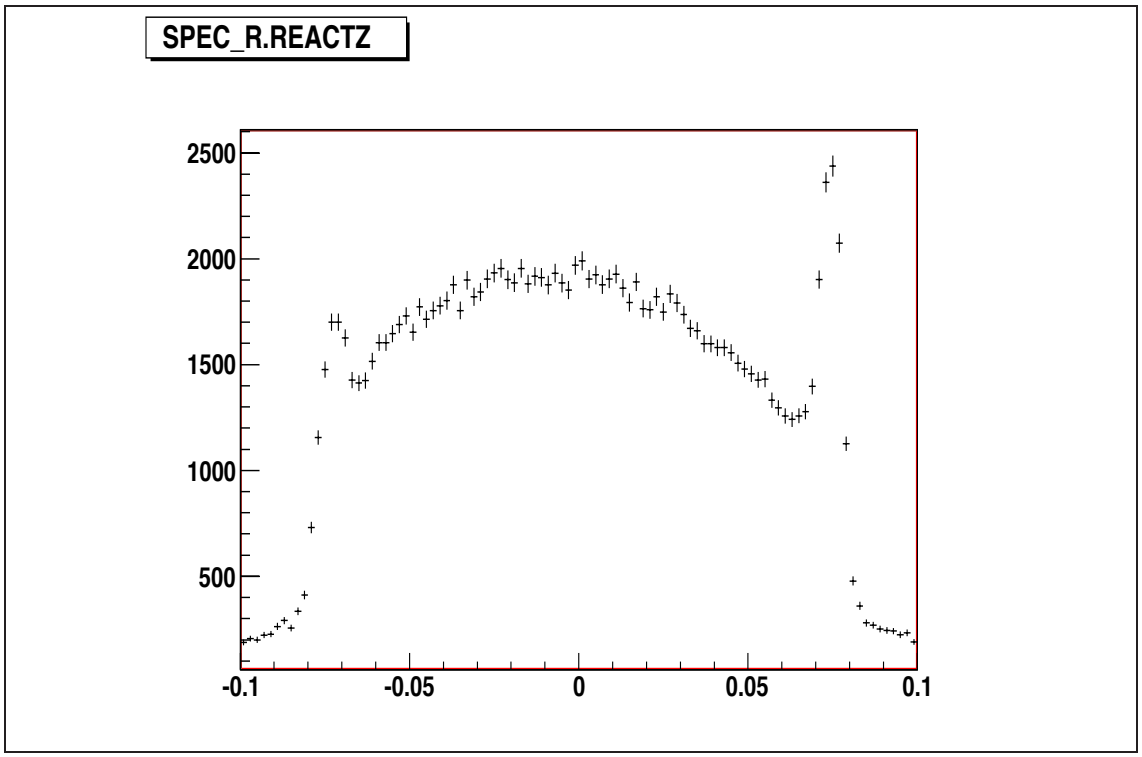

Figure 49: The *react_z* spectra showing the peaks coming from the end caps of the target. The cut used throughout the (e,e'p) analysis was $|zreact| < 0.05$ meters

- Missing energy cut

The missing energy cut is used to select events belonging to the $^2H(e, e'p)n$ reaction which produces a peak at 2.25 MeV corresponding to the binding energy of the deuteron. In our data analysis, we used an event-by-event reconstruction of the missing energy and missing momenta and the true coincidences were observed in the accumulated missing energy distribution. The incident and the outgoing electron can emit real photons as they travel through the electromagnetic field of the target nucleus. This process creates a tail in the missing energy spectrum of the (e,e'p) events.

The cut to the missing energy E_{miss} calculated from the measured four vectors of the particles involved in the reaction was: $-10 < |E_{miss}| < 15$.

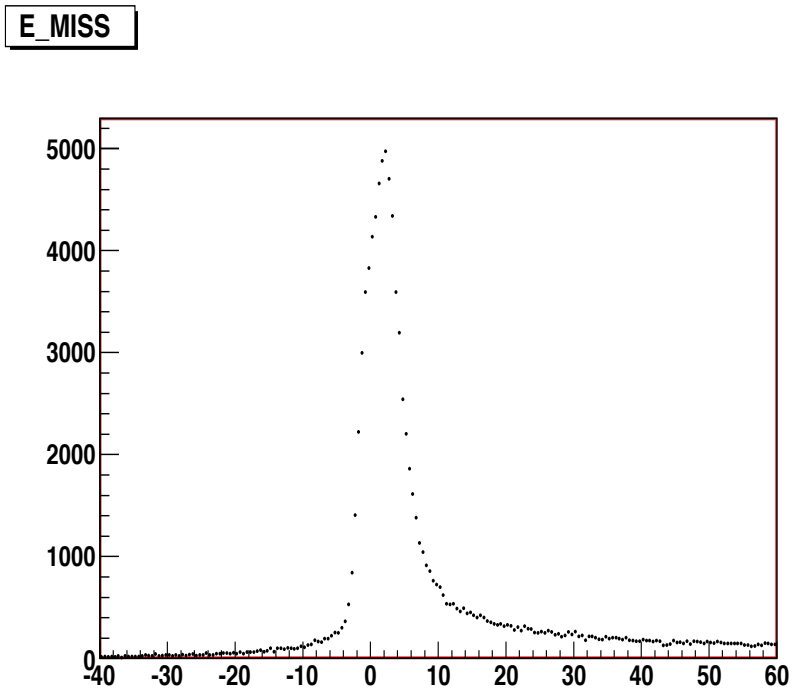

Figure 50: A typical The E_{miss} spectra for the $2^H(e,e'p)n$ reaction. The cut applied on this variable was $-10 < |E_{miss}| < 15$.

- Relative momentum cut

The dispersive coordinate δ is related to the detected momentum of the particle via $\delta = \frac{(p-p_0)}{p_0}$, where p_0 is the reference momentum which depends on the field settings of the spectrometer. The cuts on δ was chosen to be 4%.

- Cerenkov cut

A particle identification cut was applied to reject pions. Pions give a much smaller signal than the electrons in the Cerenkov detector. A cut on the sum of the Gas Cerenkov ADC channels ($ADCSUM > 150$) was applied to remove the contribution from pions.

- $R\_function$ cut

For a fixed angle and momentum setting, the HRS will accept particle trajectories in a limited range of angles and momenta, around the central values. R-function acceptance cuts were applied to limit events to those kinematical regions of the electron and hadron spectrometers where their acceptances are well known.

7.3 Monte Carlo Simulation

The $^2H(e,e'p)n$ reaction was simulated with the "Monte Carlo for $(e,e'p)$ experiments" program (MCEEP) [51]. MCEEP calculates the most probable energy losses of electrons and protons with the Bethe-Bloch formula, with additional corrections for density and shell effects. Energy loss is approximated by either Landau, Vavilov, or Gaussian distributions, depending on the ratio between the most probable energy loss and maximum energy loss in a single collision. In a final stage of event simulation, the mean energy losses of electrons and protons are subtracted to allow comparison with data corrected for the mean energy losses. To calculate the $^2H(e,e'p)n$ phase

space acceptance MCEEP was run for a bound final state (a neutron) with all resolution effects turned off.

7.4 Event generation

Mceep simulation of the (e,e'p) reaction proceeds along the following steps: first the vertex is selected (including the beam raster) and the direction of the proton. This is achieved by means of an event generator that creates sets of particles distributed uniformly in δ, θ, ϕ, x, y, and z. When the reaction point is known, the length of the path (and the corresponding energy loss) of the incoming electron through the target cell can be calculated. Second, the scattered electron is generated. One then checks whether the outgoing electron passes the collimator: if it does, the length of its path through the target cell is calculated and a corresponding energy loss is evaluated and the electron's momentum is adjusted accordingly. If the momentum of the electron still fits into the momentum acceptance of the spectrometer, one has a valid electron; in all other circumstances, the event is rejected. To be able to compare the simulated particle distributions to the ones obtained from the analysis program, the final particle momenta are corrected for energy losses energy losses in the last step of the simulation in the same manner as for the experimental reaction events. The direction of the proton is selected by selecting a location in the opening of the spectrometer. The vertex and the location in the opening of the spectrometer give the direction of the proton.

7.5 Transport through the spectrometer

MCEEP has a model which simulates a spectrometer response using three main elements: the event generator, the transport of the particle through the magnets, and the list of materials and apertures that cause multiple scattering or stop the particles. The particles generated at the target are transported to the focal plane, by application of the spectrometer forward transfer functions [51].

The most significant multiple scattering occurs in the target material and in the scattering chamber exit window. There is significant multiple scattering in the detector material itself, but the scattering that occurs before the particle passes through the magnets has a greater effect on the resolution. Gaussian distribution were used to simulate multiple scattering of the events in the target, the scattering chamber exit window and spectrometer entrance window. The final focal plane quantities obtained, are used to calculate the event variables at the target. Each target variable is expressed as a multidimensional polynomial of the focal plane variables using the same functions as for the experimental data. The spectrometer resolution is simulated by additional Gaussian distributions to particle coordinates reconstructed at the target. The parameters of these additional distributions are chosen to match the experimentally observed spectrometer resolution.

7.6 Radiative corrections

Because of their small masses, electrons can easily radiate photons in the field of the target nuclei(Bremsstrahlung radiation). The angular distribution of the emitted photons is peaked in the direction of the incident and the scattered electrons. In most calculations of corrections due to radiative effect, the assumption used is that all photons are emitted in the direction of the momentum of the radiating particles (peaking approximation). An electron can emit real photons in the field of the same nucleus in which the interaction takes place (internal bremsstrahlung) or in the field of an other nucleus (external bremsstrahlung). The electron can radiate before and/or ofter the reaction. If the electron radiates after the reaction, the kinematic at the location of the vertex is changed. The corrections due to internal bremsstrahlung and the emission and reabsorption of virtual photons has been first calculated by Schwinger [52]. External bremsstrahlung has been calculated by Bethe [53]. Large statistical fluctuations can occur in the amount of energy deposited by the particle in material. The proton loses energy by many small energy loss interactions while the electron losses a large amount of energy in a few collisions.To define what kind of distribution to use for the energy loss we use the ratio between the mean energy loss ϵ to the maximum possible energy loss, T_{max} in a single collision.

$$k = \frac{\epsilon}{T_{max}} \tag{47}$$

If almost all the energy of the incident particle traversing the material is deposited, i.e. $(k > 10)$, the Gaussian distribution is used for description of the energy loss.

In the opposite case, the particle deposits only a part of its energy in material and for $(10 \geq k > 0.01)$ the Vavilov distribution should is used and for $(0.01 < k)$ the Landau distribution is used. The proton energy loss is represented by a Gaussian or Vavilov distribution, while for the electron a Landau distribution is used.

Using these calculations, the experimentally determined spectra have been corrected for these processes in order to compare them to theoretical calculations.

In this work, radiative corrections were performed as follows: The area under a histogram (the number of counts in a histogram) is called yield. For a fixed p_{miss} the ratio of the unradiated to the radiated yields, was calculated for each θ_{nq} bin using cross sections calculated with the model of Laget including FSI effects. Figures 51, 52, and 53 show the radiative correction factor for each θ_{nq} bin for the p_{miss} = 200, 400 and $500 MeV/c$ kinematics respectively. The experimental yields for each corresponding θ_{nq} bin are then multiplied by these ratios to correct the data for radiative effects.

7.7 Normalization

Previous data from Hall A and other world data indicate that the yields of the $^1H(e,e'p)$ elastic data for experiment E01-020 were about 20-25% below the known values [21]. The comparison was performed using different proton electromagnetic form factor parameterizations in MCEEP. Based on this discrepancy, it was decided

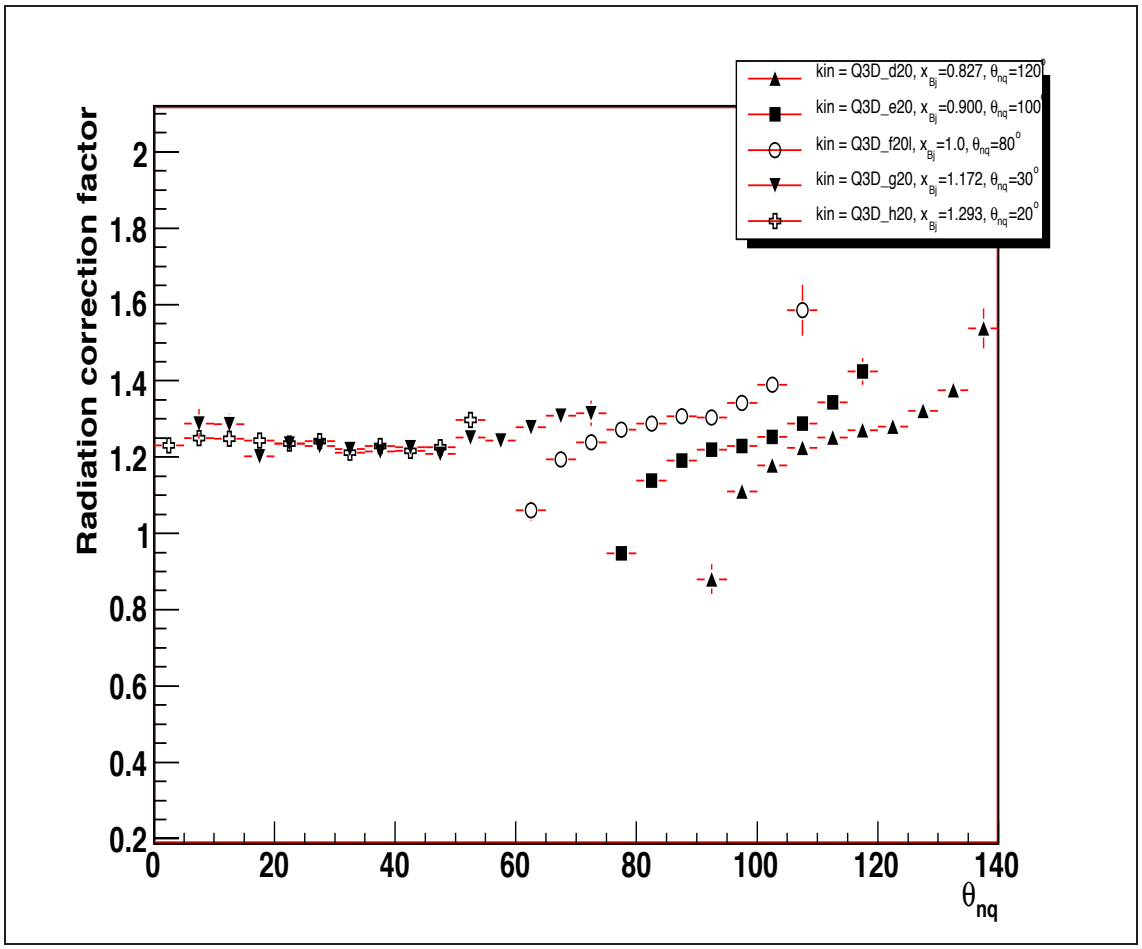

Figure 51: Radiative correction factor for each θ_{nq} for $p_{miss} = 200 MeV/c$ kinematics

to normalize the $^2H(e,e'p)n$ cross sections by using the normalization factor, fn = (0.78 ± 0.06). Extensive studies of this discrepancy indicate a problem at the trigger level. The trigger rates are much lower than expected. Same discrepancy appear in other Hall A experiments, though these other results are only preliminary.

7.8 Spectrometer acceptance

The coincidence events can be observed in a small kinematical region determined by the experimental configuration. The shape of this region is dependent primarily on the energy-momentum constraints of the reaction being studied. Other variables such

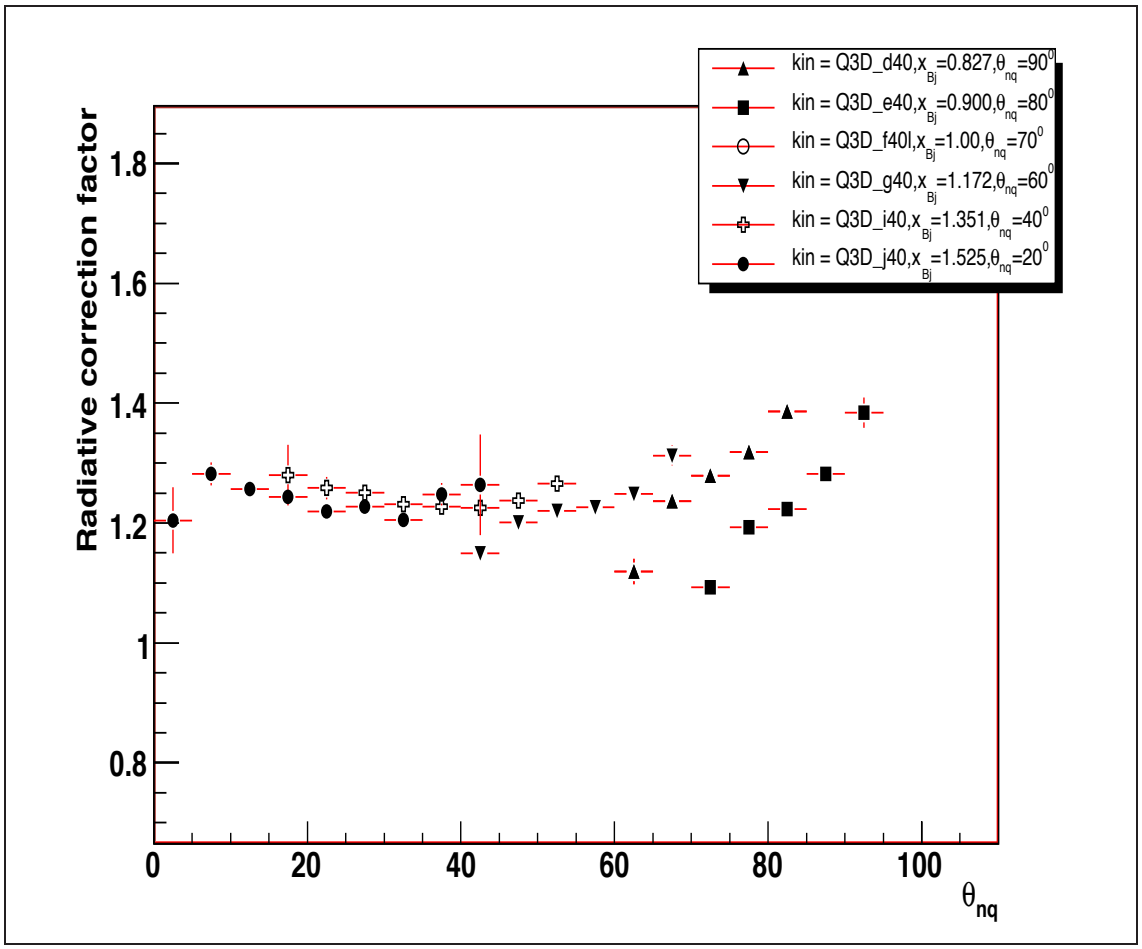

Figure 52: Radiative correction factor for each θ_{nq} for $p_{miss} = 400 MeV/c$ kinematics

as the spectrometer angles, collimators, detector efficiencies, scattering cell types and beam rastering contribute to the shape of this kinematical region (acceptance). The actual acceptance is very complex and the only possibility to determine it is to use a computer simulation. The probability that an event produced in a given region of the target with a given initial momentum and direction is accepted (rejected) defines the spectrometer acceptance. The geometrical acceptance of the spectrometer has been evaluated with the help of a Monte Carlo simulation. The simuation program uses a detailed geometrical description of the apparatus to account for the position and dimension of each individual detector element. In a coincidence experiment, two

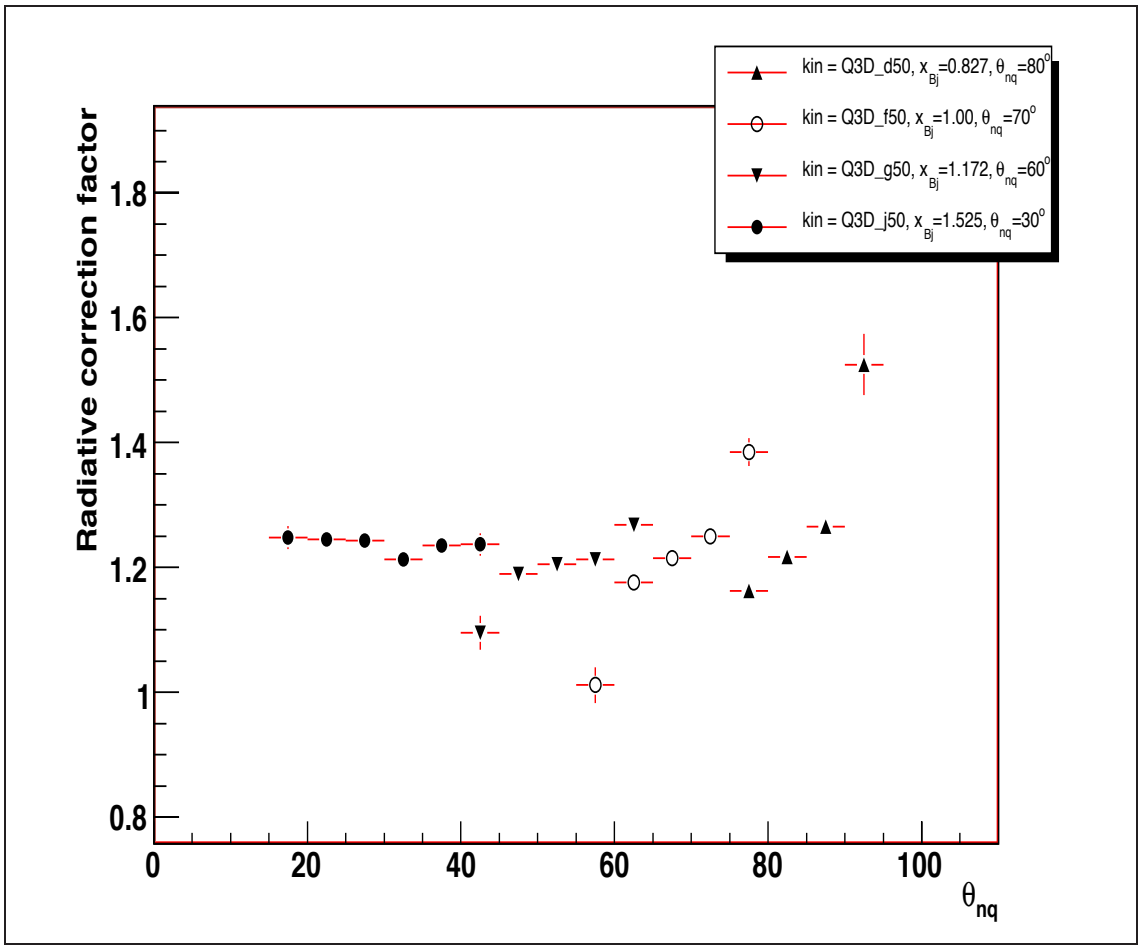

Figure 53: Radiative correction factor for each θ_{nq} for $p_{miss} = 500 MeV/c$ kinematics

spectrometers are used and the ranges of the kinematical variables that they cover (the so-called nominal spectrometer acceptance) are usually smaller than the ranges of the corresponding variables at the target.

7.9 R_function

When a charged particle of a certain momentum enters a spectrometer it moves on a trajectory determined by the spectrometer magnetic field. For each initial line of flight and momentum of the particle, there are two possibilities: the particle passes through the spectrometer to its focal plane, or is getting absorbed by internal

spectrometer apertures. This behavior can be modeled by an acceptance function, defined in the space of the initial particle trajectories and momenta, that assumes values of either 0 or 1. This modeling takes into account the geometry of the magnetic field in the spectrometer and the geometry of spectrometer apertures.

An R-function [54] is a real-valued function whose sign is completely determined by the signs of its arguments. The resulting function is equal to 0 on the boundary of the geometrical object, greater than 0 inside the object and less than 0 outside the object. In addition, the absolute value of the resulting R-function can be made approximately equal to the distance to the nearest boundary of the acceptance volume. The 5-dimensional HRS acceptance region is a complicated region that is not easy to visualize.

Events with positive values of the function lie inside the region of the initial acceptance cut, events with negative values of the function lie outside of the acceptance cut. In the above approximation the region were acceptance function is equal to 1 (flat or good acceptance region) a certain value of R defines a region in the 5-dimensional space of target variables x_{tg}, y_{tg}, ϕ_{tg}, θ_{tg}, δ_{tg}. R-functions, are very convenient because they make it is possible to uniformly enlarge or decrease the acceptance and, by comparing the result to a simulation, to see at what point experiment and simulation starts to deviate.

In Figures 54 trough 61 the value of this R-function is plotted for $^2H(e, e'p)$ experimental coincidence events for the electron arm (left) and the hadron arm (right)

as a dashed line, together with the results of a MCEEP simulation (solid circles) for various kinematics. The value of the function for a coincidence event characterizes how close is the event to the center of the combined left/right spectrometer acceptance defined by cuts.

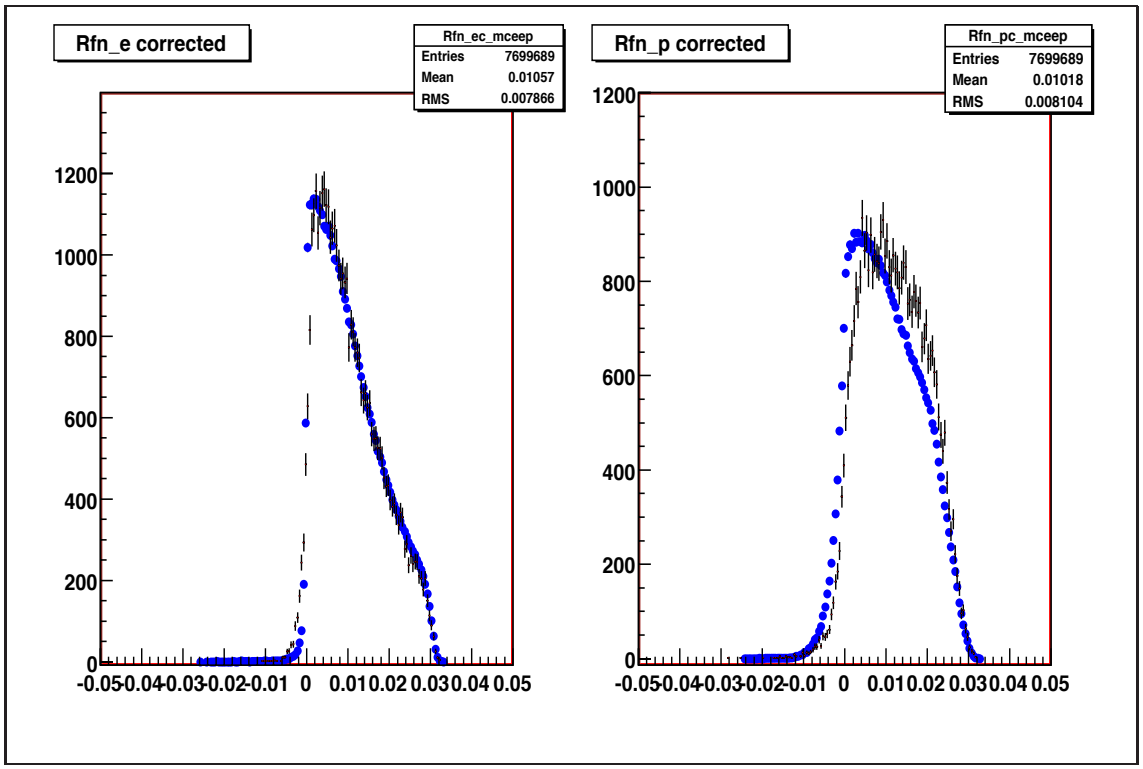

Figure 54: Rfn function for coincidence data electron arm (left) at 25.59 degrees and hadron arm (right) at 40.96 degrees, beam energy 5009 MeV (kin Q3D_h20).

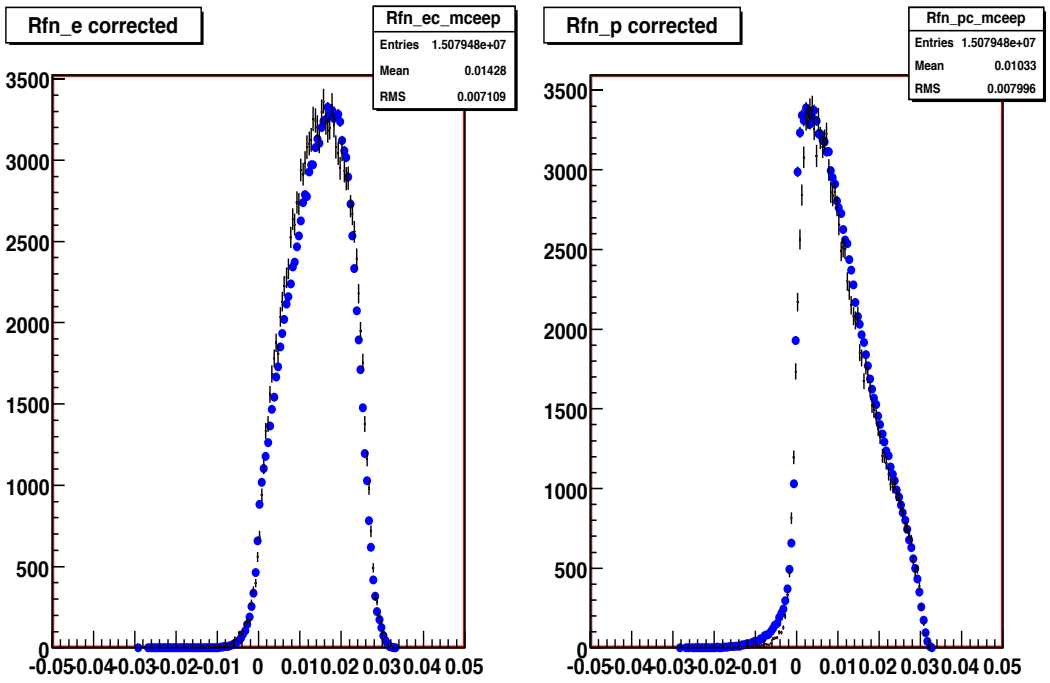

Figure 55: Rfn function for coincidence data electron arm (left) at 30.86 degrees and hadron arm (right) at 32.86 degrees, beam energy 5009 MeV (kin $Q3D\_e20$).

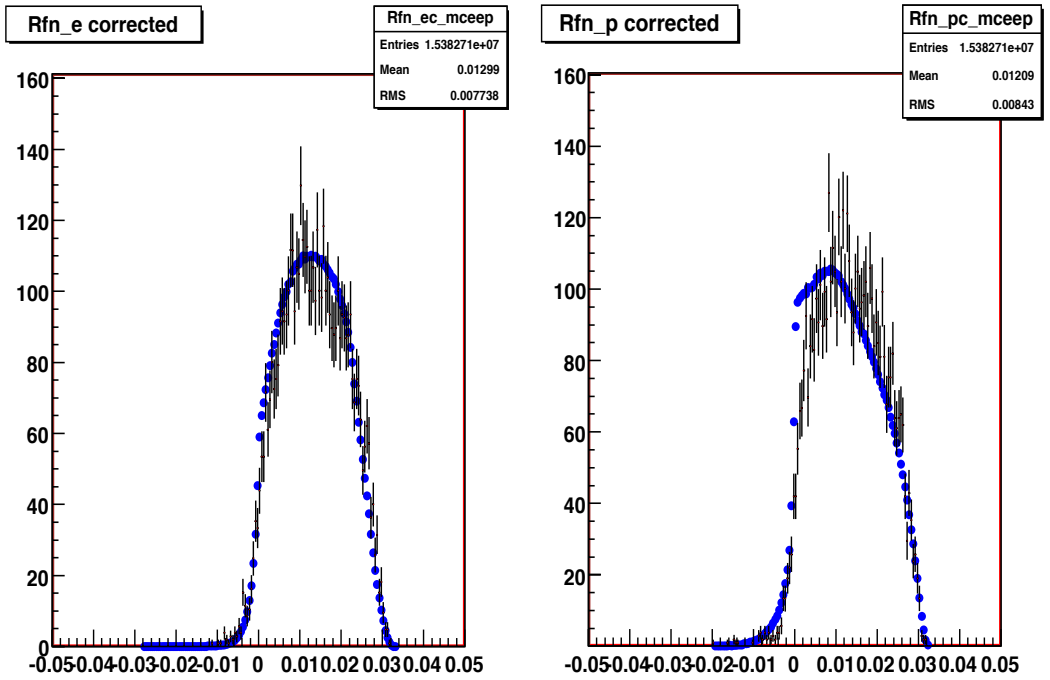

Figure 56: Rfn function for coincidence data electron arm (left) at 30.86 degrees and hadron arm (right) at 37.12 degrees, beam energy 5009 MeV (kin$Q3D_e40$).

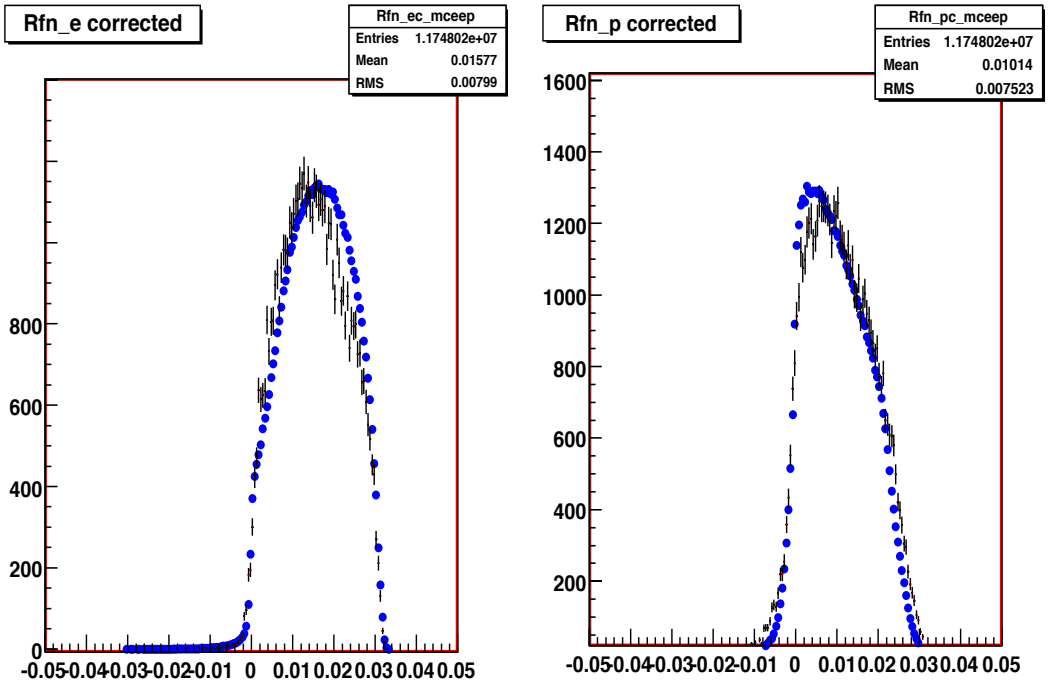

Figure 57: Rfn function for coincidence data left (electron) arm at 19.65 degrees and right (hadron) arm at 48.46 degrees, beam energy 5009 MeV (kin $Q3D\_f20l$).

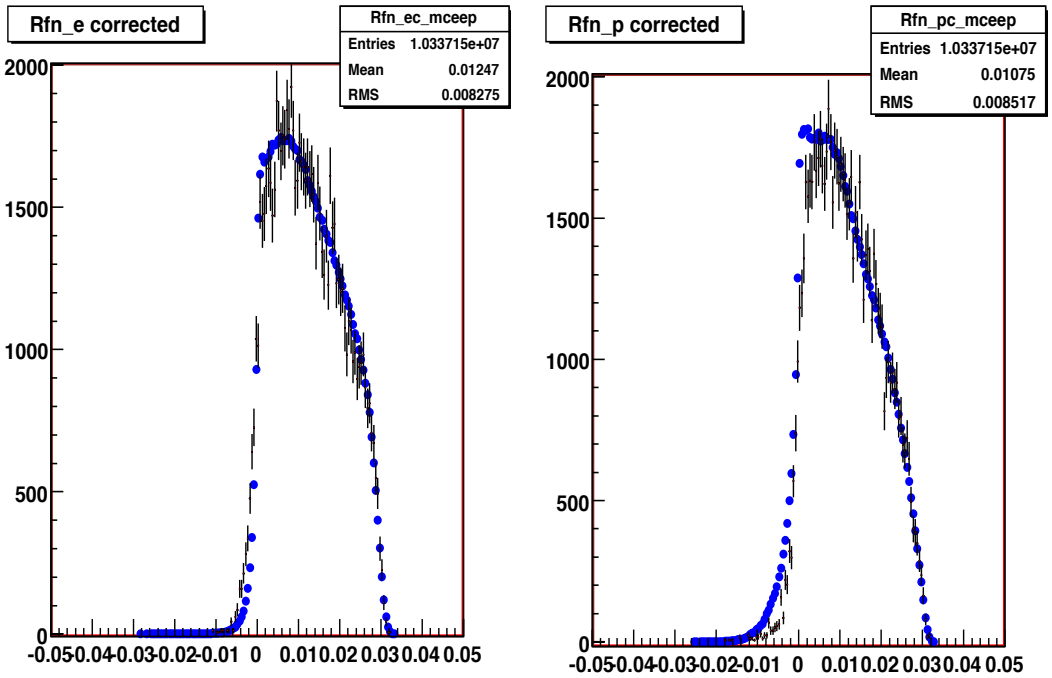

Figure 58: Rfn function for coincidence data electron arm (left) at 26.15 degrees and hadron arm (right) at 41.39 degrees, beam energy 5008.9 MeV (kin $Q3D\_g20$).

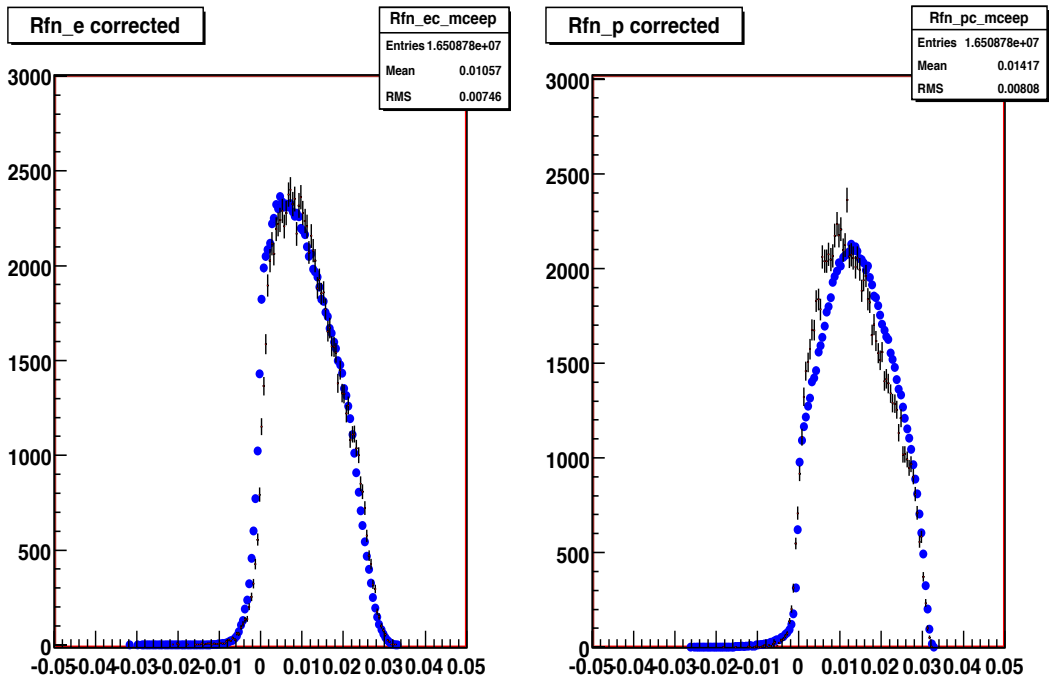

Figure 59: Rfn function for coincidence data electron arm (left) at 29.19 degrees and hadron arm (right) at 30.61 degrees, beam energy 5009 MeV (kin Q3D_d20)

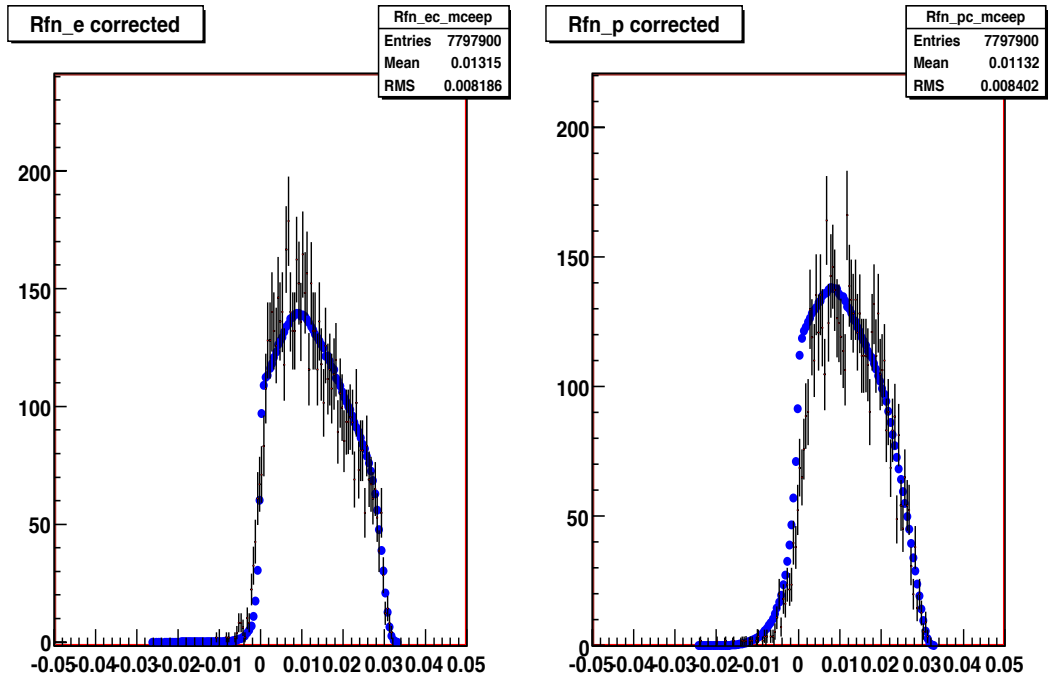

Figure 60: Rfn function for coincidence data electron arm (left) at 25.37 degrees and hadron arm (right) at 50.00 degrees, beam energy 5009 MeV (kin $Q3D\_i40$).

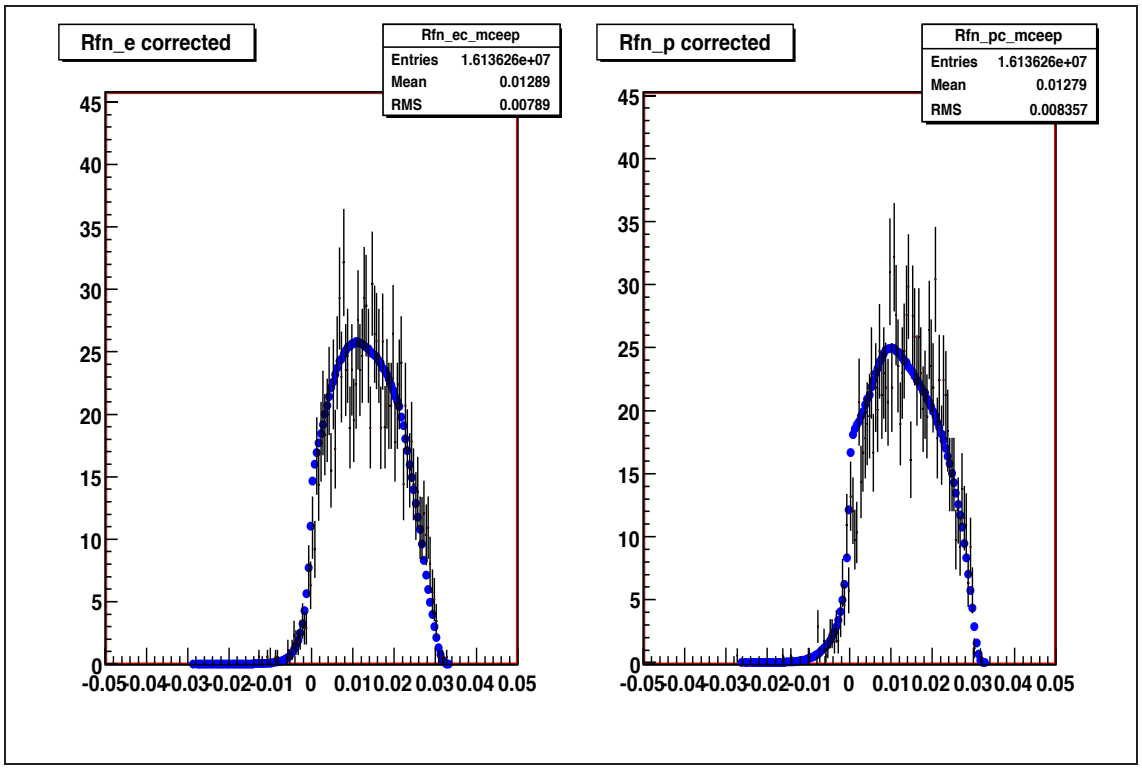

Figure 61: Rfn function for coincidence data electron arm (left) at 29.18 degrees and hadron arm (right) at 37.06 degrees, beam energy 5009 MeV (kin $Q3D\_d50$).

8 The Experimental (e,e'p) Cross Section

The (e,e'p) cross sections extracted in E01020 are bin-averaged five-fold differential cross sections. The method of extracting the cross sections and their relation to the theoretical cross sections is discussed below.

8.1 Five-fold differential cross section

The $^2H(e,e'p)n$ reaction produces a peak in the missing energy histogram with a width determined by the overall resolution of the experiment. In an (e,e'p) experiment we measure the number of events $N(E_{miss}, P_{miss})$ that fall within the missing energy and missing momentum bin (E_{miss}, P_{miss}). The total cross section is given by:

$$\sigma_{exp} = \frac{N_{bin}^{exp}}{N_{el\_inc} \cdot \Delta V_{ph\_space}} \tag{48}$$

where the number of events in the experimental bin is given by:

$$N_{bin}^{exp} = L \cdot t \cdot \Delta V \cdot \sigma_{(e,e'p)} \tag{49}$$

with L being the luminosity and t is the data taking time. The spectrometer phase space is (the total hyper-volume sampled over in the Monte Carlo):

$$\Delta V_{ph\_space} = \Delta\Omega_e \cdot \Delta\Omega_p \cdot \Delta\omega \tag{50}$$

where $\Delta\Omega_e = \Delta\theta_e \cdot \Delta\phi_e$ is the electron spectrometer opening and $\Delta\Omega_p = \Delta\theta_p \cdot \Delta\phi_p$ is the proton spectrometer opening.

The detection volume $\Delta V(E_{miss}, P_{miss})$ is calculated with a standard Monte Carlo technique:

$$\Delta V ph\_space = \frac{N_{inside}(E_{miss}, P_{miss})}{N_{trials}} \cdot \Delta\Omega_e \cdot \Delta\Omega_p \cdot \Delta\omega \tag{51}$$

$N_{inside}(E_{miss}, P_{miss})$ is the number of successful trials landing in the (E_{miss}, P_{miss}) bin and N_{trials} is the total number of trials. The kinematic variable of the outgoing electron for a particular trial were randomly sampled from the volume $\Delta\Omega_e \cdot \Delta\Omega_p \cdot \Delta\omega$ and the position of the incident electron beam on the target was rastered as in the experiment.

The five fold differential cross section is defined as:

$$\frac{d^5\sigma}{\Delta\Omega_e \cdot \Delta\Omega_p \cdot \Delta\omega} = \frac{N_{corr}(E_{miss}, P_{miss})}{V_{ph\_space}(E_{miss}, P_{miss})} \tag{52}$$

where: $N_{corr}(E_{miss}, P_{miss})$ is the corrected data yield and $V_{ph\_space}(E_{miss}, P_{miss})$ is the acceptance or phase-space per bin calculated by MCEEP. The corrected data yield can be written in therms of uncorrected data yield as follow:

$$N_{corr}(E_{miss}, P_{miss}) = \frac{f_{rad} \cdot N_{uncorr}(E_{miss}, P_{miss})}{CLT \cdot \epsilon_{VDC} \cdot f_{boil} \cdot f_n} \tag{53}$$

where:

- $N_{uncorr}(E_{miss}, P_{miss})$ is the uncorrected yield per bin,
- f_{rad} is the radiative correction factor,

- CLT is the computer live time,
- ϵ_{VDC} is the VDC efficiency,
- f_{boil} is the boiling correction factor,
- f_n is the normalization correction factor.

8.2 Cross section extraction

The individual steps in the extraction of the cross section for the $^2H(e,e'p)n$ reaction are summarized below.

- Subtract background of accidental events (in our kinematics this correction is negligible).
- Divide data counts, corrected for efficiencies, etc. by MCEEP phase space, each with appropriate acceptance and physics cuts (see below). This gives cross section before radiative correction
- Run MCEEP monte-carlo-simulation using radiated cross section [55] and unradiated (Laget=PW+FSI) and take the ratio to get the radiative correction. Laget-unradiated has all resolution effects turned off as well as energy loss and multiple scattering and, of course, internal bremsstrahlung.
- Multiply the data, bin-by-bin, by this ratio to get the radiatively corrected data.

- Run MCEEP bound state with all resolution effects turned off to generate the phase space.

- The data cross section is the number of corrected counts in the data (corrected for efficiencies and CDT) divided by the MCEEP phase space. This is done for each bin of interest. The end result is 5-fold differential cross section, corrected for radiative effects

8.3 Average kinematics simulation

Average kinematics results were studied in order to understand the observed variation of the cross section for a given p_{miss} as a function of the neutron angle. Different kinematical settings give different cross sections. The theory (e.g. for the p_{miss} = 200 MeV/c kinematics) gives a different cross section for the same θ_{nq} (the neutron angle) for different kinematics. A kinematical setting is not completly specified if one fixes the missing momenta and the angle of the recoiling neutron θ_{nq}. Different combinations of missing momenta and electron scattering angle yield the same θ_{nq}. The cut on missing momenta is $\pm$ 20 MeV/c. Within one central kinematic, the missing momenta is allowed to vary by 40 MeV/c about the nominal value. Low missing momenta translate in larger cross section. A drop of one degree in the electron scattering angle can easily make a $\sim$ 10% difference in the cross section.

In Appendix B simulated average kinematics are shown . Figures 75 through 77 show the simulated average missing momenta for each θ_{nq} bin for $p_{miss} \sim$ 200, 400 and 500 MeV/c kinematics, respectively. Figures 78 through 80 show the simulated average energy transfer ω for each θ_{nq} bin for p_{miss} = 200, 400 and 500 MeV/c kinematics, respectively. Figures 81 through 83 show the simulated average 3-momentum transfer , $|\vec{q}|$ for each θ_{nq} bin for p_{miss} = 200, 400 and 500 MeV/c kinematics, respectively.

Figures 84 through 86 show the simulated average electron scattering angle for each θ_{nq} bin for p_{miss} = 200, 400 and 500 MeV/c kinematics, respectively.

8.4 Systematic uncertainties

The systematic uncertainties are divided into "normalization" uncertainties which propagate as a multiplicative correction to the extracted cross section and other uncertainties.

Sources of systematic uncertainty in the measured $(e, e'p)$ cross sections are given in Table 6 and are described in detail in this section. The rows of the table consider uncertainties due to possible offsets in the central value of kinematic quantities such as the beam energy, beam angles, scattered particles momenta and spectrometer angles.

Quantity	Symbol	Uncertainty
Incident beam energy ($\pm$ 160 KeV)	δE_{beam}	0.3 $\times 10^{-3}$
Beam out-plane angle	θ_{Beam}	0.1 mrad
Beam in-of-plane angle	ϕ_{Beam}	0.1 mrad
Scattered electron energy	δ e'	0.15 $\times 10^{-3}$
Scattered electron in-plane angle	$\theta_{e'}$	0.12 mrad
Scattered electron out-of-plane angle	$\phi_{e'}$	0.23 mrad
Outgoing proton momentum	δ_p	0.23 $\times 10^{-3}$
Proton out-plane angle	θ_p	0.13 mrad
Proton in-of-plane angle	ϕ_p	0.29 mrad

Table 6: Kinematic systematic uncertainties for the beam and the particles detected in the two spectrometers. E_{Beam} is the incident electron energy, e is the scattered electron energy, p is the momentum of the proton, and θ and ϕ are the in-plane and out-of-plane angles for each particle. These uncertainties folded into the MCEEP simulation suite.

Tables 9, 10, and 11 in Appendix D, summarize the kinematic errors due to the sensitivity of the cross section for quasi-elastic $^2H(e, e'p)n$ scattering with beam energy equal to 5000 MeV and four momentum transfer $Q^2 = 3.5(MeV/c)^2$ to θ_{Beam},

ϕ_{Beam}, $\delta e'$, $\theta_{e'}$, $\phi_{e'}$, δ_p, θ_p, ϕ_p. Coincidence cross sections can vary strongly with kinematics. The kinematic error were determined with the code SYSTERR written by P. Ulmer and K. Fissum [56]. This code works in conjunction with MCEEP and calculates the change of the cross section due to small variation of each of the quantities mentioned in table 6 averaged over the acceptance, according to the following steps. The SYSTERR code calculates the nominal cross section and uses the uncertainties given in Table 6 to calculate nine other cross sections for shifts equal to each of the kinematic uncertainties in turn (with all others at nominal values). The fractional variations of the nine cross sections from the nominal cross

Quantity	Global Uncertainty δ (%)
Beam Charge	1
Target Boiling Correction	2
Data Acquisition dead time	1
Electronics deadtime	1
VDC detection efficiency	1
VDC tracking efficiency	1
Triggering Efficiency	1
Particle identification	1
Radiative Corrections	1
Normalization	6
Sum in Quadrature	7

Table 7: Estimates of other systematic uncertainties associated with the $^2H(e,e'p)n$ cross section measurements. Global uncertainties refer to kinematics independent uncertainties which are common to all kinematics settings and bins.

section are shown in Fig. 87 through 89, Appendix C, for two different kinematics ($Q3D\_f20l$ and $Q3D\_j50$). The magnitude of these uncertainties depend upon p_{miss}. The total (quadrature sum) of the fractional shifts (kinematics dependent systematic uncertainties) as a function of θ_{nq} angle are shown in Appendix C, in Figures 90

through 92 for kinematics $Q3D\_f20l$, $Q3D\_f40l$, and $Q3D\_j50$, respectively. In tables 10 and 11 are given the total systematic uncertainties (in %) for each theta bin for which the cross sections were measured. Other kinematical errors associated with the cross section measurements are listed in Table 7. These uncertainties were extracted from archives from previous experiments performed in Hall A. The sum in quadrature of the kinematical and non-kinematical errors give the total error associated with the $^2H(e,e'p)n$ cross section measurements.

8.5 Results and Discussions

Figures 62 through 64 show the cross sections for the $^2H(e,e'p)n$ reaction extracted for missing momenta values, p_{miss}, equal to 200, 400 and 500 MeV/c, respectively, as a function of the angle θ_{nq}, between the vector momentum transfer, $\vec{q}$, and the direction of the residual neutron. The cross sections were measured at a beam energy of 5 GeV and a four momentum transfer squared Q^2=3.5 (MeV/c)^2. The cross sections have had the radiative effects removed, and are corrected for all dead times and inefficiencies. The error bars shown are total errors. The statistical error are plotted on top of the total errors. Various marker styles differentiate between kinematics (see Appendix A).

In Fig. 62 one can see the variation of the extracted cross section as a function of the θ_{nq} angle, for different kinematical settings. When changing from one kinematic to another the angle θ_e is varied in order to keep Q^2 constant, while x_{Bj} changes. This change in θ_e is reflected in the measured cross section since θ_e enters the elementary cross section, σ_{ep}, as $\frac{cos^2(\theta_e)}{sin^4(\theta_e)}$, a function that varies rapidly with the θ_e setting. This explains the variations observed in the measured cross section, at the same θ_{nq} bin. For comparison also plotted are the theoretical cross sections for the same kinematics (continous lines). The calculations, provided by J. M. Laget, include FSI effects. For p_{miss} = 200 MeV/c (Fig. 62), the calculation is in good agreement with the measured cross section for central angle $\theta_{nq} = 80^o$. For angles $\theta_{nq} < 70^o$ the theory is slightly above and for $\theta > 90^o$ slightly below the measured cross sections.

Figure 63, for p_{miss}=400 MeV/c, shows that for angles $\theta_{nq} < 60^o$ the theory is above the measured cross sections. For angles $\theta_{nq} > 60^o$ the theory underestimates the measured cross sections.

For $p_{miss} = 500$ MeV/c (Fig. 64), the calculation describes very well the measured cross section at central $\theta_{nq} = 70^o$. Same behavior as for the p_{miss}= 200 MeV/c and p_{miss}= 400 MeV/c kinematics is observed here. For angles $\theta_{nq} < 60^o$, the theory overpredicts the experimental cross sections while for $\theta_{nq} > 75^o$ the theory predictions are below the measured cross sections.

In tables 13 and 14 are given the measured cross section values along with the associated statistical uncertainties.

8.5.1 Comparison to theory

In order to exhibit the effect of FSI, the ratio between the experimental and the simulated PWIA cross section, $T = \frac{\sigma_{exp}}{\sigma_{PWIA}}$, as a function of the θ_{nq} angle was measured.

The position of the peak of the ratio T was compared to GEA predictions and Glauber theory predictions. The experimental ratio T shows θ_{nq} dependence, and agrees quite well with the theoretical GEA prediction. The T distributions show that the peak of T is around $\theta_{nq} = 75^0$. Figure 65 shows the measured ratio T, as a function of the angle θ_{nq}, for missing momenta values of $p_{miss} = 200$ MeV/c, $p_{miss} = 400$ MeV/c and $p_{miss} = 500$ MeV/c, respectively. For missing momenta of

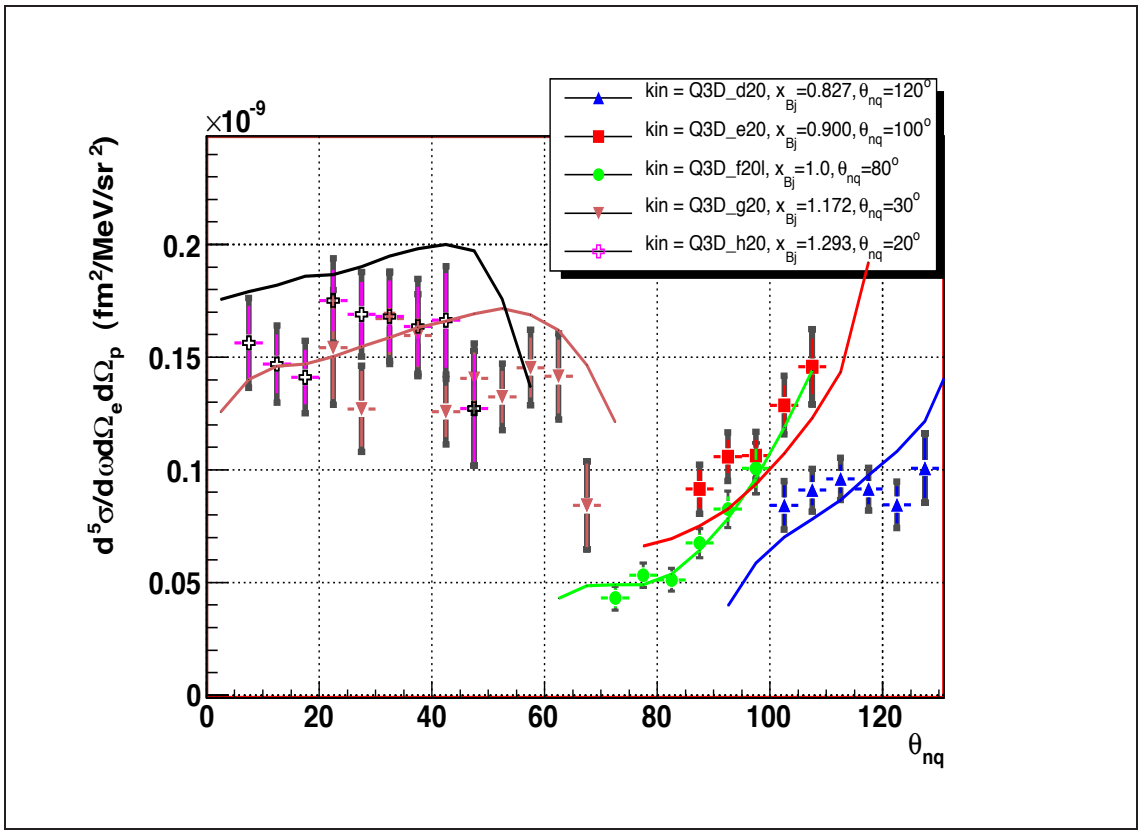

Figure 62: $^2H(e,e'p)n$ cross section as a function of θ_{nq} for $p_{miss} = 200 MeV/c$ kinematics. Statistical errors are plotted on top of total errors (ticker lines).

200 MeV/c the ratio T, as a function of θ_{nq}, has a small dip at angles θ_{nq} between 60 and 80 degrees. For a missing momenta of 400 MeV/c there is an enhancement in the ratio T up to a factor ~ 2.4 and up to a factor ~ 2.7 for a missing momenta of 500 MeV/c. A well known example of the eikonal approximation of FSI is the Glauber approximation [10]. However, the latter was derived for cases where one can neglect the motion of bound nucleons in the nucleus. For the $^2H(e,e'p)n$ reaction at large missing momenta, the eikonal approximation was generalized (GEA) in order to account for finite values of nucleon momenta [13]. According to recent calculations [13, 55, 57, 58, 59] FSI are supposed to develop large contributions that result in

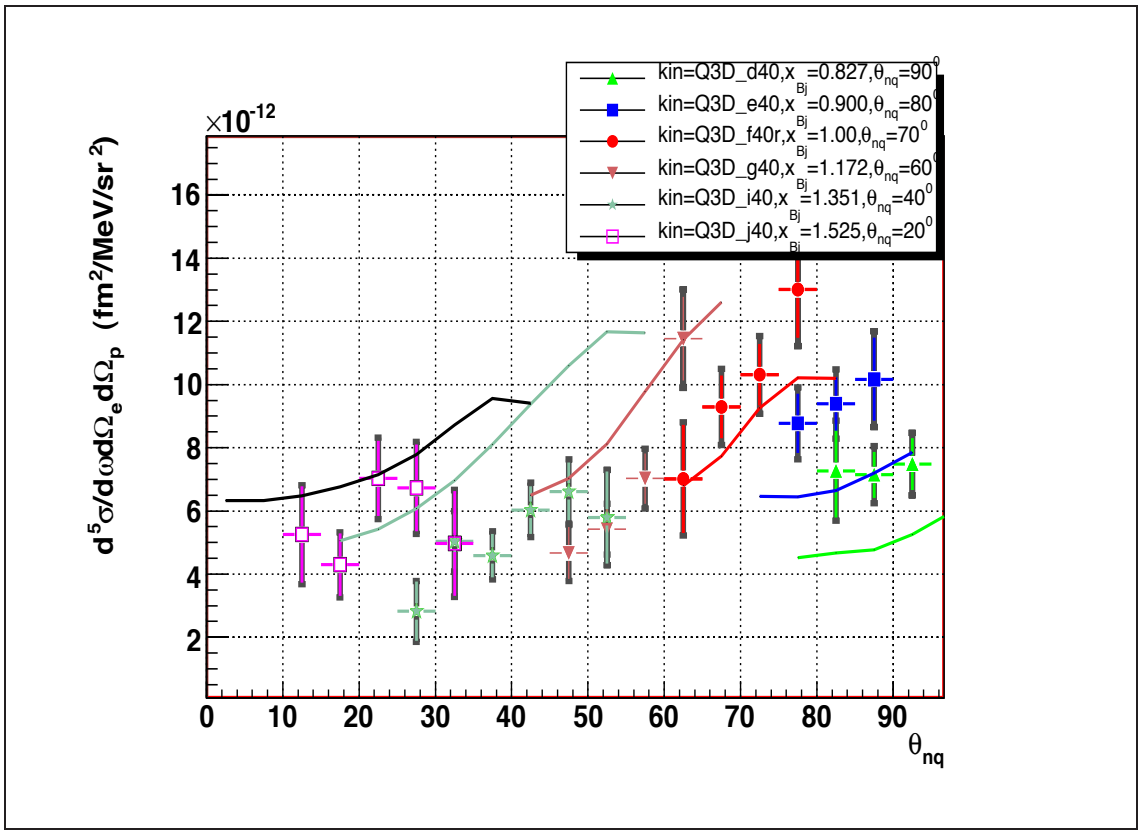

Figure 63: $^2H(e,e'p)n$ cross section as a function of θ_{nq} for $p_{miss} = 400 MeV/c$ kinematics. Statistical errors are plotted on top of total errors (ticker lines).

an increase in the cross section for high missing momentum kinematics compared to what PWIA predicts. Figures 68 through 70 present the experimental results for the ratio $T = \frac{\sigma_{experim}}{\sigma_{PWIA}}$ along with the theoretical calculations by Sargsian [60], the ratio $T = \frac{\sigma_{Sargsian}}{\sigma_{PWIA}}$, for p_{miss}=200 MeV/c, p_{miss} = 400 MeV/c and p_{miss} = 500 MeV/c, respectively.

The results of our experiment show that the conventional Glauber approximation, modified to describe correctly relativistic kinematics and the dynamics of FSI's (which is done within the generalized eikonal approximation), properly describe the overall structure of the reaction. Figure 66 represents the ratio of the $^2H(e,e'p)n$

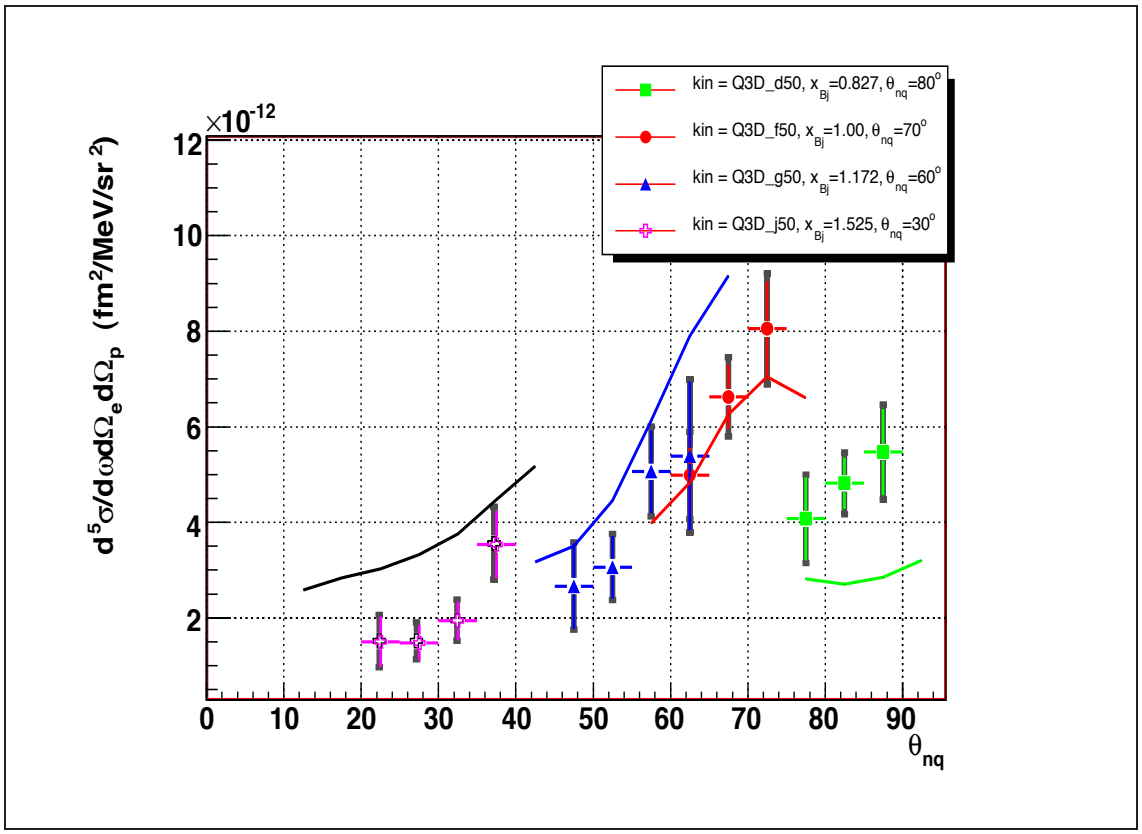

Figure 64: $^2H(e,e'p)n$ cross section as a function of θ_{nq} for $p_{miss} = 500 MeV/c$ kinematics. Statistical errors are plotted on top of total errors (ticker lines).

cross section calculated in the PWIA and FSI terms to the cross section which includes the PWIA term only, as a function of the angle θ_{nq} for different neutron (spectator) momenta [13]. The dashed line in this figure corresponds to the conventional Glauber approximation and indicates the position of the peak to be at $\theta_{nq} = 90^0$. The solid line represent the GEA calculations with relativistic effects included and indicate the position of the peak in the ratio to be at $\theta_{nq} = 70^0$.

Figures 72 through 74 present the experimental results for the ratio $T = \frac{\sigma_{experim}}{\sigma_{PWIA}}$ along with the theoretical Laget ratio $T = \frac{\sigma_{Laget}}{\sigma_{PWIA}}$, for p_{miss}=200 MeV/c, p_{miss} = 400 MeV/c and p_{miss} = 500 MeV/c, respectively. These results demonstrate that GEA,

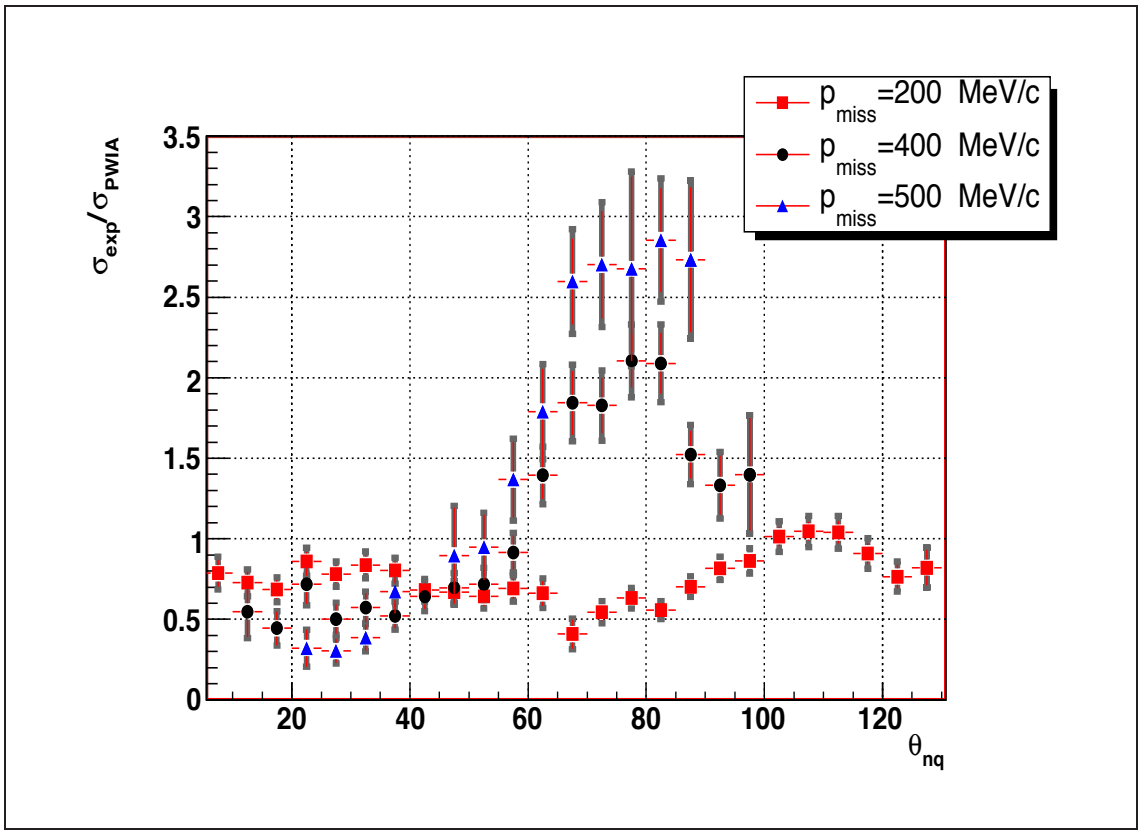

Figure 65: The ratio between the experimental cross section to the PWIA simulated cross section $T = \frac{\sigma_{exp}}{\sigma_{PWIA}}$ as a function of the θ_{nq} angle for missing momenta values of p_{miss} = 200 MeV/c, p_{miss} = 400 MeV/c and p_{miss} = 500 MeV/c.

which takes into account the nuclear fermi motion, provides a better description of the reaction than the standard Glauber theory. The experimental values of T show a θ_{nq} dependence that agrees quite well with the general shape of the theoretical prediction. In addition, the T distributions show that the peak of T is around $\theta_{nq} = 75^0$ (or $x_{Bj} \sim 1$), as predicted for the first time in 1997 in theoretical calculations of Sargsian et al. [13].

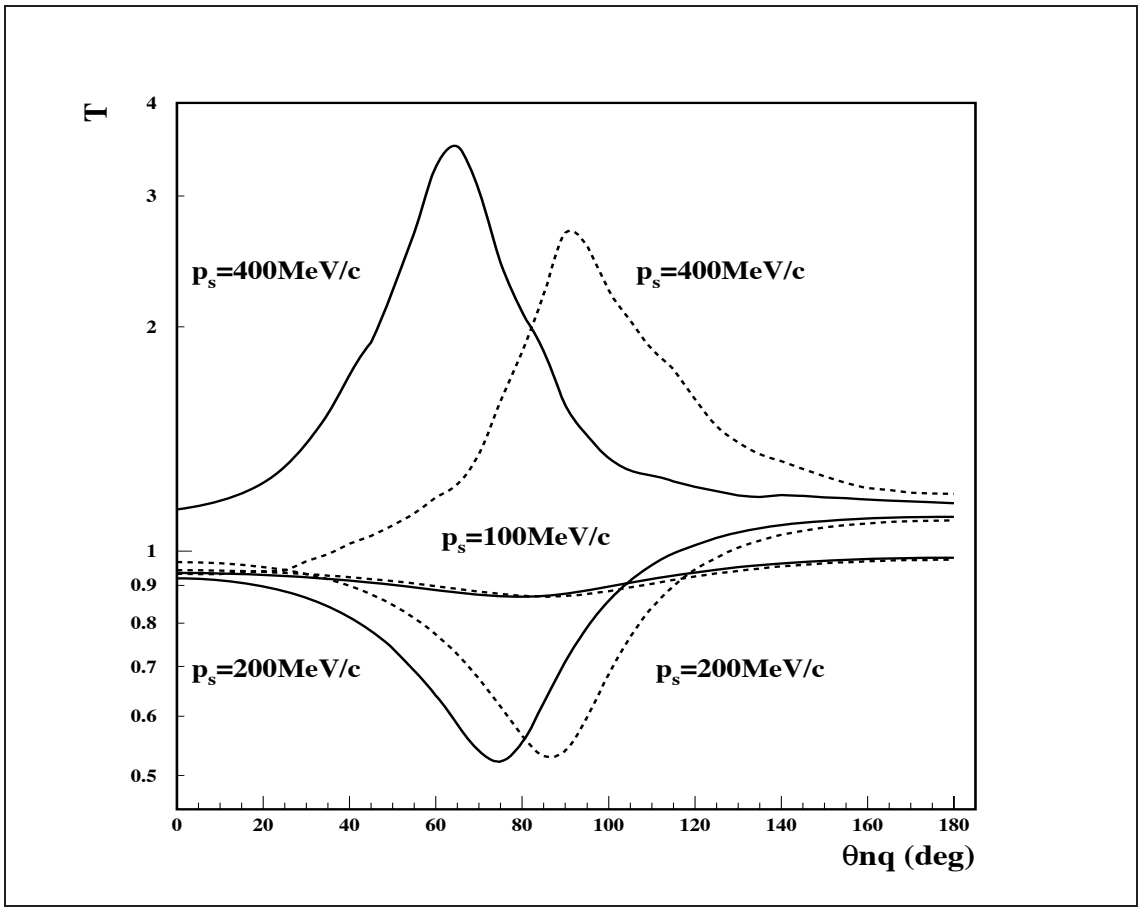

Figure 66: ${}^2H(e,e'p)n$ ratio between the theoretical (Sargsian) cross section and PWIA cross section as a function of θ_{nq} [13]. The continuous line represent the GEA calculation and the dashed line represent the standard Glauber calculation.

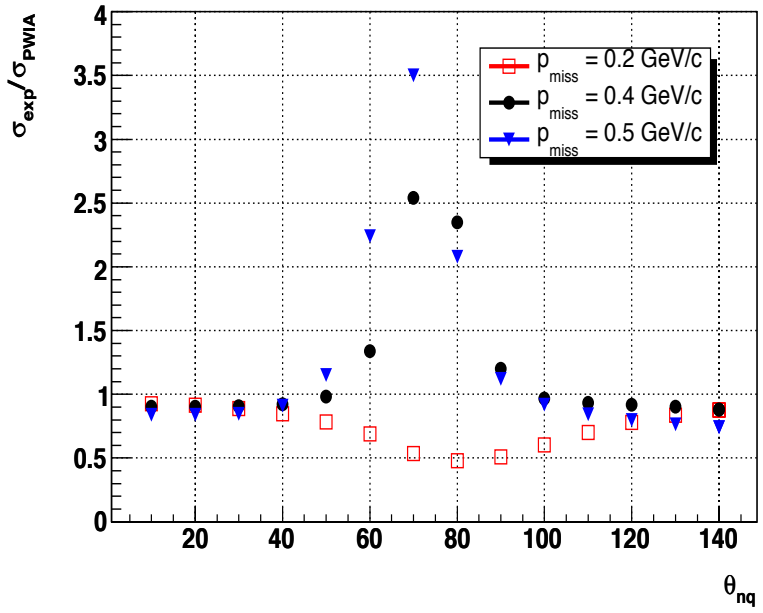

Figure 67: The ratio between the Sargsian cross section to the PWIA simulated cross section $T = \frac{\sigma_{Sargsian}}{\sigma_{PWIA}}$, as a function of the θ_{nq} angle for missing momenta values of $p_{miss} = 200 MeV/c$, $p_{miss} = 400 MeV/c$ and $p_{miss} = 500 MeV/c$.

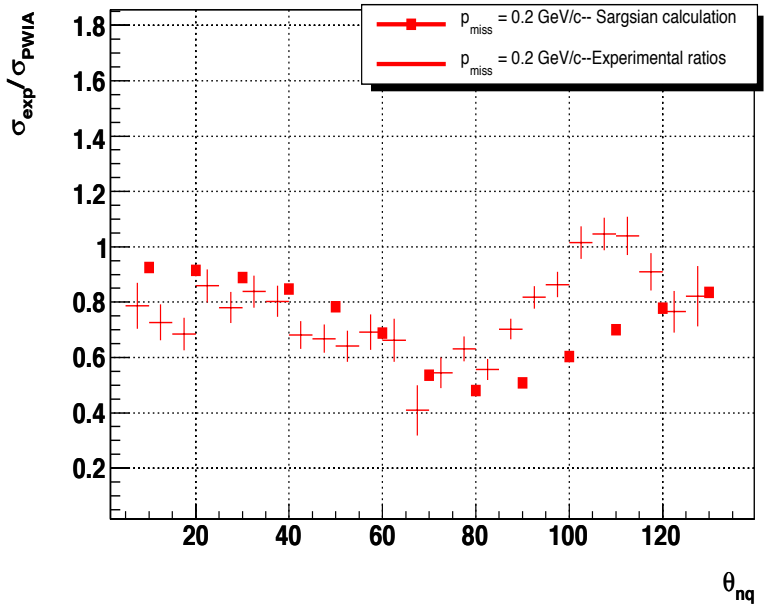

Figure 68: The ratio between the experimental cross section to the PWIA simulated cross section $T = \frac{\sigma_{experim}}{\sigma_{PWIA}}$, as a function of the θ_{nq} angle for missing momenta values of $p_{miss} = 200 MeV/c$ (stars) and the ratio between the Sargsian cross section to the PWIA simulated cross section $T = \frac{\sigma_{Sargsian}}{\sigma_{PWIA}}$, as a function of the θ_{nq} angle for missing momenta values of $p_{miss} = 200 MeV/c$ (squares).

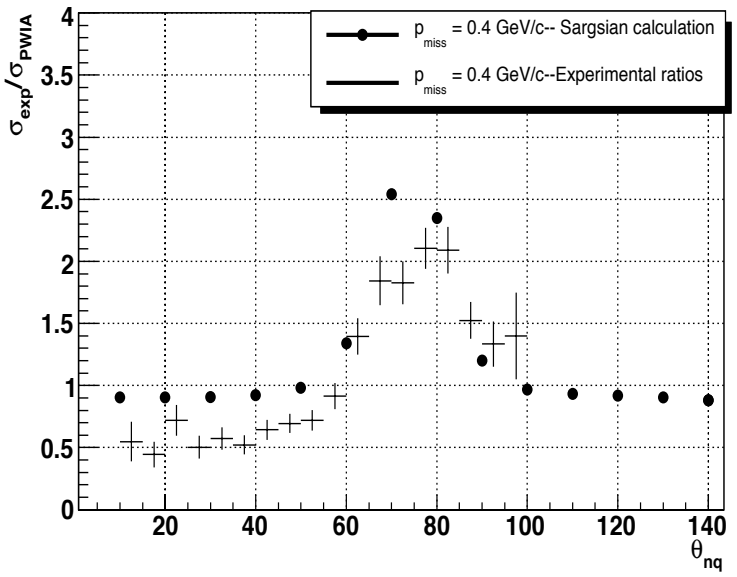

Figure 69: The ratio between the experimental cross section to the PWIA simulated cross section $T = \frac{\sigma_{experim}}{\sigma_{PWIA}}$, as a function of the θ_{nq} angle for missing momenta values of $p_{miss} = 400 MeV/c$ (stars) and the ratio between the Sargsian cross section to the PWIA simulated cross section $T = \frac{\sigma_{Sargsian}}{\sigma_{PWIA}}$, as a function of the θ_{nq} angle for missing momenta values of $p_{miss} = 400 MeV/c$ (circles).

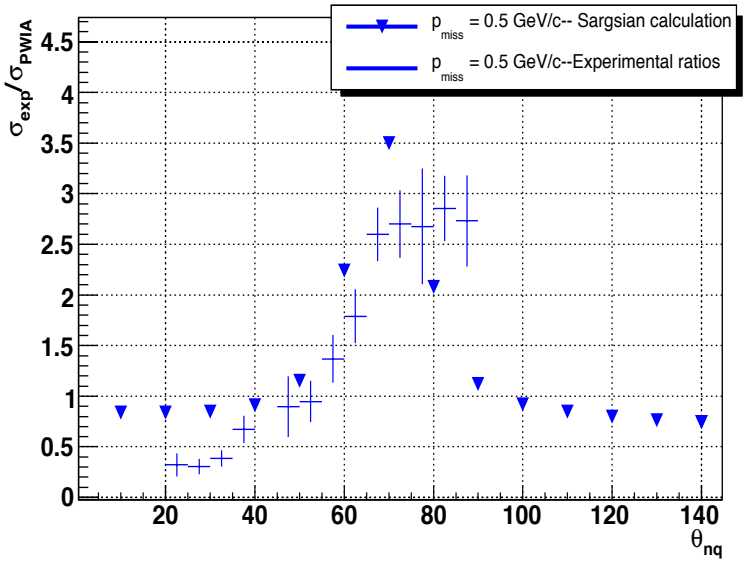

Figure 70: The ratio between the experimental cross section to the PWIA simulated cross section $T = \frac{\sigma_{experim}}{\sigma_{PWIA}}$, as a function of the θ_{nq} angle for missing momenta values of p_{miss}=500 MeV/c (stars) and the ratio between the Sargsian cross section to the PWIA simulated cross section $T = \frac{\sigma_{Sargsian}}{\sigma_{PWIA}}$, as a function of the θ_{nq} angle for missing momenta values of p_{miss}=500 MeV/c (triangles).

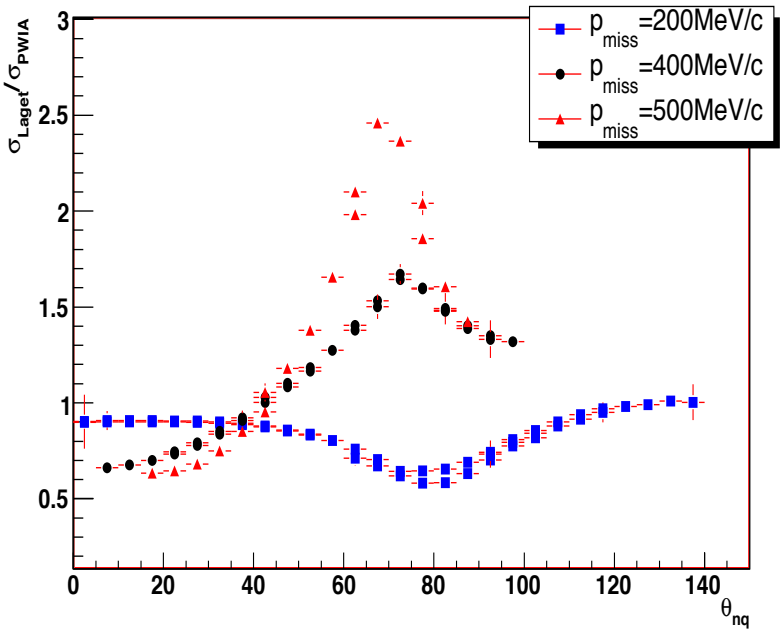

Figure 71: The ratio between the Laget cross section to the PWIA simulated cross section $T = \frac{\sigma_{Laget}}{\sigma_{PWIA}}$, as a function of the θ_{nq} angle for missing momenta values of $p_{miss} = 200 MeV/c$, $p_{miss} = 400 MeV/c$ and $p_{miss} = 500 MeV/c$.

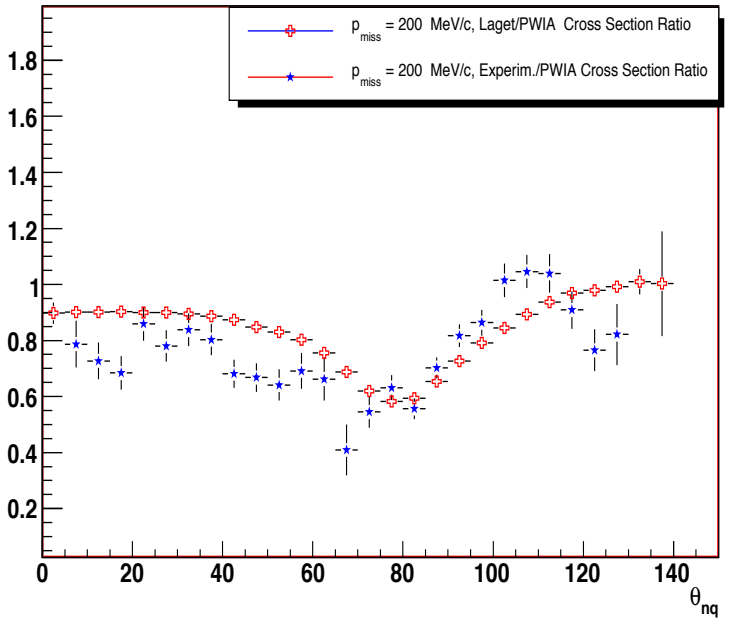

Figure 72: The ratio between the experimental cross section to the PWIA simulated cross section $T = \frac{\sigma_{experim}}{\sigma_{PWIA}}$, as a function of the θ_{nq} angle for missing momenta values of $p_{miss} = 200 MeV/c$ (stars) and the ratio between the Laget cross section to the PWIA simulated cross section $T = \frac{\sigma_{Laget}}{\sigma_{PWIA}}$, as a function of the θ_{nq} angle for missing momenta values of $p_{miss} = 200 MeV/c$ (crosses)

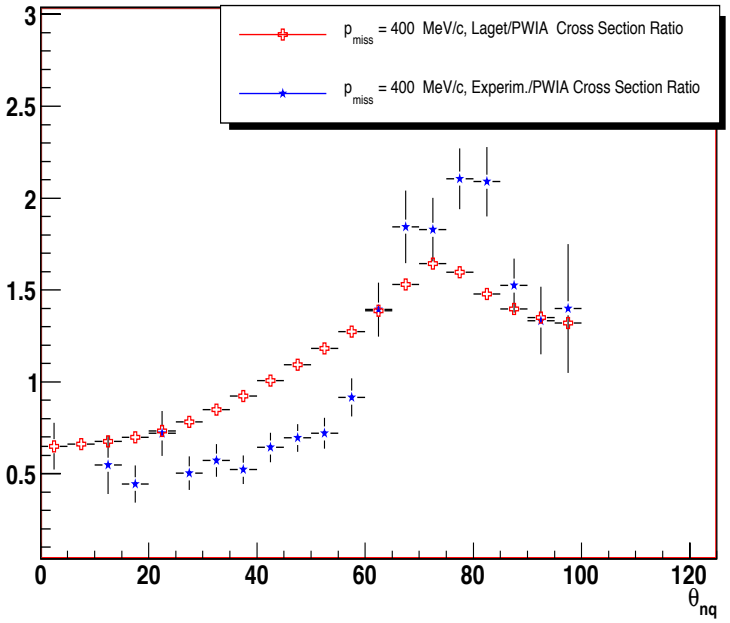

Figure 73: The ratio between the experimental cross section to the PWIA simulated cross section $T = \frac{\sigma_{experim}}{\sigma_{PWIA}}$, as a function of the θ_{nq} angle for missing momenta values of $p_{miss} = 400 MeV/c$ (stars) and the ratio between the Laget cross section to the PWIA simulated cross section $T = \frac{\sigma_{Laget}}{\sigma_{PWIA}}$, as a function of the θ_{nq} angle for missing momenta values of $p_{miss} = 400 MeV/c$ (crosses).

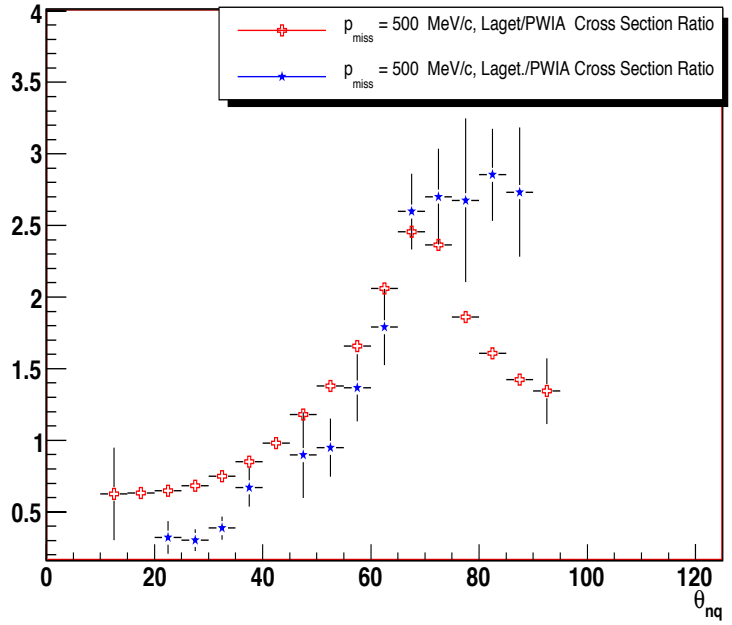

Figure 74: The ratio between the experimental cross section to the PWIA simulated cross section $T = \frac{\sigma_{experim}}{\sigma_{PWIA}}$, as a function of the θ_{nq} angle for missing momenta values of p_{miss}=500 MeV/c (stars) and the ratio between the Laget cross section to the PWIA simulated cross section $T = \frac{\sigma_{Laget}}{\sigma_{PWIA}}$, as a function of the θ_{nq} angle for missing momenta values of p_{miss}=500 MeV/c (crosses).

9 Summary

This experiment was an extensive and systematic study of the nucleon knockout reaction on the deuteron in a kinematical region close to the QE peak at high Q^2. The major goal was to measure the cross section of the $^2H(e,e'p)n$ reaction, with the emphasis toward higher missing momenta which were not studied in previous experiments. The current experimental results test predictions of FSI effects as a function of the scattering angle of the outgoing neutron at a fixed four momentum transfer Q^2.

The measurements were performed at a central momentum transfer of $|q|$ ~2400 MeV/c, at a central energy transfer of $\omega \sim 1500$ MeV, and for a four momentum transfer $Q^2 = 3.5$ (GeV/c)^2, covering missing momenta from 0 to 0.5 GeV/c. The majority of the measurements were performes at $\Phi = 180^o$ and a small set of measurements were done at $\Phi = 0^o$. Absolute $^2H(e,e'p)n$ cross sections were obtained as a function of the recoiling neutron scattering angle with respect to $\vec{q}$. These results were compared to a Plane Wave Impulse Approximation (PWIA) model and to a calculation that includes FSI effects. Experimental $^2H(e,e'p)n$ cross sections were determined with an estimated systematic uncertainty of 7 %. Final State Interactions (FSI) contributions were found to depend strongly on the angle of the recoiling neutron with respect to the momentum transfer, and on the missing momentum. We found a systematic deviation of the theoretical prediction of about 30 %. At small θ_{nq} ($\theta_{nq} <\sim 60^o$) the theory overpredicts the cross section while at large θ_{nq}

(θ_{nq} >80^o) the theory underestimates the cross sections. The general features of the measured cross sections are reproduced by the Glauber (GEA) based calculations that take into account the motion of the bound nucleons. We observed about a 240 % enhancement of the cross section, as compared to PWIA, due to FSI, for a missing momentum of 0.4 GeV/c at an angle of 75^o. For missing momentum of 0.5 GeV/c the enhancement of the cross section due to the same effects was about 270 %. This is in agreement with GEA. Standard Glauber calculations predict this large contribution to occur at an angle of 90^o. Our results show that GEA better describes the $^2H(e,e'p)n$ reaction.

Final state interactions (FSI), meson exchange currents (MEC), and isobar configurations (IC) effects are not independent from each other. There is no complete theoretical treatment which include all of these effects. The present theories are improved with respect to the relativistic contributions to the internal dynamics. High-precision $^2H(e,e'p)$ cross section measurements, thus, represent an important means of testing our understanding of the NN interaction. In order to achieve a better agreement between theory and experiment, significant improvements are still necessary.

References

[1] B. Povh, K. Rith, C. Scholz, F. Zetsche, Paticles and Nuclei - An Introduction to the Physical Concepts, 1995.

[2] J. Carlson, R Schiavilla, Rev. Mod. Phys. 70, 743, (1998).

[3] B. A. Mecking Eur. Phys. J. A 28, s01, 209 (2006)

[4] M. Bernheim et al., Nucl. Phys. A365, 349 (1981).

[5] H. Breuker et al.,Nucl. Phys. A455, 641 (1986).

[6] K.I. Blomqvist et al, Phys. Lett. B 424, 33 (1998).

[7] M. van der Schaar et al, Phys. Rev. Lett. 66, 2855 (1991).

[8] M. van der Schaar et al, Phys. Rev. Lett. 68, 776 (1992).

[9] P.E. Ulmer et al., Phys. Rev. Lett. 89,6 (2002).

[10] R.J. Glauber Phys. Rev. 100,242 (1995).

[11] Lectures in Theoretical Physics, v.1, ed. W. Brittan and L. G. Dunham, Interscience Publ., N.Y., 1959

[12] L. L. Frankfurt, W.R. Greenberg, G.A. Miller, M.M. Sargsian and M. I. Strikman, Z. Phys. A352 97 (1995)

[13] L. L. Frankfurt, M.M. Sargsian, M. I. Strikman, Phys. Rev. C 56 1124 (1997).

[14] Misak M. Sargsian, Selected topics in high energy semi-exclusive electro-nuclear reactions, Int. J.Mod.Phys. E10 405-458, (2001).

[15] C. E. Carlson, J. R. Hiller and R. J. Holt, Ann. Rev. Nucl. Part. Sci. 47, 395 (1997).

[16] W. Boeglin, M. Jones, A. Klein, P. Ulmer, E. Voutier, et. al, *(e,e',p)* Studies of the deuteron at high Q^2, Jefferson Lab E01-020 proposal, (1998)

[17] F. Frommberger et al, Phys. Lett. B 339, 17 (1994).

[18] H.J. Bulten et al, Phys. Rev. Lett. 74, 4775 (1995).

[19] Hadrons in the Nuclear Medium, Misak Sargsian et. all, Journals of Physics, G29 (2003).

[20] A. Bianconi, S. Boffi, and D. E. Kharzeev, Physical Review C, 49.R124338. Quantum interference effects in N^* electroproduction and propagation in nuclei, 10.1103/PhysRevC.49.R1243 (1993).

[21] Hassan F. Ibrahim, The ^{2}H(e, e$_0$p)n Reaction at high momentum transfer,Ph.D. thesis, Old Dominion University, December (2006).

[22] S. Turck-Chieze et al, Phys. Lett. 142B, 145 (1984).

[23] H. Arenhovel, W. Leidemman, L. Tomusiak, Phys. Rev. C 52-1232, (1995).

[24] T. Tamae et al, Phys. Rev. Lett. 59, 2919 (1987).

[25] J.E. Ducret et al, Phys. Rev. C 49, 1783 (1994).

[26] D. Jordan et al, Phys. Rev. Lett. 76, 1579 (1996).

[27] A. Pellegrino et al, Phys. Rev. Lett. 78, 4011 (1997).

[28] W.-J. Kasdorp et al, Phys. Lett. B 393, 42 (1997)

[29] B.D. Milbrath et al, Phys. Rev. Lett. 80, 452 (1998).

[30] B.D. Barkhu, Ph.D. thesis, MIT (1997).

[31] K. Joo, Ph.D. thesis, MIT (1997).

[32] S. Frullani and J. Mougey, Adv. Nucl. Phys. 14, (1985).

[33] T. de Forest, Nucl. Phys. A 132-305, (1969).

[34] A.E.L. Dieperink and T. de Forest, Ann. Rev. Nucl. Sci. 25-1 (1975).

[35] Jefferson Lab, Hall A 3-dimensional image library, http://www.jlab.org/help/Ghelp/halla3d.html.

[36] W.U. Boeglin Czechoslovak Journal of Phys. 45-295 (1995).

[37] John Alcorn et. al., Basic Instrumentation for Hall A at Jefferson Jab, Nuclear Instruments and Methods in Physics Research, Section A, NIM A 522, (2004).

[38] P. E. Ulmer, I. Karabekov, A. Saha, P. Bertin, P. Vernin, JLab internal report, CEBAF-TN-94-001 (2001) .

[39] J. H. Mitchell et. all, Hall A Experimental Equipment Operations Manual, http://hallaweb.jlab.org/document/OPMAN/.

[40] O.K.Baker and other, Nucl. Instrum. Meth. A367, 92 (1995).

[41] J. Litt and R. Meunier, Ann. Rev. Nucl. Sci. **23**, 1 (1973).

[42] D. Abbot et al., The CODA System and its Performance in the First Online Experiments at CEBAF, Proceedings of the 1995 IEEE Conference on Real-Time Computing Applications in Nuclear, Particle and Plasma Physics, pp 147-151, May (1995).

[43] Robert Michaels, Trigger Programming for Hall A Spectrometers, http://hallaweb.jlab.org/equipment/daq/daq_trig.html, (2002).

[44] Robert Michaels, Bodo Reitz, James Proffitt, Update on electronics deadtime, JLAB, http://www.jlab.org/r̃om/edt_annrpt_2001.ps, (2001).

[45] Jefferson Lab, Hall A ESPACE users guide available at: http://hallaweb.jlab.org/espace/docs.html.

[46] Nilanga Liyanage, Optics Calibration of the Hall A High Resolution Spectrometers using the new optimizer. http://www.jlab.org/ñilanga/physics/optics.ps.

[47] D.S. Armstrong, Target Density Fluctuations and Bulk Boiling in the Hall A Cryotarget, D.S. Armstrong & all, JLAB-TN-03-017.

[48] ROOT: An Object-Oriented Data Analysis Framework available at: http://root.cern.ch/.

[49] P.E. Ulmer LH_2 Target Density in Hall A Experiment E01-020 Jlab-TN-05-064, July 28, (2005).

[50] P.E. Ulmer, VDC Tracking in Experiment E01-020, JLab internal report, (2003).

[51] P.E. Ulmer, Monte Carlo for (e,e'p) events, http://hallaweb.jlab.org/software/mceep/mceep.html.

[52] J. Schwinger Phys. Rev. 76-790 (1949).

[53] H. A. Bethe and W. Heitler Proc. Roy. Soc. A 146-83 (1943).

[54] Marat Rvachev, Effective use of JLab Hall A HRS acceptance with R-functions, Massachusetts Institute of Technology December 5, 2001.

[55] J. M. Laget, arXivnucl-th/0303052(2003).

[56] P. Ulmer and K. Fissum, Jefferson Lab Thech. Note 02-015,(2002).

[57] S. Jeschonnek and T.W. Donnelly, Phys. Rev. C59-2676 (1999).

[58] S. Jeschonnek, Phys. Rev. C63-034609 (2001).

[59] C. Ciofi degli Atti and L. P. Kaptari, Phys. Rev. Lett. 95-052502, (2005).

[60] Misak Sargsian, private communication, June 2007.

[61] Jefferson Lab, Hall A Electronic log records for experiment E01_020: http://www.jlab.org/ãdaq/halog/html/0206_archive/logdir.html.

Appendices

A List of Kinematics

A list of the kinematics for Experiment E01-020; data from Hall A Electronic log [61].
Kinematic: is the name given to a set of measurements taken at certain Q^2 and missing momenta values.
E0_Tief (GeV): is the energy of the incoming electron.
L_ANGLE: is the electron scattering angle;
R_ANGLE : is the angle at which the proton is detected;
Q^2 (MeV/c^2): is the value of the squared 4 momentum transfer;
X_Bjorken: is the value of the x Bjorken variable.

Kin.	E0_Tief (GeV)	L_ANGLE	R_ANGLE	Q^2 $(MeVc^2)$	X_Bjorken
Q3_d20	5.00899	29.1971	30.612	3.5	0.8258
Q3_d40	5.00905	29.1971	35.0082	3.5	0.8258
Q3_d50	5.00905	29.1971	37.0601	3.5	0.8258
Q3_e20	5.00899	30.8601	32.8612	3.5	0.9001
Q3_e40	5.00905	30.8601	37.1201	3.5	0.9001
Q3_f20l	5.00905	19.6501	43.4601	3.5	1.0001
Q3_f40l	5.00899	27.2893	24.4206	3.5	0.9978
Q3_f40r	5.00875	27.2893	41.6394	3.5	0.9980
Q3_f50	5.00841	27.2893	43.7719	3.5	0.9983
Q3_g20	5.00898	26.1539	41.3901	3.5	1.1686
Q3_g40	5.00897	26.1539	46.2598	3.5	1.1686
Q3_g50	5.00897	26.1539	48.531	3.5	1.1686
Q3_h20	5.00915	25.5876	40.9601	3.5	1.2895
Q3_i40	5.00895	25.3729	48.9999	3.5	1.3452
Q3_j40	5.00896	24.8302	48.6595	3.5	1.5175
Q3_j50	5.00894	24.8302	52.5558	3.5	1.5175

Table 8: Kinematic Q3: data taken at Q^2= 3.5 MeV/c^2

B Simulated Average Kinematics for $^2H(e,e'p)n$

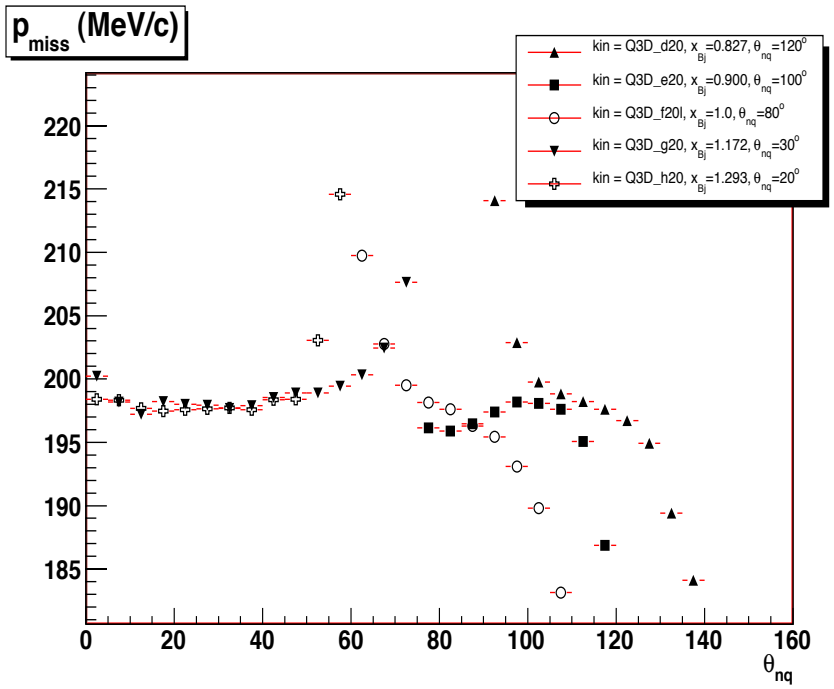

Figure 75: Simulated average missing momenta for each θ_{nq} bin for $p_{miss} \sim 200 MeV/c$ kinematics.

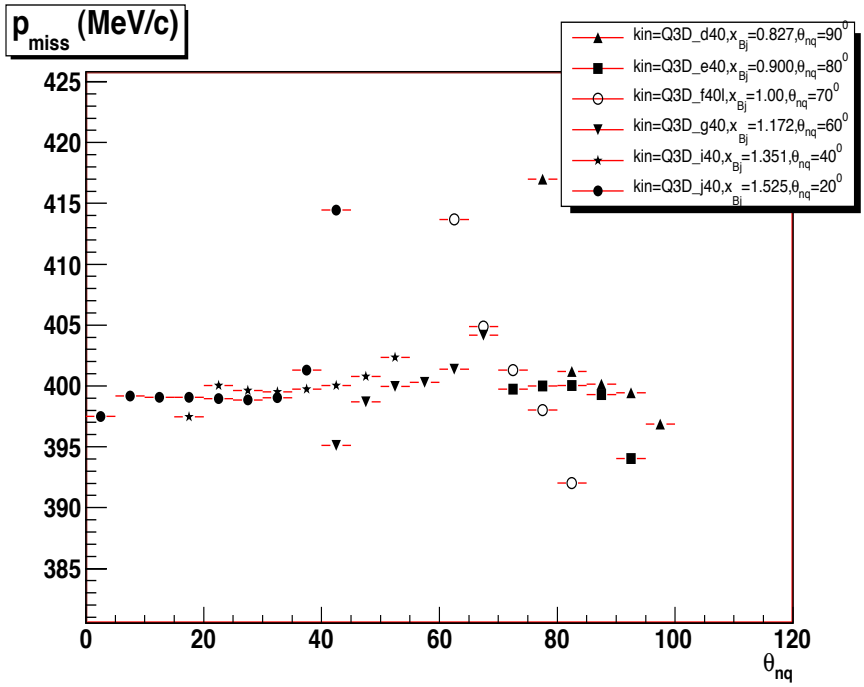

Figure 76: Simulated average missing momenta for each θ_{nq} bin for $p_{miss} \sim 400 MeV/c$ kinematics.

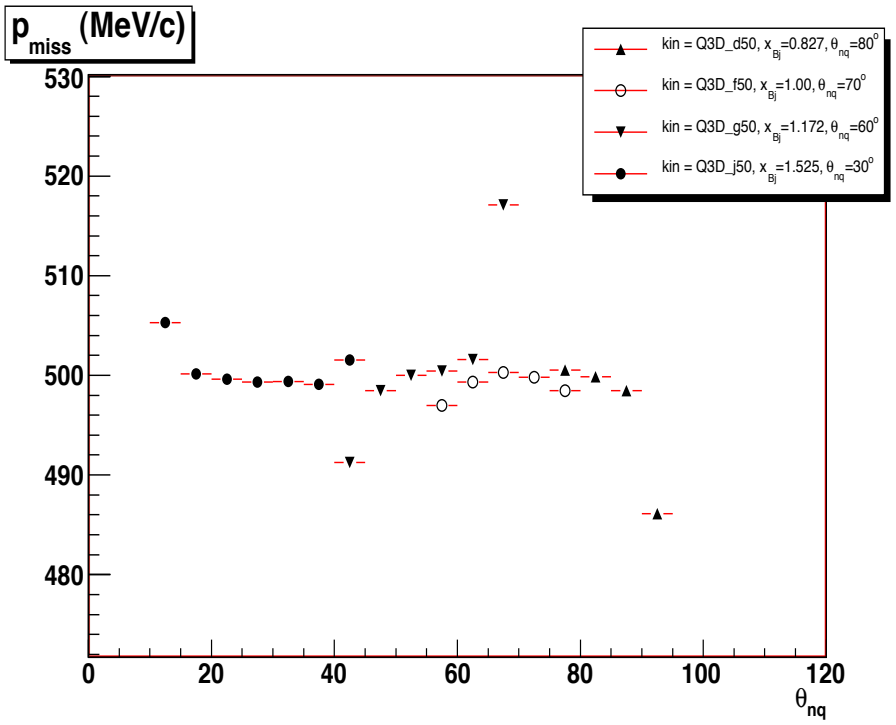

Figure 77: Simulated average missing momenta for each θ_{nq} bin for $p_{miss} = \sim 500 MeV/c$ kinematics.

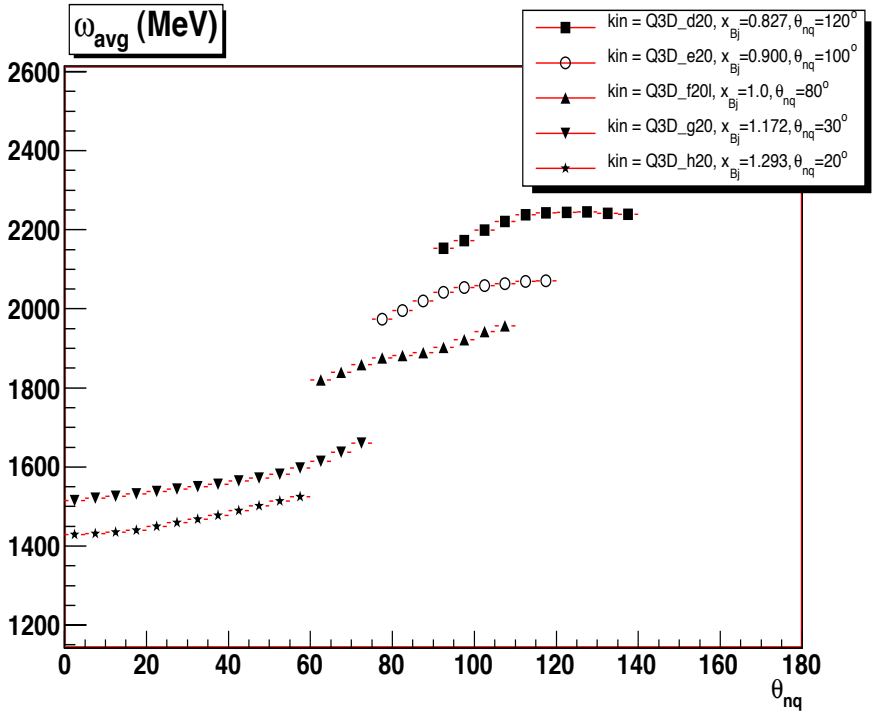

Figure 78: Simulated average energy transfer ω for each θ_{nq} bin for $p_{miss} = 200 MeV/c$ kinematics.

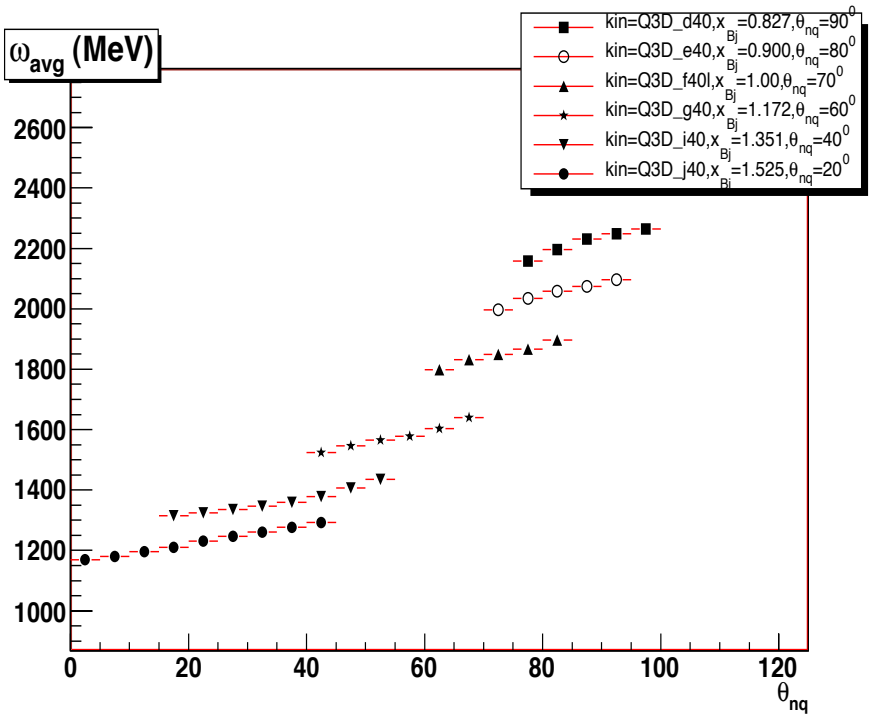

Figure 79: Simulated average energy transfer ω for each θ_{nq} bin for $p_{miss} = 400 MeV/c$ kinematics.

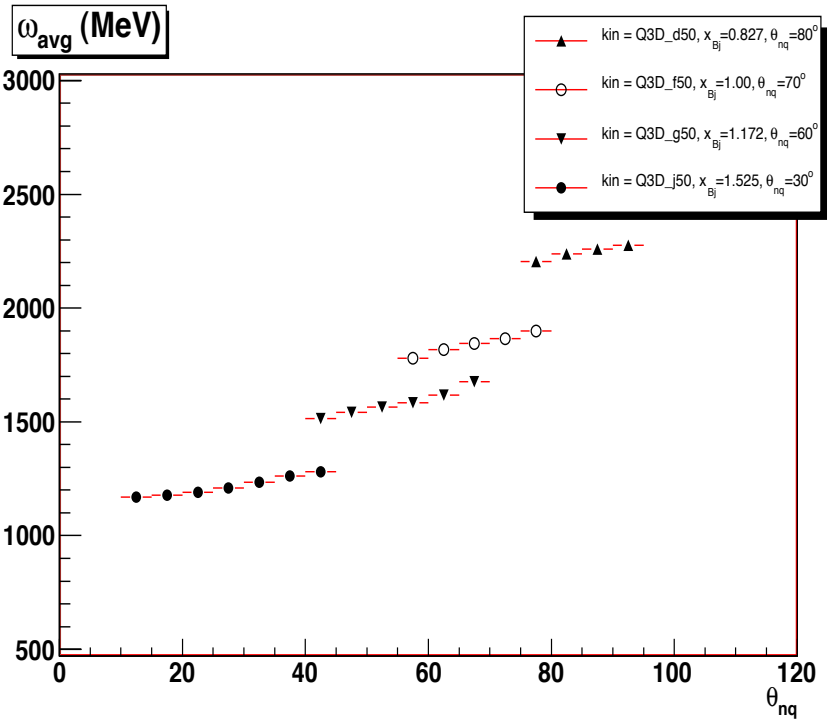

Figure 80: Simulated average energy transfer ω for each θ_{nq} bin for $p_{miss} = 500 MeV/c$ kinematics.

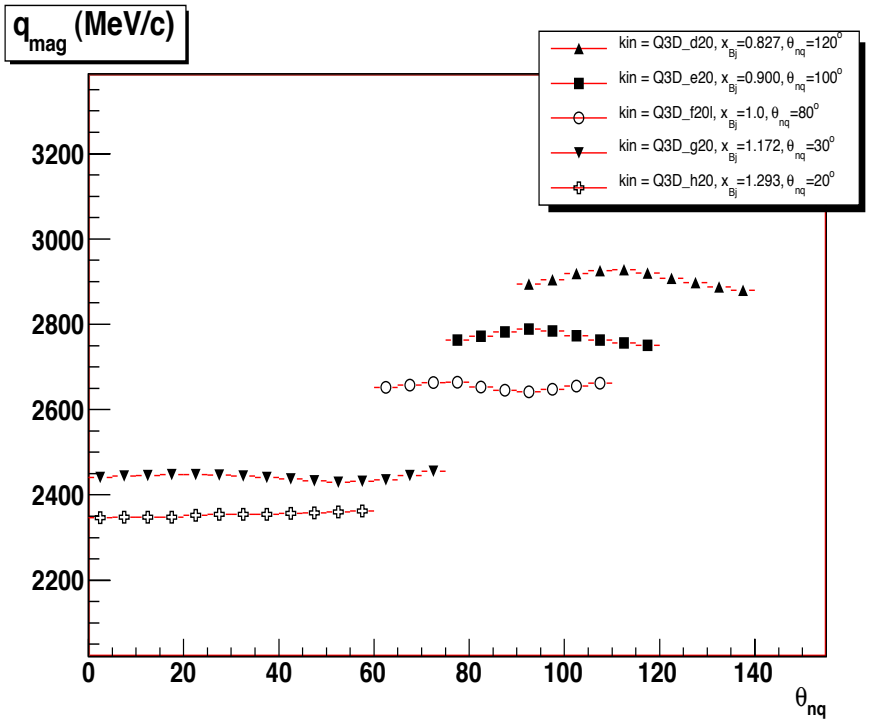

Figure 81: Simulated average 3-momentum transfer , $|\vec{q}|$, for each θ_{nq} bin for $p_{miss} = 200 MeV/c$ kinematics.

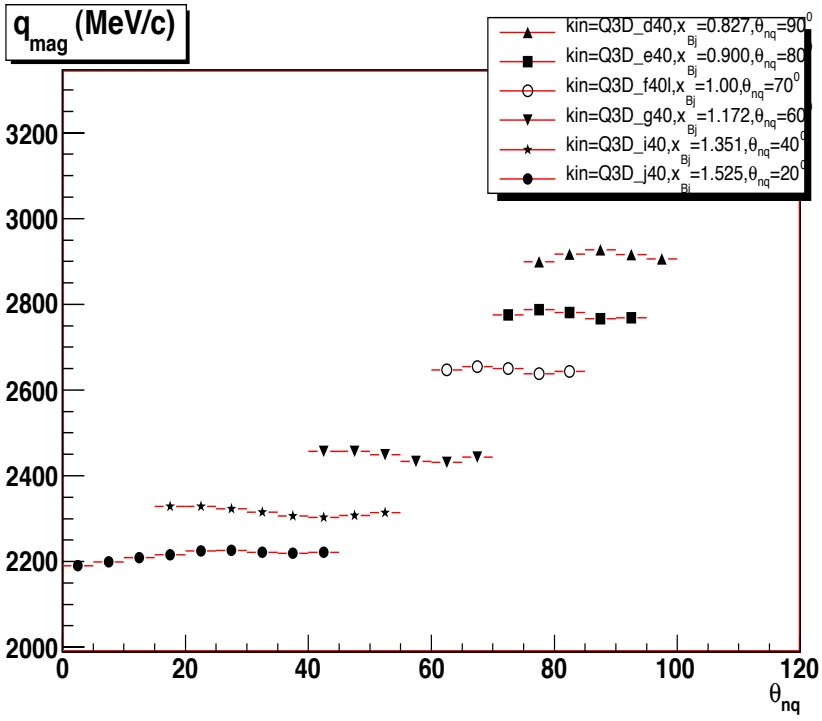

Figure 82: Simulated average 3-momentum transfer , $|\vec{q}|$, for each θ_{nq} bin for $p_{miss} = 400 MeV/c$ kinematics.

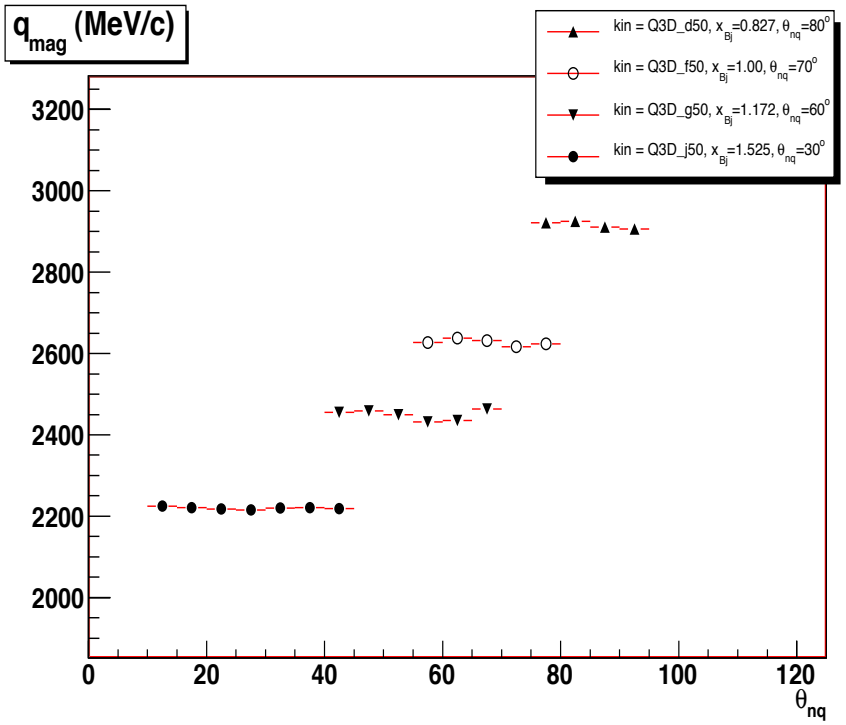

Figure 83: Simulated average 3-momentum transfer , $|\vec{q}|$, for each θ_{nq} bin for $p_{miss} = 500 MeV/c$ kinematics.

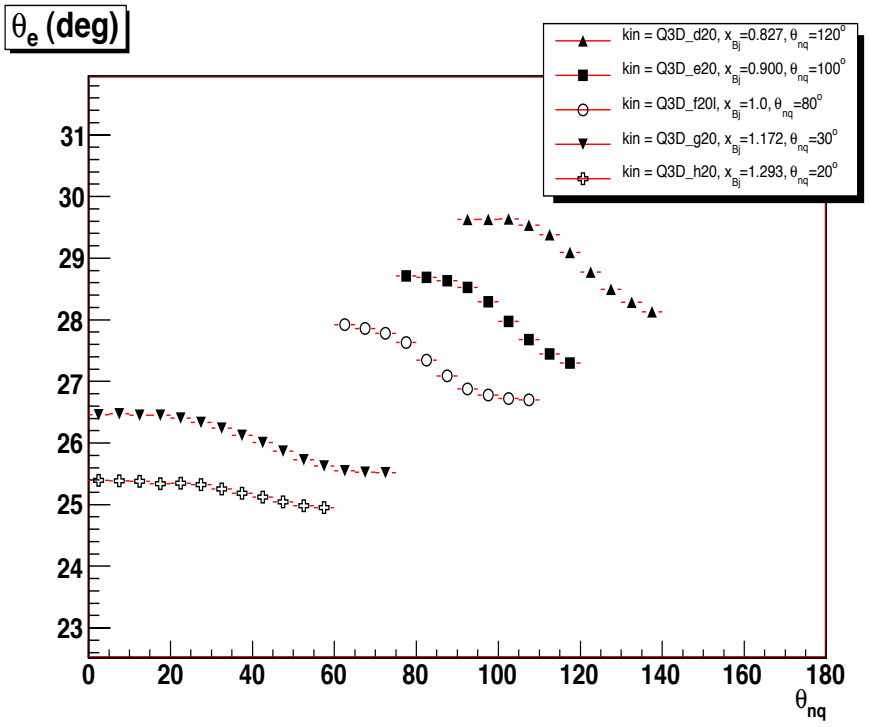

Figure 84: Simulated average electron scattering angle, for each θ_{nq} bin for $p_{miss} = 200 MeV/c$ kinematics.

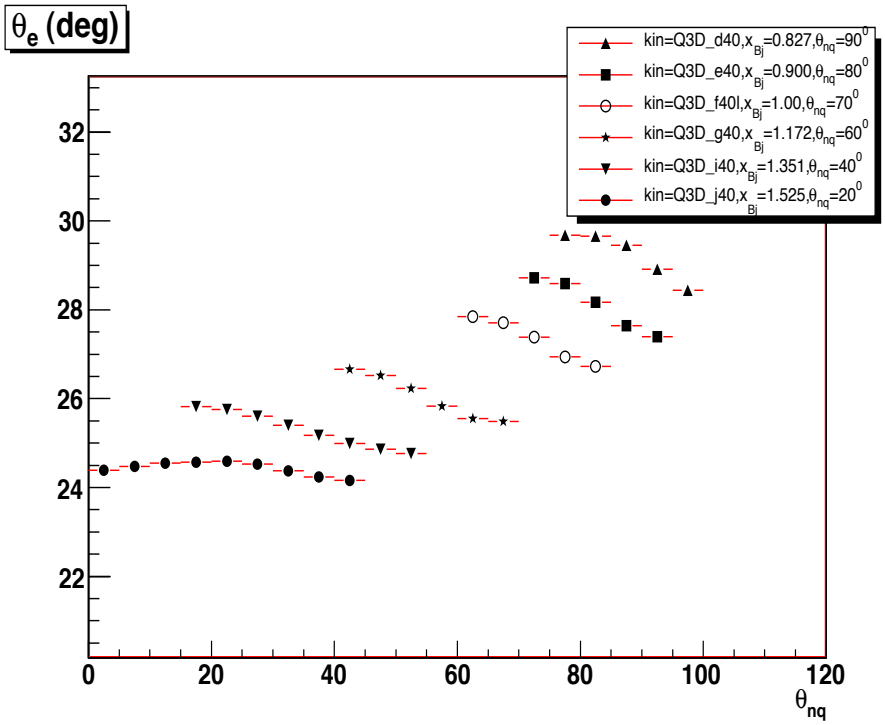

Figure 85: Simulated average electron scattering angle, for each θ_{nq} bin for $p_{miss} = 400 MeV/c$ kinematics.

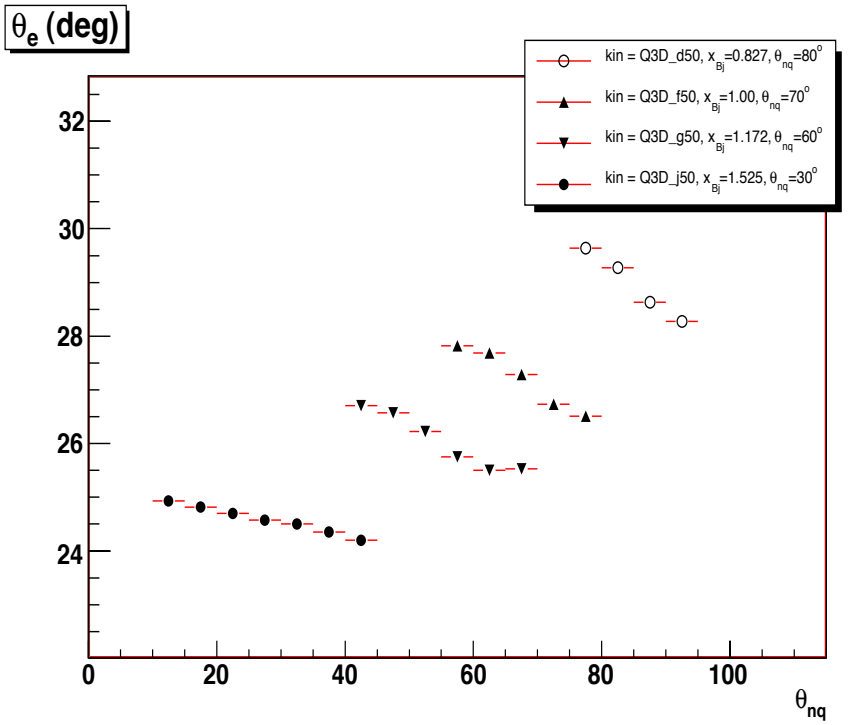

Figure 86: Simulated average electron scattering angle, for each θ_{nq} bin for $p_{miss} = 500 MeV/c$ kinematics.

C Fractional shift of the cross section

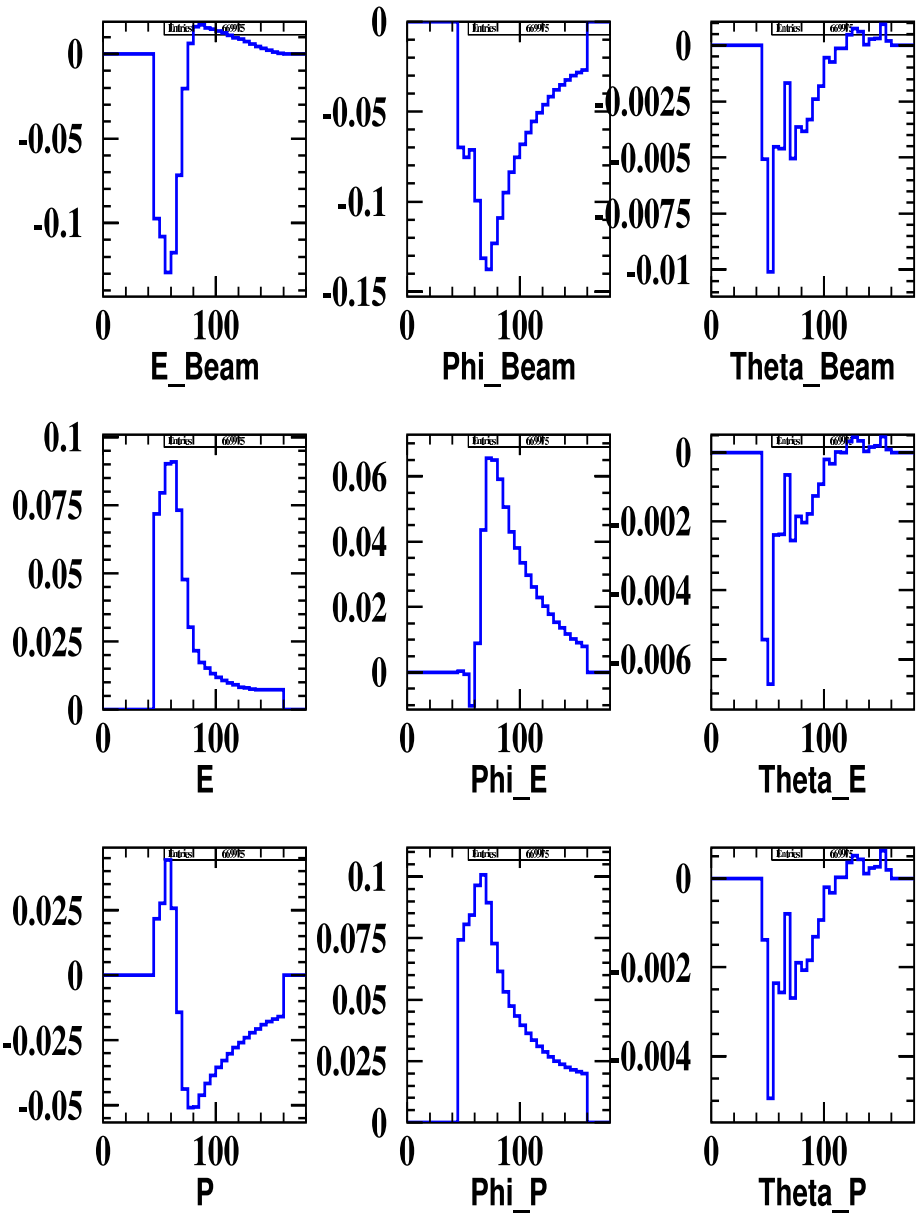

Figure 87: Fractional shifts in the cross section (y-axis) versus the θ_{nq} angle in degree (x-axis). The labels below each histogram refer to the quantity which was shifted in computing the change in cross section. The missing momentum is 200 MeV/c, $x_{Bj} = 1.0$, $\theta_{nq} = 80^o$.

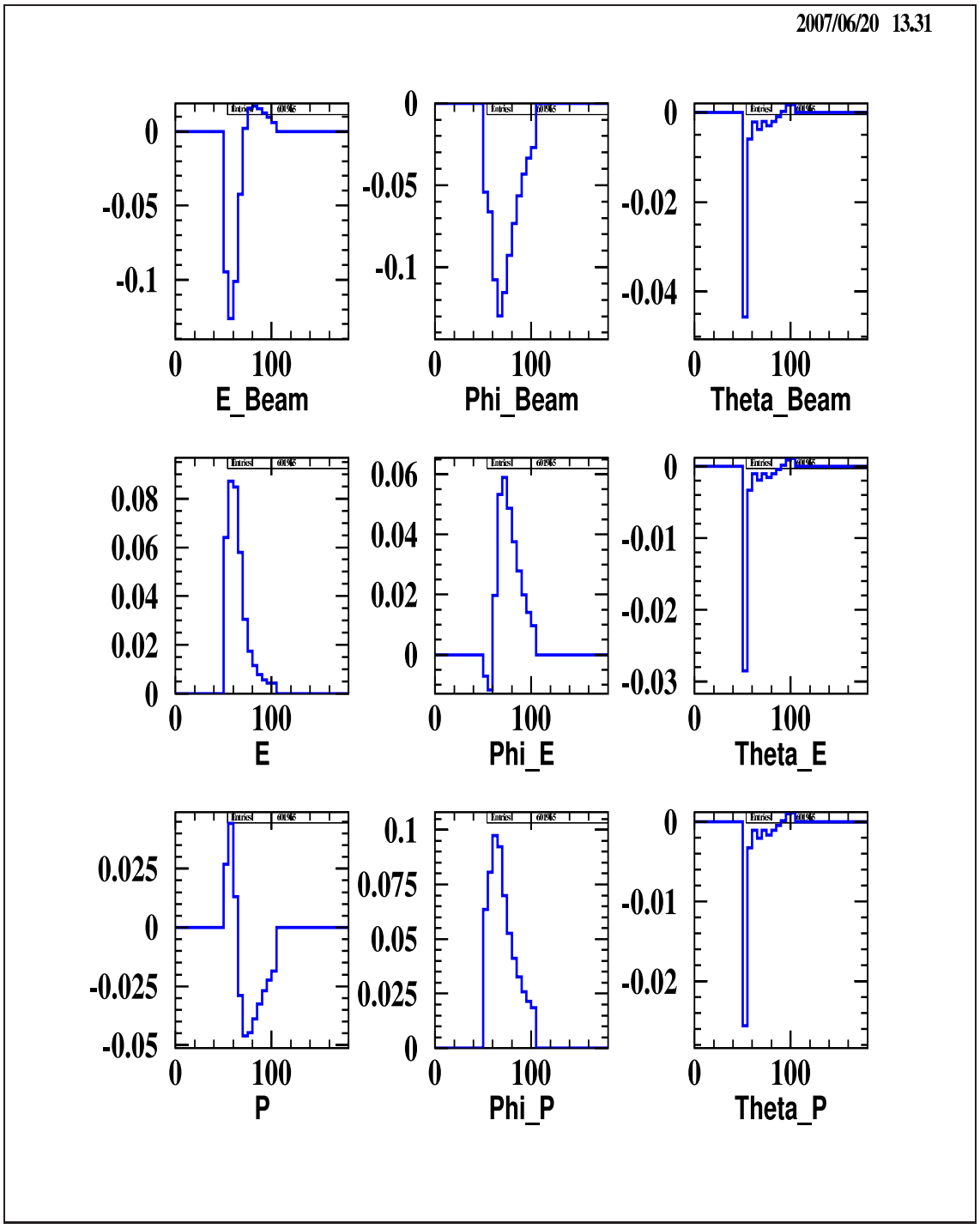

Figure 88: Fractional shifts in the cross section (y-axis) versus the θ_{nq} angle (x-axis). The labels below each histogram refer to the quantity which was shifted in computing the change in cross section. The missing momentum is 400 MeV/C, $x_{Bj} = 1.0$, $\theta_{nq} = 70^o$.

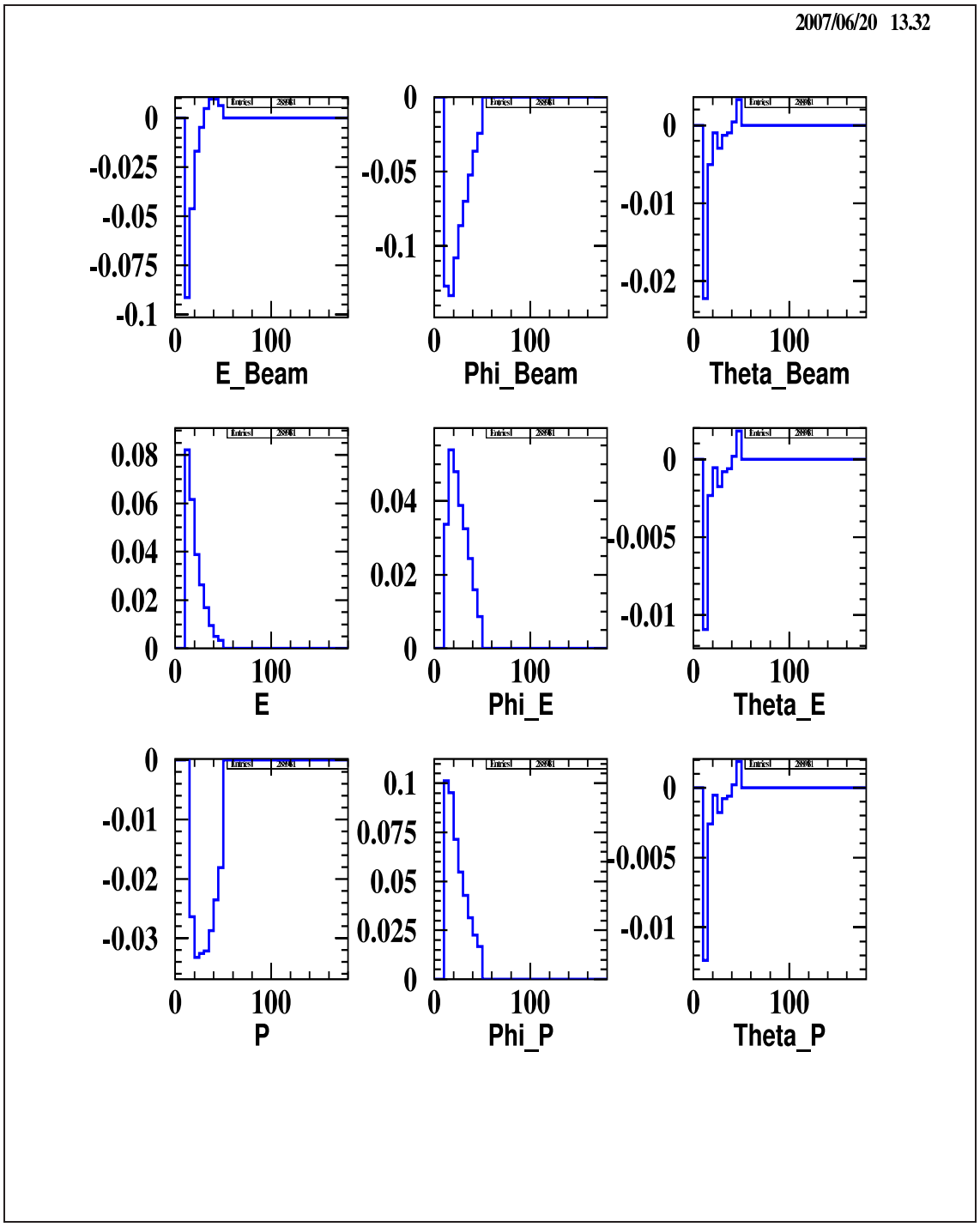

Figure 89: Fractional shifts in the cross section (y-axis) versus the θ_{nq} angle in (x-axis). The labels below each histogram refer to the quantity which was shifted in computing the change in cross section. The missing momentum is 500 MeV/c, x_{Bj}=1.525, θ_{nq}=30^o.

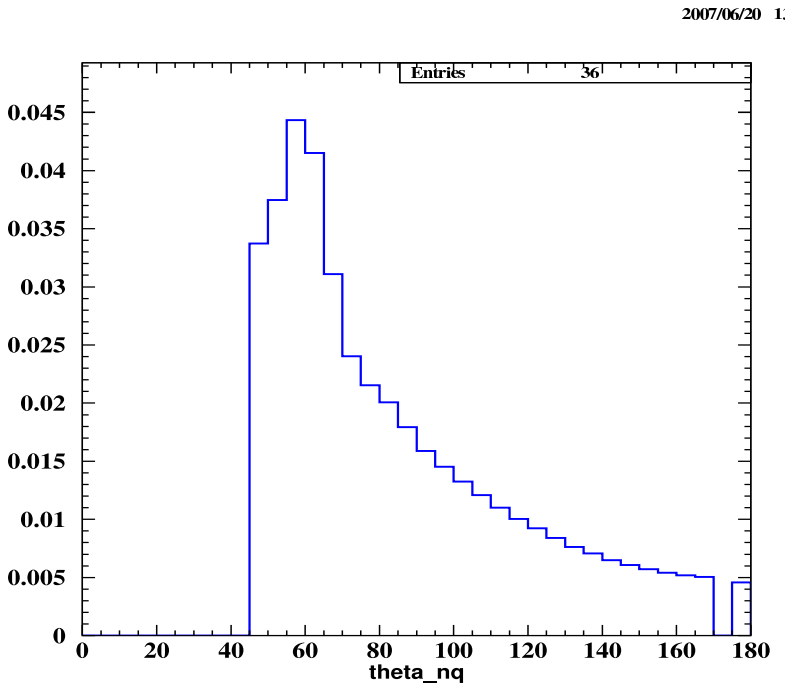

Figure 90: The total (quadrature sum) of the fractional shifts (kinematics dependent systematic uncertainties) as a function of θ_{nq} angle (^{o}). The fractional shift are calculated using the uncertainties given in Table 6. The missing momentum is 200 MeV/c, $x_{Bj} = 1.0$, $\theta_{nq} = 80^o$.

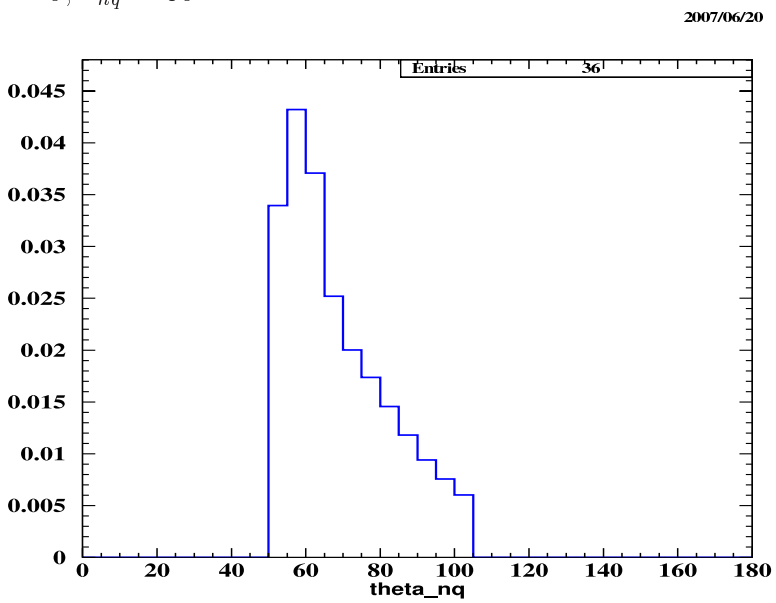

Figure 91: The total (quadrature sum) of the fractional shifts (kinematics dependent systematic uncertainties) as a function of θ_{nq} angle. The fractional shift are calculated using the uncertainties given in Table 6. The missing momentum is 400 MeV/c, $x_{Bj} = 1.0$, $\theta_{nq} = 70^o$.

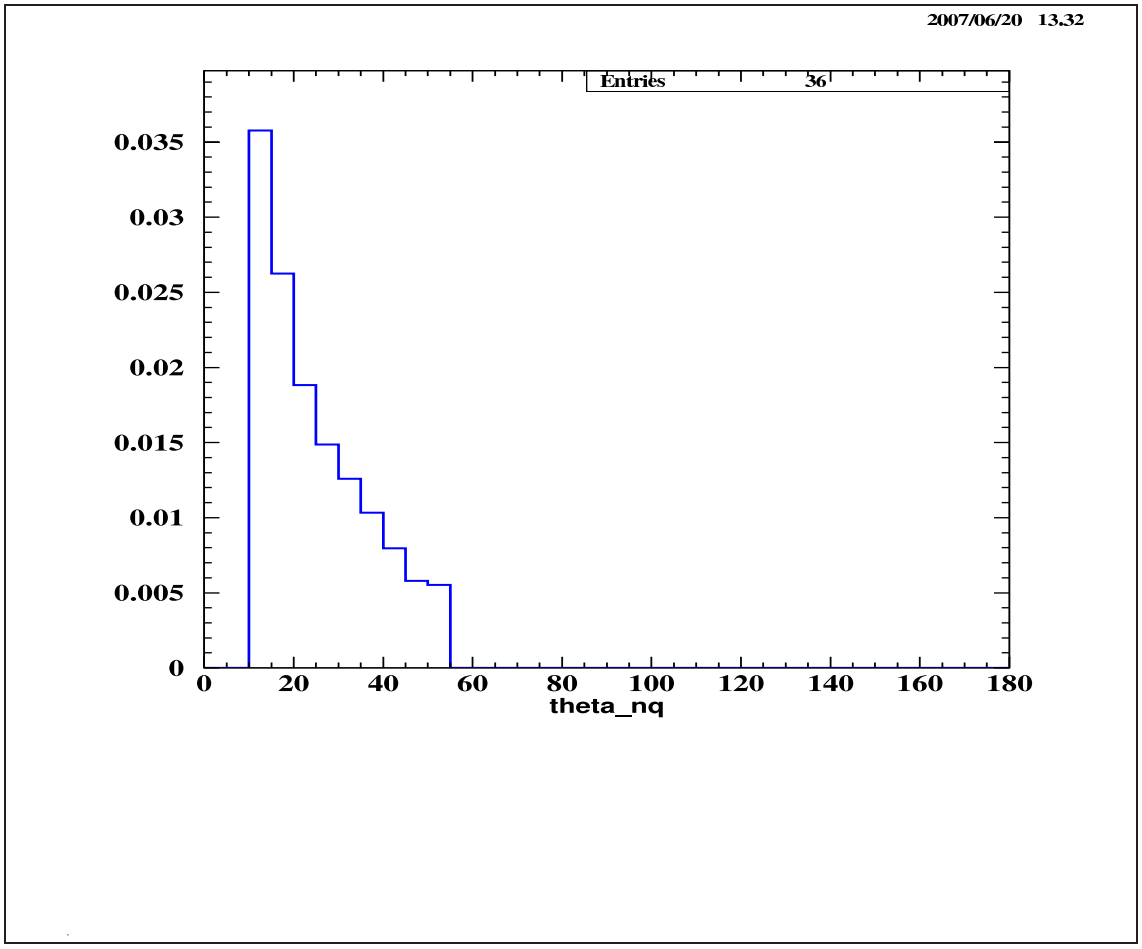

Figure 92: The total (quadrature sum) of the fractional shifts (kinematics dependent systematic uncertainties) as a function of θ_{nq} angle. The fractional shift are calculated using the uncertainties given in Table 6. The missing momentum is 500 MeV/c, x_{Bj}=1.525, θ_{nq}=30^o.

D Systematic uncertainties calculated for each θnq bin

Kin.	p_{miss}	θ_{nq}	Error $\delta\sigma(\%)$
Q3D_j40	400	12.5	2.048
Q3D_j40	400	17.5	1.559
Q3D_j40	400	22.5	1.257
Q3D_j40	400	27.5	1.043
Q3D_j40	400	32.5	0.853
Q3D_i40	400	27.5	2.165
Q3D_i40	400	32.5	1.806
Q3D_i40	400	37.5	1.588
Q3D_i40	400	42.5	1.423
Q3D_i40	400	47.5	1.278
Q3D_i40	400	52.5	1.112
Q3D_g40	400	47.5	2.135
Q3D_g40	400	52.5	1.902
Q3D_g40	400	57.5	1.698
Q3D_g40	400	62.5	1.51
Q3D_f40l	400	62.5	3.707
Q3D_f40l	400	67.5	2.521
Q3D_f40l	400	72.5	2.001
Q3D_f40l	400	77.5	1.738
Q3D_e40	400	77.5	2.711
Q3D_e40	400	82.5	2.661
Q3D_e40	400	87.5	2.601
Q3D_e40	400	92.5	2.742
Q3D_d40	400	82.5	2.417
Q3D_d40	400	87.5	2.763
Q3D_d40	400	92.5	2.933

Table 9: Systematic uncertainties for p_{miss}= 400 MeV/c.

Kin.	p_{miss}	θ_{nq}	Error $\delta\sigma(\%)$
Q3D_h20	200	2.5	2.118
Q3D_h20	200	7.5	2.383
Q3D_h20	200	12.5	2.802
Q3D_h20	200	17.5	3.019
Q3D_h20	200	22.5	2.373
Q3D_h20	200	27.5	1.76
Q3D_h20	200	32.5	1.361
Q3D_h20	200	37.5	1.158
Q3D_h20	200	42.5	1.034
Q3D_h20	200	47.5	0.946
Q3D_g20	200	22.5	2.209
Q3D_g20	200	27.5	2.004
Q3D_g20	200	32.5	1.831
Q3D_g20	200	37.5	1.708
Q3D_g20	200	42.5	1.61
Q3D_g20	200	47.5	1.532
Q3D_g20	200	52.5	1.467
Q3D_g20	200	57.5	1.402
Q3D_g20	200	62.5	1.338
Q3D_g20	200	67.5	1.27
Q3D_f20l	200	72.5	2.402
Q3D_f20l	200	77.5	2.154
Q3D_f20l	200	82.5	2.007
Q3D_f20l	200	87.5	1.794
Q3D_f20l	200	92.5	1.589
Q3D_f20l	200	97.5	1.452
Q3D_e20	200	87.5	2.424
Q3D_e20	200	92.5	2.473
Q3D_e20	200	97.5	2.658
Q3D_e20	200	102.5	2.754
Q3D_e20	200	107.5	3.13
Q3D_d20	200	102.5	1.659
Q3D_d20	200	107.5	1.606
Q3D_d20	200	112.5	1.759
Q3D_d20	200	117.5	2.025
Q3D_d20	200	122.5	2.341
Q3D_d20	200	127.5	2.727

Table 10: Systematic uncertainties for each θ_{nq} bin, for p_{miss}= 200 MeV/c.

Kin.	p_{miss}	θ_{nq}	Error $\delta\sigma(\%)$
Q3D_j50	500	22.5	4.483
Q3D_j50	500	27.5	1.983
Q3D_j50	500	32.5	1.596
Q3D_j50	500	37.5	2.336
Q3D_g50	500	47.5	2.351
Q3D_g50	500	52.5	2.01
Q3D_g50	500	57.5	1.731
Q3D_g50	500	62.5	1.47
Q3D_f50	500	62.5	2.59
Q3D_f50	500	67.5	2.334
Q3D_f50	500	72.5	2.129
Q3D_d50	500	77.5	2.37
Q3D_d50	500	82.5	2.68
Q3D_d50	500	87.5	2.741

Table 11: Systematic uncertainties for p_{miss}= 500 MeV/c.

E Cross section values for all kinematics and associated errors

Kin.	p_{miss}	θ_{nq}	σ $(fm^2/MeV/sr^2)$	Error $\delta\sigma$ $(fm^2/MeV/sr^2)$
Q3D_j40	400	12.5	5.25293e-12	1.51874e-12
Q3D_j40	400	17.5	4.29487e-12	9.86625e-13
Q3D_j40	400	22.5	7.02687e-12	1.19038e-12
Q3D_j40	400	27.5	6.72374e-12	1.37546e-12
Q3D_j40	400	32.5	4.96587e-12	1.65798e-12
Q3D_i40	400	27.5	2.82407e-12	9.4254e-13
Q3D_i40	400	32.5	5.04313e-12	8.79931e-13
Q3D_i40	400	37.5	4.58958e-12	6.85664e-13
Q3D_i40	400	42.5	6.02871e-12	7.49941e-13
Q3D_i40	400	47.5	6.61417e-12	9.11404e-13
Q3D_i40	400	52.5	5.79206e-12	1.45199e-12
Q3D_g40	400	47.5	4.66895e-12	8.26731e-13
Q3D_g40	400	52.5	5.41554e-12	7.00507e-13
Q3D_g40	400	57.5	7.02341e-12	7.97233e-13
Q3D_g40	400	62.5	1.14537e-11	1.32776e-12
Q3D_f40r	400	62.5	7.01501e-12	1.70423e-12
Q3D_f40r	400	67.5	9.29201e-12	9.92665e-13
Q3D_f40r	400	72.5	1.03077e-11	9.71955e-13
Q3D_f40r	400	77.5	1.30036e-11	1.51597e-12
Q3D_e40	400	77.5	8.77227e-12	9.31638e-13
Q3D_e40	400	82.5	9.3839e-12	8.44386e-13
Q3D_e40	400	87.5	1.01668e-11	1.31527e-12
Q3D_d40	400	82.5	7.27021e-12	1.48626e-12
Q3D_d40	400	87.5	7.14491e-12	7.26218e-13
Q3D_d40	400	92.5	7.48467e-12	8.17773e-13

Table 12: Cross section results for p_{miss}= 400MeV/c. Here are the tabulated experimental cross section values from Fig. 63.

Kin.	p_{miss}	θ_{nq}	σ $(fm^2/MeV/sr^2)$	Error $\delta\sigma$
Q3D_h20	200	2.5	4.35484e-10	4.70384e-11
Q3D_h20	200	7.5	1.56372e-10	1.63378e-11
Q3D_h20	200	12.5	1.47037e-10	1.30553e-11
Q3D_h20	200	17.5	1.41181e-10	1.20724e-11
Q3D_h20	200	22.5	1.75071e-10	1.35863e-11
Q3D_h20	200	27.5	1.69064e-10	1.42429e-11
Q3D_h20	200	32.5	1.68174e-10	1.58414e-11
Q3D_h20	200	37.5	1.63684e-10	1.76011e-11
Q3D_h20	200	42.5	1.66335e-10	2.09371e-11
Q3D_h20	200	47.5	1.27303e-10	2.38985e-11
Q3D_g20	200	22.5	1.54299e-10	2.27545e-11
Q3D_g20	200	27.5	1.27083e-10	1.68394e-11
Q3D_g20	200	32.5	1.67225e-10	1.62902e-11
Q3D_g20	200	37.5	1.59658e-10	1.4063e-11
Q3D_g20	200	42.5	1.2584e-10	1.14098e-11
Q3D_g20	200	47.5	1.40685e-10	1.15357e-11
Q3D_g20	200	52.5	1.32378e-10	1.14256e-11
Q3D_g20	200	57.5	1.45355e-10	1.32508e-11
Q3D_g20	200	62.5	1.41448e-10	1.62837e-11
Q3D_g20	200	67.5	8.42191e-11	1.84846e-11
Q3D_f20l	200	72.5	4.30534e-11	4.33738e-12
Q3D_f20l	200	77.5	5.3196e-11	3.73092e-12
Q3D_f20l	200	82.5	5.11882e-11	3.45748e-12
Q3D_f20l	200	87.5	6.74881e-11	4.26447e-12
Q3D_f20l	200	92.5	8.25163e-11	5.62398e-12
Q3D_f20l	200	97.5	1.00728e-10	8.74225e-12
Q3D_e20	200	87.5	9.14187e-11	8.61901e-12
Q3D_e20	200	92.5	1.05877e-10	7.39604e-12
Q3D_e20	200	97.5	1.06304e-10	7.10679e-12
Q3D_e20	200	102.5	1.28731e-10	8.83479e-12
Q3D_e20	200	107.5	1.45825e-10	1.23108e-11
Q3D_d20	200	102.5	8.41904e-11	8.98141e-12
Q3D_d20	200	107.5	9.09389e-11	6.78616e-12
Q3D_d20	200	112.5	9.59494e-11	6.3026e-12
Q3D_d20	200	117.5	9.14137e-11	6.69229e-12
Q3D_d20	200	122.5	8.45138e-11	8.17972e-12
Q3D_d20	200	127.5	1.0076e-10	1.33213e-11

Table 13: Cross section results for p_{miss}= 200MeV/c. Here are the tabulated experimental cross section values from Fig. 62.

Kin.	p_{miss}	θ_{nq}	σ $(fm^2/MeV/sr^2)$	Error $\delta\sigma$
Q3D_j50	500	22.5	1.50311e-12	5.31873e-13
Q3D_j50	500	27.5	1.47916e-12	3.70135e-13
Q3D_j50	500	32.5	1.94137e-12	4.05295e-13
Q3D_j50	500	37.5	3.53562e-12	7.08664e-13
Q3D_g50	500	47.5	2.66619e-12	8.89173e-13
Q3D_g50	500	52.5	3.06319e-12	6.53457e-13
Q3D_g50	500	57.5	5.06246e-12	8.69035e-13
Q3D_g50	500	62.5	5.39114e-12	1.55779e-12
Q3D_f50	500	62.5	4.98468e-12	8.31818e-13
Q3D_f50	500	67.5	6.62288e-12	6.73549e-13
Q3D_f50	500	72.5	8.04976e-12	9.92743e-13
Q3D_d50	500	77.5	4.07463e-12	8.69397e-13
Q3D_d50	500	82.5	4.81569e-12	5.42277e-13
Q3D_d50	500	87.5	5.47027e-12	9.0015e-13

Table 14: Cross section results for p_{miss}= 500 MeV/c. Here are the tabulated experimental cross section values from Fig. 64.

F Cross section ratio values ($\sigma EXP/\sigma_{PWIA}$) and associated errors

p_{miss}	θ_{nq}	$\sigma_{exp}/\sigma_{PWIA}$	Error
200	7.5	0.7869	0.08342
200	12.5	0.7269	0.06546
200	17.5	0.6843	0.05930
200	22.5	0.8590	0.05998
200	27.5	0.7806	0.05635
200	32.5	0.8379	0.05791
200	37.5	0.8029	0.05573
200	42.5	0.6811	0.05083
200	47.5	0.6679	0.05107
200	52.5	0.6412	0.05598
200	57.5	0.6915	0.06384
200	62.5	0.6622	0.07712
200	67.5	0.4091	0.09039
200	72.5	0.5445	0.05531
200	77.5	0.6315	0.04473
200	82.5	0.5564	0.03794
200	87.5	0.7026	0.03747
200	92.5	0.8171	0.04064
200	97.5	0.8635	0.04634
200	102.5	1.0147	0.05911
200	107.5	1.0455	0.05897
200	112.5	1.0397	0.06878
200	117.5	0.9092	0.06700
200	122.5	0.7652	0.07451
200	127.5	0.8217	0.10940

Table 15: The ratios between the experimental cross section and the PWIA cross ection for p_{miss}= 200 MeV/c. Here are the tabulated experimental cross section ratio values from Fig. 65.

p_{miss}	θ_{nq}	$\sigma_{exp}/\sigma_{PWIA}$	Error
400	12.5	0.5485	0.15889
400	17.5	0.4442	0.10220
400	22.5	0.7195	0.12221
400	27.5	0.5029	0.09180
400	32.5	0.5724	0.08931
400	37.5	0.5224	0.07825
400	42.5	0.6438	0.08037
400	47.5	0.6948	0.07585
400	52.5	0.7197	0.08373
400	57.5	0.9149	0.10416
400	62.5	1.3935	0.14642
400	67.5	1.8437	0.19747
400	72.5	1.8277	0.17283
400	77.5	2.1053	0.16585
400	82.5	2.0895	0.18847
400	87.5	1.5239	0.14735
400	92.5	1.3334	0.18315
400	97.5	1.3999	0.35023
500	22.5	0.3211	0.11375
500	27.5	0.3033	0.07597
500	32.5	0.3864	0.08080
500	37.5	0.6711	0.13488
500	47.5	0.8969	0.29931
500	52.5	0.9476	0.20230
500	57.5	1.3671	0.23495
500	62.5	1.7900	0.26559
500	67.5	2.5973	0.26467
500	72.5	2.7009	0.33385
500	77.5	2.6761	0.57155
500	82.5	2.8538	0.32169
500	87.5	2.7331	0.45025

Table 16: The ratios between the experimental cross section and the PWIA cross section. Here are the tabulated experimental cross section ratio values from Fig. 65, for p_{miss}= 400 MeV/c and p_{miss}= 500 MeV/c .

VITA

LUMINITA COMAN

2001-2007 Doctoral candidate in Physics, Florida International University.

1998-2000 M. Sc. (Physics), Florida International University.

1989-1994 B. Sc. (Physics Engineer), Bucharest University, Romania.

2001- Member of Thomas Jefferson National Accelerator Facility User Group: Builded, commissioned, performed calibration and tested a Neutron detector; Performed nuclear data analysis.

1996-1998 Speciality referee, National Commission for Nuclear Activities Control, Bucharest Romania; Elaborated, developed and implemented calibration methods for germanium detectors used for the determination of natural and artificial radioactivity levels; Calibration for radiation dosimeters, efficiency calibrations, reports, radioactivity levels in envirenment, radioactivity monitoring of Cernavoda Nuclear Power Plant.

PUBLICATIONS

1. High Resolution Spectroscopy of $^{\Lambda}_{12}$by Electroproduction, M. Iodice et al., Phys. Rev. Lett. 99, 052501 (2007).

2. Proton Spin Structure in the Resonance Region, F. R. Wesselmann et al., Phys. Rev. Lett. 98, 132003 (2007).

3. Proton G_E/G_M from beam-target asymmetry, M. K. Jones et al., Phys. Rev. C 74, 035201 (2006).

4. Measurement of the electric form factor of the neutron at $Q^2 = 0.5$ and 1.0 $(GeV/c)^2$, G. Warren et al. Phys. Rev. Lett. 92, 042301 (2004).

5. First Measurement of the Rotational Constants for the Homonuclear Molecular Ion He_2^+, L. Coman, M. Guna, L. Simons, and K. A. Hardy, Phys. Rev. Lett. 83, 2715 - 2717 (1999).

6. Dissociative Recombination of He^{2+}, L.Coman, M.Guna, L. Simons and K.A. Hardy, GEC99 Meeting of The American Physical Society, Bull. Am. Phys. Soc., 44 71 (1999).

7. Observation of the Natural Line Width of an Atomic Energy Level Using Dissociative Recombination Reaction Products, I. Boniche, L.Coman, M.Guna, J. Pai, L. Simons and K.A. Hardy, Abstract published in Bull. Am. Phys. Soc., V44, No. 6, 45 (1999).

CONTRIBUTED TALKS

1. (e,e'p) Studies of the Deuteron at High Q^2, Status Report: JLAB Experiment E01-020 Hall A, Thomas Jefferon Lab, Dec 2005 .

2. (e,e'p) Studies of the Deuteron at High Q^2, APS April Meeting Orlando, FL, April 16-19, 2005.

3. The rotational constants of He_2^+ and evidence of the indirect process for the dissociative recombination reaction, Kenneth Hardy, Luminita Coman, Libni Simons (Florida International University, Miami, Fl. 33199), APS April Meeting Orlando, FL, June 2000.